Development of Innovative Co-based Oxide Dispersion Strengthened (ODS) Superalloys

A Dissertation Submitted to Hokkaido University
for the Degree of Doctor of Philosophy

Hao YU

Division of Materials Science and Engineering

Graduate School of Engineering

Hokkaido University

2017

Table of contents

Abstract

In order to develop Co-based oxide dispersion strengthened (ODS) superalloys with excellent mechanical properties and oxidation resistance at the temperature above 1000 ºC, a novel Co-20Cr-(5,10)Al (wt. %) ODS superalloys containing 2.4 wt. % Hf and 1.5 wt. % Y_2O_3 were designed and fabricated by mechanical alloying (MA), spark plasma sintering (SPS), hot rolling and the final annealing at 1200 ºC.

Based on the results of microstructure characterization, the superalloys were found to contain a Co solid solution phase with face-centered cubic (fcc) structure and a CoAl phase with body-centered cubic (B2) structure, which offers the guarantee for good ductility and favorable strength, respectively. Composition and volume fraction of the both phases are almost consistent with the Co-Cr-Al ternary phase diagram computed with the Pandat software. Fine Y-Hf oxides particles are densely distributed inside the fcc solid solution and the B2 phase. Grain boundaries and phase boundaries are decorated with the oxide particles, which are beneficial to grains and phases stability at elevated temperature. Moreover, a unique core-shell structure of $Y_2Hf_7O_{17}$ in core and $Y_2Hf_2O_7$ at periphery was observed, which is responsible for the coarsening of the Y-Hf oxides.

High-temperature oxidation behavior of the Co-based ODS superalloys was investigated by the isothermal oxidation test at 900 ^oC and 1000 ^oC in air. With the increase of Al content from 5 wt. % to 10 wt. %, the oxidation resistance of the superalloys had been significantly improved by the formation of a single alumina scale, which is far better than conventional Co-based alloys. A faster θ- to α-alumina transformation at higher temperature was found to be responsible for the smaller weight gain at 1000 ºC than at 900 ºC for the 10 wt. % Al specimens. Besides, the effect of Cr and Y_2O_3 addition on the oxidation behavior of the Co-based superalloys was investigated, as well. The results indicate that the addition of Cr is beneficial to the oxidation resistance by accelerating the formation of an exclusive Al_2O_3 scale, i.e., changing the oxide scales morphologies from the multilevel scales with an external

$CoO/CoAl_2O_4$ and an internal Al_2O_3 to the single Al_2O_3 scale. With Y_2O_3 addition, the grain size of Al_2O_3 scale was decreased, and even though the weight gain of Co-20Cr-10Al ODS superalloys has been slightly accelerated, the Co-based ODS superalloys possess far better oxide-scale adherence than that in free Y_2O_3 alloys.

Tensile strengths of two Co-based ODS superalloys with 5wt. % and 10wt. % Al addition were measured at 23 ^oC, 250 ^oC, 500 ^oC, 700 ^oC and 1000 ^oC. 10Al shows less ultimate tensile strength (UTS) at low temperature since a brittle fracture caused by high B2 volume fraction. 5Al exhibits outstanding UTS of 2.85 GPa at room temperature, which is associated with the distribution of fine Y-Hf oxides and the nano-twins deformation during strain. Along with the increasing of temperature, a drastic reduction in tensile strength was observed, which is associated with grain boundary deformation due to the ultrafine grains of 500 nm in the 5Al and 800nm in the 10Al Co-based superalloys.

Therefore, since the occurrence of brittle fracture in 10Al with high B2 volume fraction, less Al should be considered to add into the composition of the Co-based superalloys. However, the 10Al superalloy possesses a better oxidation resistance than the 5Al to form a single alumina scale. Hence, the composition optimization based on altering the Al content should be focused, and 6 or 7 wt.% was considered to be applicable in this system.

Chapter 1 Introduction

Co-based ODS superalloys possess prominent oxidation resistance and stable strength, and they have broad application prospects for making the guide vanes of aviation jet engines and the stationary blades of industrial gas turbines [1, 2]. In order to make full use of this advantage and broaden application prospects, the advanced strengthening approaches for developing Co-based alloys are considered. The usual strengthening approach used in case of the conventional Co-based superalloys is based on W, Mo, Ta and Cr carbides precipitate strengthening [3]. However, the application of those conventional superalloys is limited up to 800 ºC, because the carbides easily coarsen above this temperature [4]. Lately γ'-Co_3(Al, W) precipitate strengthened Co-Al-W system has been developed and considered to be more effective with a high strength, but this γ'-phase is available only at a narrow temperature-composition range [5-8], i.e., the utilizing temperature is limited below 900 ^{o}C and the Cr addition which is beneficial to corrosion resistance has been proved to be deleterious effect on γ' stability [9]. In addition, the high temperature oxidation behavior of the γ' strengthened Co-based alloys still has to be improved further even though Klein et al. reported several additional elements like boron and silicon could significantly improve the oxidation resistance [9, 10]. Therefore, both of the two methods should be invalid due to a poor stability at elevated temperature up to 900 ^{o}C. Besides, such conventional carbides strengthened or the γ'-strengthened Co-based alloys are restricted in the alloying composition. As we know, alumina has been considered to be more protective scale than other conventional metal oxide scale due to its lower growth rate and nonvolatility at elevated temperature. However, the production of alumina-forming in the superalloys demands a high aluminum concentration, which has been clarified with a low operability in the Co-based alloys strengthened by the two approaches.

Fortunately, based on an extremely high thermal-stability of dispersed oxide particles at the temperature above 1000 ºC and a flexibly controllable composition of matrix, the oxide dispersion strengthening (ODS) is expected to be an advanced approach to increase service temperature of Co-based alloys alloys beyond 1000 ºC

[11]. In fact, the Ni-base and Fe-base ODS alloys have been developed, and already partially used as industrial materials [12-16]. Besides, in addition to their superior creep resistance and favorable high-temperature strength, ODS superalloys show better oxidation resistance than the ODS-free alloys with the same basic composition, which has been frequently proved with a large number of reports about oxidation behavior of Fe- and Ni based ODS superalloys [17-19]. However, the Co-based ODS system has received much less attention than Ni-based ODS and Fe-based ODS superalloys, and the study of high-temperature oxidation in Co-based ODS superalloys is scarcely conducted [20-22]. Zhang et al. proposed that Hf is effective to reduce the oxide particles size that could enhance strength significantly by forming $Y_2Hf_2O_7$ particles [23, 24]. Takezawa et al. had discovered Co-3Al-1.5Y_2O_3-1.2Hf ODS alloys, and they found that the oxide particles are extremely stable at the temperature above 1000 ºC, suggesting that the high temperature strength of this Co-based ODS superalloys can be enhanced dramatically as compared with the conventional Co based superalloys [25]. Soon afterwards, Sasaki et al. announced that Co ODS alloys were able to maintain high hardness with an outstanding microstructure stability after annealing at 1000 ºC for 240 h, owing the pinning of grain boundaries by the dispersed oxide particles [26].

In the present Phd work, aimed at developing novel Co-based superalloys with superior oxidation resistance and favorable strength at elevated temperature, the Co-20Cr-(5, 10)Al (wt. %) ODS superalloys have been synthesized by more Al-addition. 20 (wt. %) chromium was also introduced to promote the formation of alumina scale according to the reports on oxidation behavior of conventional Co-based alloys [20]. The Hf has been utilized to refine the oxide dispersoids, based on the reports by Zhang et al., suggesting that Hf is effective to reduce the oxide particles size by generating $Y_2Hf_2O_7$ particles [23, 24], which are excepted to provide a powerful guarantee for an improved strength at elevated temperature. In these systems, high-temperature strength is maintained by the dispersed oxide particles [13, 27] and high-temperature oxidation is prevented by the alumina scale at the temperature above 1000 ºC [20, 28]. The detailed microstructure and the phases

formed in Co-20Cr-(5, 10)Al (wt.%) ODS superalloys were investigated in terms of variable aluminum content. The effect of Al content on the high temperature oxidation properties of the novel Co-based ODS superalloys, as well as the influence of Cr and Y_2O_3 addition on the oxidation resistance were investigated through an isothermal oxidation test at 900 ºC and 1000 ºC under air condition. Besides, the tensile test was conducted to assess the novel Co-based superalloys and the related microstructure characterization was carried out to explain the mechanical properties. Based on these results, optimized composition was proposed from the points of high temperature strength and oxidation resistance.

Chapter 2 Theoretical background

2.1 Co-based superalloys and their strengthening

Cobalt-based alloys have been wildly used in the manufacturing of various components such as vanes or combustion containers in gas turbines, including the industrial type and aeroengines. Although cobalt-based alloys show less strength than nickel-based alloys at high temperature, it is still irreplaceable in the superalloys category and to be studied persistently since the advantages that [29]: (1) A higher melting temperature than nickel (1495 ^{o}C vs 1455 ^{o}C) which could further increase the process temperature of the gas turbine; (2) Cobalt-based superalloys have a better corrosion resistance. The diffusivity of sulphur in cobalt-based superalloys is approximately 100 times lower than in nickel based superalloys. In addition, the higher chromium content in cobalt-based alloys gives superior hot corrosion resistance in contaminated gas turbine atmospheres. (3) Cobalt-based superalloys possess a better thermal conductivity, resulting in a greater thermal shock resistance and better thermal fatigue resistance than nickel-based superalloys.

2.1.1 Carbide precipitate strengthened

In the 1940s, the cobalt-based alloys were come into service for the manufacturing of high temperature component, i.e., the HS-21 (derived from cobalt-chromium-molybdenum) was initially used for making turbochargers and gas turbine. Thereafter, the wrought Co-Ni-Cr alloy S-816 was developed and used for the producing of gas turbine blades and vanes. And in 1943, the modified Co-Ni-Cr-W alloy X-40 come out and still be used in gas turbine vanes. Their design is aimed primarily at improving elevated temperature strength by use of solid solution and carbide precipitation strengthening mechanisms. Such mechanisms must tolerate substantial additions of chromium (above 20 wt. %) in order to obtain a satisfactory oxidation resistance and a good hot corrosion resistance. Solid solution strengthening results principally from the additions of chromium, tantalum, niobium and tungsten [30]. Carbide precipitate strengthened Co-based superalloys are achieved by the precipitation of cubic and non-coherent carbide partlcles, which are mainly composed

of chromium-carbide [29]. In order to ensure the formation of enough carbides precipitants, a high chromium contents in the range of 18 to 35 wt. % and carbon contents from 0.25 to 1.0 wt.% are introduced into composition, in which the carbon contents is much higher than that in the austenitic stainless steel (0.02 to 0.20 wt.%) and Ni-based superalloys (0.05 to 0.20 wt.%). Most of the carbides precipitate during the process of solidification, and decorate at grain boundaries and phase boundaries, which inhibit grain boundary sliding and benefit to the grain and phase stability at elevated temperature. The strength of cobalt-based superalloys is inversely related to the carbide particle size and directly related to the volume fraction of carbides [30]. Besides, the carbides are metastable and could be broken down to the secondary carbides with fine grain size during aging or mechanical working, which is beneficial to the improvement of mechanical properties through pinning dislocation and hardening matrix [31].

According to the content of Cr, the carbides in Co-based superalloys could be classified into M_3C_2, M_7C_3 and $M_{23}C_6$. Basically the chromium enriched carbides contain Co, tungsten (W), or molybdenum (Mo), which would in place of the Cr position in the carbides. M_3C_2 and M_7C_3 are easily to form in the Co-based alloys with a low Cr/C ratio, which shows a rhombic crystal structure and a trigonal crystal structure, respectively. M_7C_3 is metastable and can be dissolved during solution treating and transforms to $M_{23}C_6$ during aging heat treatment with following decomposition reaction [32]:

$$23Cr_7C_3 \rightarrow 7Cr_{23}C_6 + 27C \quad (2.1)$$

Meanwhile, a re-precipitation reaction would occur if the Cr content is high enough, as shown below, resulting from the combination of the dissociative carbon atoms and other chromium atom in the alloy matrix.

$$6C + 23Cr \rightarrow Cr_{23}C_6 \quad (2.2)$$

$M_{23}C_6$ is the main secondary strengthened phase in the superalloys which contains a high Cr/C ratio. Basically, the $M_{23}C_6$ shows a relatively fine grain size with a unique shape of an interdendritic precipitate within the secondary dendrite arms, even though the detailed morphology is determined by the chemical composition and the process

of cooling rate [33, 34].

In addition, MC and M_6C are another kind of carbides that enrich refractory elements, such as zirconium (Zr) tantalum (Ta), hafnium (Hf), niobium (Nb), etc. MC carbides are typically the form of TaC, HfC, NbC, etc., which possess high stability and form in the process of solidification. In most of commercial Co-based alloys, the MC carbides are observed to be dispersed inside both matrix and along grain boundaries and grain boundary triple junctions. Besides, MC carbides are also metastable and could react with matrix during service, resulting in the generation of M_6C via the equation below [29],

$$\mathrm{MC} + \text{austenite} \rightarrow \mathrm{M_6C} \tag{2.3}$$

Such as

$$\mathrm{TaC} + (\mathrm{Co, Ni, Cr, C}) \rightarrow (\mathrm{Co, Ni})_4(\mathrm{Cr, Ta})_2\mathrm{C} \tag{2.4}$$

Optimum mechanical properties are obtained through a balance between the carbides at the grain boundaries and those in the matrix. Grain boundary carbides, regardless of type, should be present as discrete particles. Continuous carbide networks at grain boundaries reduce impact ductility and creep rupture properties.

Table 2.1 listed several typical carbide precipitates strengthened Co-based conventional alloys, in which the detailed chemical compositions were given. Besides, **Fig. 2.1** shows the figure of ultimate tensile strength (UTS) vs. temperature for those conventional Co-based alloys.

Table 2.1 Several typical carbide strengthened Co-based alloys and corresponding elemental compositions

Alloys	Compositions (wt %)								
	Co	C	Cr	Ni	W	Ta	Fe	Nb	Other
Haynes 188	Bal.	0.1	22	22	14		＜3		0.07La, Si, Mn
MAR-M302	Bal.	0.85	21.5	＜1.5	10	9	＜1.5		0.05B, 0.2Zr
MAR-M509	Bal.	0.6	22.5		7	3.5			0.2Ti, 0.5Zr
WI-52	Bal.	0.45	21	＜1	11		2	2	0.3Mn, 0.3Si
X-40	Bal.	0.5	25.5	10	7.5		＜2		0.7Mn, 0.8Si

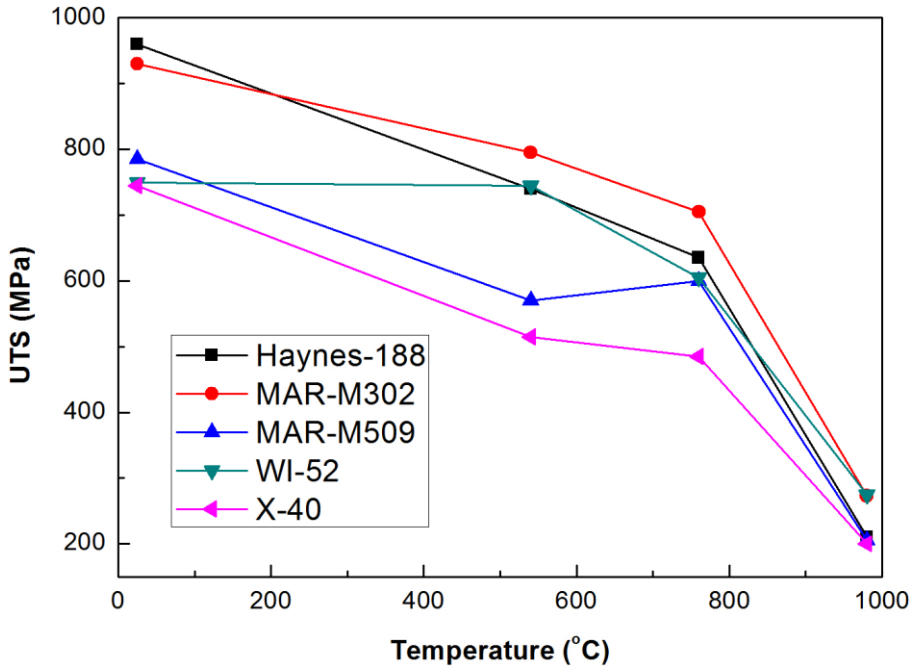

Fig. 2.1 UTS vs. temperature in carbide strengthened Co-based alloys.

2.1.2 γ'-Co_3(Al, W) precipitate strengthened

Since the development of advanced vacuum melting techniques in the 1950s, a high content of reactive elements such as Al and Ti could be added into alloy without oxidation in high vacuum atmosphere, resulting in the exploitation of γ′ strengthened (Ni_3Al compound with $L1_2$ structure) Ni-based superalloys [35], which possess stronger mechanical properties than Co-based alloy. In the 1950-1970, the γ'-Ni_3Al strengthened Ni-based superalloys were widely studied and rapidly developed to be the main force in high temperature materials. Therefore, in order to overcoming the shortage of conventional carbide strengthening, a comparable precipitation hardening mechanism with the γ'-Ni_3Al strengthened Ni-based superalloys was trying for the discovering of Co-based alloy. In the 1970s, the Co-based superalloys decorated with a γ′ (Co_3Ti) phase was developed, but the application of this alloy was limited since an inferior stability of the γ′ at the temperature above 750 °C [36]. In 2006, Sato. et al.

launched a new γ′ strengthened Co-Al-W superalloys [5], which possess a high strength comparable to Ni-based superalloys at elevated temperature. The high strength is attributed to a Co_3 (Al, W) compound with $L1_2$ structure, similar to the Ni_3Al in the Ni-based superalloys, which could keep stability at the temperature up to 900 ^oC. Besides, this novel γ'-Co_3(Al, W) phase can coexist with the cobalt fcc solid solution matrix with a favorable lattice mismatch of up to 0.53 %, allowing the precipitate-matrix interface to be coherent. Therefore, profiting from a similar $L1_2$ structure of the Ni_3Al phase in the Ni-based superalloys, the new Co_3 (Al, W) compound in Co-based superalloys is another possible strengthening approach to broaden the application of Co-based alloys at high temperature. However, as mentioned above, their strength is lost at temperature beyond 1000 °C due to the γ'-Co_3(Al, W) phase dissolution, i.e. the service temperature is restricted to 900 °C [8, 9].

2.1.3 Oxide dispersion strengthening (ODS)

ODS has been wildly utilized for the development of high temperature superalloys, in which the dispersion strengthening results from the fine oxide particles which are densely distributed in matrix. In general, the oxide particles possess several typical characteristics, such as an extremely high thermostability, inert and won't react with matrix, low diffusion rate and low interface energy, a high coherence with matrix, etc [37]. Basically, Y_2O_3 has been adopted as the main oxide particles for the manufacture of ODS superalloys in the world, since it almost meets all the requirements and without radioactivity [38]. The amount of the particles shows a close relationship with the mechanical properties, i.e., a high volume fraction of the particles could enhance the strength but decrease the plasticity. Thus, the content of the secondary dispersoid is usually controlled in the range of 0.5-2.0(wt. %). Besides, at a given concentration of the partices, the dispersoid size and the average distance between two particles are other two important factors, which should less than 0.05 μm and 0.1 μm, respectively. Basically, ODS superalloys show following characteristics:

(1) A high service temperature. In comparison with conventional superalloys, whose strength is maintained to the temperature of 0.7 T_m (T_m: Melting point), the ODS superalloys can reach to the 0.857 T_m and result in the improving of service temperature by 100-200 ^oC; (2) A high yield strength, which is close to tensile strength; (3) Superior creep properties at elevated temperature. The microstructure shows high stability even after a long-term service at high temperature, which is attributed to the pinning effect of the secondary dispersoids [39].

Dislocation theory has been deemed to as the representative view to interpret the dispersion strengthening mechanism. In the ODS superalloys, the dispersed secondary particles play as the strong barriers for the movement of dislocation during deformation. In order to overcome the obstacles and move forward, the dislocation lines need be loaded with a higher stress, resulting in a higher strength in the ODS superalloys. Orowan mechanism is one of the most famous theories to describe the process that the dislocations interact with or bypass the obstacles. The **Fig. 2.2** schematically illustrates the Orowan mechanism, as shown below [40].

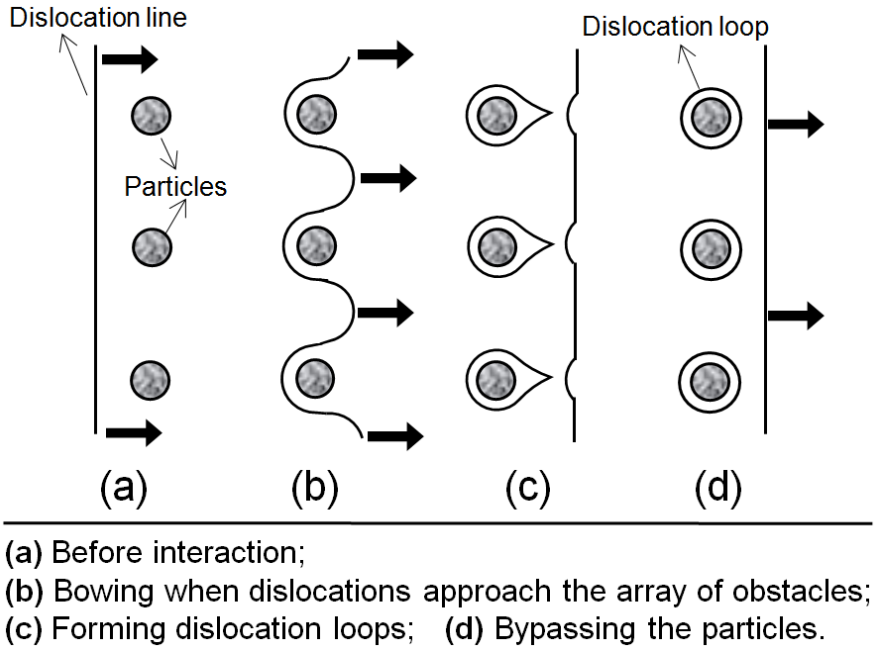

Fig. 2.2 Schematic of Orowan mechanism

In accordance with the above mechanism, when dislocation lines approach an array of secondary dispersoid, it cannot bypass directly and will bow around the particles until it leaves a dislocation loop on the surface of the obstacle. The bowing of dislocation lines could increase the local lattice distortion energy and result in a higher resistance for the dislocation motion and sliding [37].

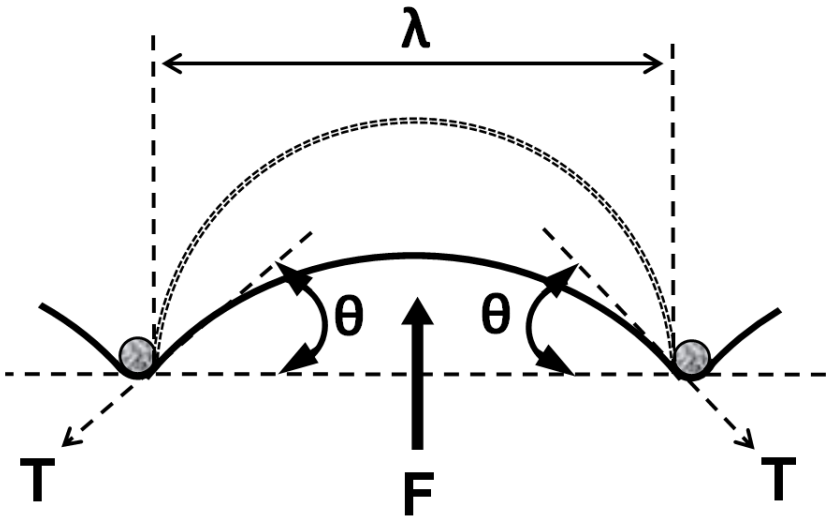

Fig. 2.3 Equilibrium model between the dislocation and particles

Under the action of shear stress (τ), the dislocation lines bow and form a circular arc once approach the obstacles, the radius of this arc depends on the loaded stress (F) and line tension (T) of dislocation. The bending angle (θ) of the dislocation lines during the interaction with the obstacles could be expressed with following equation since the balance between the F and T (**Fig. 2.3**),

$$F = 2T \sin \theta \tag{2.5}$$

As the barriers for dislocation movement, the obstacles is obviously stronger than single solute atoms, thus the θ_c (critical angle) could be suppose to be a larger value. When the $\theta = \pi/2$, the dislocation line would keep semicircle and the F reaches to maximum F_{max},

$$F_{max} = 2T = \tau_c b\lambda, \quad (2.6)$$

in which, the τ_c is critical shear stress; the λ is the distance between two particles on dislocation line; the b is Burgers vector.

If substituting the T with its approximate value, $\frac{1}{2}Gb^2$ (G is shear modulus), the Eq. (2.6) could be rewritten as follows,

$$\tau_c b\lambda = Gb^2, \text{ So } \tau_c = \frac{Gb}{\lambda} \quad (2.7)$$

The Eq. (2.7) proves that the yield stress is inversely proportional to the distance of two adjacent particles, Therefore, the improvement of yield strength in ODS superalloys could be achieved via shortening the interparticle distance [41, 42].

Until now, oxide dispersion strengthened Fe- and Ni-based superalloys have already been partially used as industrial materials. The **Table 2.2** and **Table 2.3** have listed typical Fe- and Ni-ODS superalloys, respectively [43].

Table 2.2 Several typical Fe-based ODS superalloys

Wt. %

Alloys	Cr	Al	Ti	Mo	Y_2O_3
MA956	20	4.5	0.5	-	0.5
MA957	14	-	1.0	0.3	0.25
PM2000	20	5.5	0.5	-	0.5
DT2906	13	-	2.5	1.5	0.75
DT2203Y05	13	-	2.2	1.5	0.5
ODM331	13	3	0.6	1.5	0.5
ODM751	16.5	4.5	0.6	1.5	0.5

Table 2.3 Several typical Ni-based ODS superalloys

Wt. %

Alloys	Cr	Al	Co	Ti	Mo	W	Ta	Y_2O_3
MA754	20	0.3	-	0.5	-	-	-	0.6
MA758	30	0.3	-	0.5	-	-	-	0.6
MA760	20	6.0	-	-	2.0	3.5	-	0.9
MA6000	15	4.5	-	2.5	2.0	4.0	2.0	1.1
PM3000	20	6.0	-	-	-	3.5	-	0.9/1.1
PM3000S	17	6.6	-	-	2.0	3.5	2.0	0.9/1.1
PM1000	20	0.3	-	-	0.5	-	-	0.6
TM02	5.9	4.2	9.7	-	-	12.4	4.7	1.1
Alloy98	6.8	5.2	5.1	-	-	8.6	5.7	1.1

However, almost no ODS Co-based superalloys could be referred for the application in industry field. As mentioned in above section, there are only a few researches had been conducted for the Co-based ODS superalloys. The development of the oxide dispersion strengthened Co-based superalloys starts to be focused since Zhang et al. proved that the Y-Hf oxides works effectively for the strengthening of Co-based alloys [23].

2.2 High temperature oxidation in air

In the design of Co-based superalloys, the high temperature oxidation resistance must be another key point to be considered, since the alloys would suffer from a metal loss with the formation of oxide scale in surrounding air, and the high temperature environment could further accelerate the process of this oxidation. Almost all the metals would be oxidized due to the reaction with oxygen. The oxidation process is unavoidable and continuously happens in oxidizing environments. If the alloys show a high oxidation rate during the oxidation process, the components of this alloy would be invalid since an erosion of the metal. In order to improve the oxidation resistance at elevated high temperature, for most of conventional Co-based alloys, overlay coating has been wildly applied to deposit a protective layer at the alloy surface, such as the thermal barrier coating (TBC). However, it's also significant to modify the substrate metals, which can provide a superior oxidation resistance automatically, i.e., the substrate could form a thin and protective oxide scale on the surfaces during the oxidation reaction, which possesses a low growth rate and suppress the further oxidation.

Initially, an oxide scale could be established rapidly on the surface of the bare substrates, especially in an elevated temperature, which could promote the process with higher reaction kinetics. Thereafter, if the oxide layer is compact and protective, the oxidation rate could be decreased gradually with the increasing of the scale thickness. The detailed rate of this oxidation reaction depends on the properties of the oxide scales, such as chemical composition, structure, growth rate, compactness, adherence, etc, which directly affect the transport processes of the cation and anion within the scale and the capability as a physical barrier between the interface of the outer air and inner metal. In general, thermodynamic and kinetic are two different starting points to interpret the high temperature oxidation behavior of alloys.

2.2.1 Thermodynamic aspect

Once the bare alloys expose in gaseous oxygen environment, oxidation process would happen between the metal and oxygen with the typical reaction listed below,

$$M + O_2 = MO_2 \quad (2.8)$$

in which M represents the reacting metal, such as Fe, Ni or Co; MO_2 is corresponding oxide, and its detailed chemical formula depends on the chemical valence of M.

The driving force for this reaction is Gibbs energy change (ΔG), i.e., the oxidation process can occur spontaneously only with a negative value of ΔG, and more mass gain would happen with the increasing of the oxides. If the ΔG equals to zero, the oxidation reaches to a thermodynamic equilibrium and oxidation mass gains stops [44].

Based on the Van't Hoff isothermal equation, the Gibbs energy change at a constant temperature (T) could be expressed with following equation:

$$\Delta G = \Delta G_0 + RT \cdot \ln K \quad (2.9)$$

$$K = \frac{\alpha'_{MO_2}}{\alpha'_M p'_{O_2}} \quad (2.10)$$

ΔG_0 is standard Gibbs free energy change at the temperature of T; R is gas constant; K is Equilibrium constant; α'_M and α'_{MO_2} is the activity of metal M and its oxides MO_2, respectively, both equal to 1; p'_{O_2} is the oxygen partial pressure in surrounding air.

If the ΔG equals to zero and the reaction reaches to a thermodynamic equilibrium, the equation (2.9) could be written as follows:

$$\Delta G_0 = -RT \cdot \ln K = -RT \ln \frac{\alpha_{MO_2}}{\alpha_M p_{O_2}} \quad (2.11)$$

where T is the temperature of the thermodynamic equilibrium; α_M and α_{MO_2} are the activity of the metal M and oxides MO_2 at this T, both equal to 1, as well; p_{O_2} represents the oxygen partial pressure in the thermodynamic equilibrium, also equals to the dissociation pressure of the MO_2 oxide.

Substituting Eq. (2.11) into Eq. (2.9), we obtain Eq. (2.12) as follows,

$$\Delta G = -RT \ln \frac{1}{p_{O_2}} + RT \ln \frac{1}{p'_{O_2}} \quad (2.12)$$

Therefore, on a constant temperature T, based on the Eq. (2.12), it's able to directly judge that the alloys would be oxidized or not via comparing the dissociation pressure

of the MO_2 oxide (p_{O_2}) and the oxygen partial pressure (p'_{O_2}). If $p'_{O_2} > p_{O_2}$, the ΔG will less than zero and results in the formation of more oxide MO_2; If the $p'_{O_2} = p_{O_2}$, the ΔG will equal to zero and oxidation reaction reach to the thermodynamic equilibrium; If the $p'_{O_2} < p_{O_2}$, the ΔG will be greater than zero and the reaction occurs toward the dissociation direction of the oxide MO_2.

In general, the oxygen partial pressure could be deemed to a constant in a normal atmospheric condition, i.e., $p'_{O_2} = 21.28$ KPa. Thus, the stability of a metal in the normal air could be known through comparing the value of the dissociation pressure of oxide. **Table 2.4** shows a list of the dissociation pressures of some typical oxides at 1000 ^oC.

Table 2.4 The dissociation pressures of some typical oxides at 1000 ^oC.

Equations	Dissociation pressure/KPa	Equations	Dissociation pressure/KPa
Al_2O_3=2 Al+3/2 O_2	1.3×10^{-33}	CoO=Co+1/2 O_2	1.6×10^{-10}
Cr_2O_3=2 Cr+3/2 O_2	2.3×10^{-20}	Co_3O_4=3 CoO+1/2 O_2	2.7×10^{2}
FeO=Fe+1/2 O_2	1.7×10^{-13}	MnO=Mn+1/2 O_2	1.1×10^{-22}
Fe_3O_4=3 FeO+1/2 O_2	2.8×10^{-11}	Mn_3O_4=3 MnO+1/2 O_2	2.2×10^{-4}
Fe_2O_3=2/3 FeO+1/6 O_2	1.7×10^{-4}	Mn_2O_3=2/3 Mn_3O_4+1/2 O_2	1.3×10^{2}
NiO=Ni+1/2 O_2	1.7×10^{-8}	SiO_2=Si+O_2	1.1×10^{-26}

In 1944, with the advent of the famous Ellingham/Richardson diagrams [45], as shown in **Fig. 2.4**, in which the standard free energies for the formation of several typical oxides have been listed along with the changing of temperatures, the corresponding dissociation pressures of the oxides and the standard Gibbs free energy of the oxide formation could be obtained conveniently. It could be understand directly that which phases form and in what sequence, the metal which is more close to the bottom of this diagram would possess a higher affinity for oxygen, i.e., the oxidized

products should be more stable.

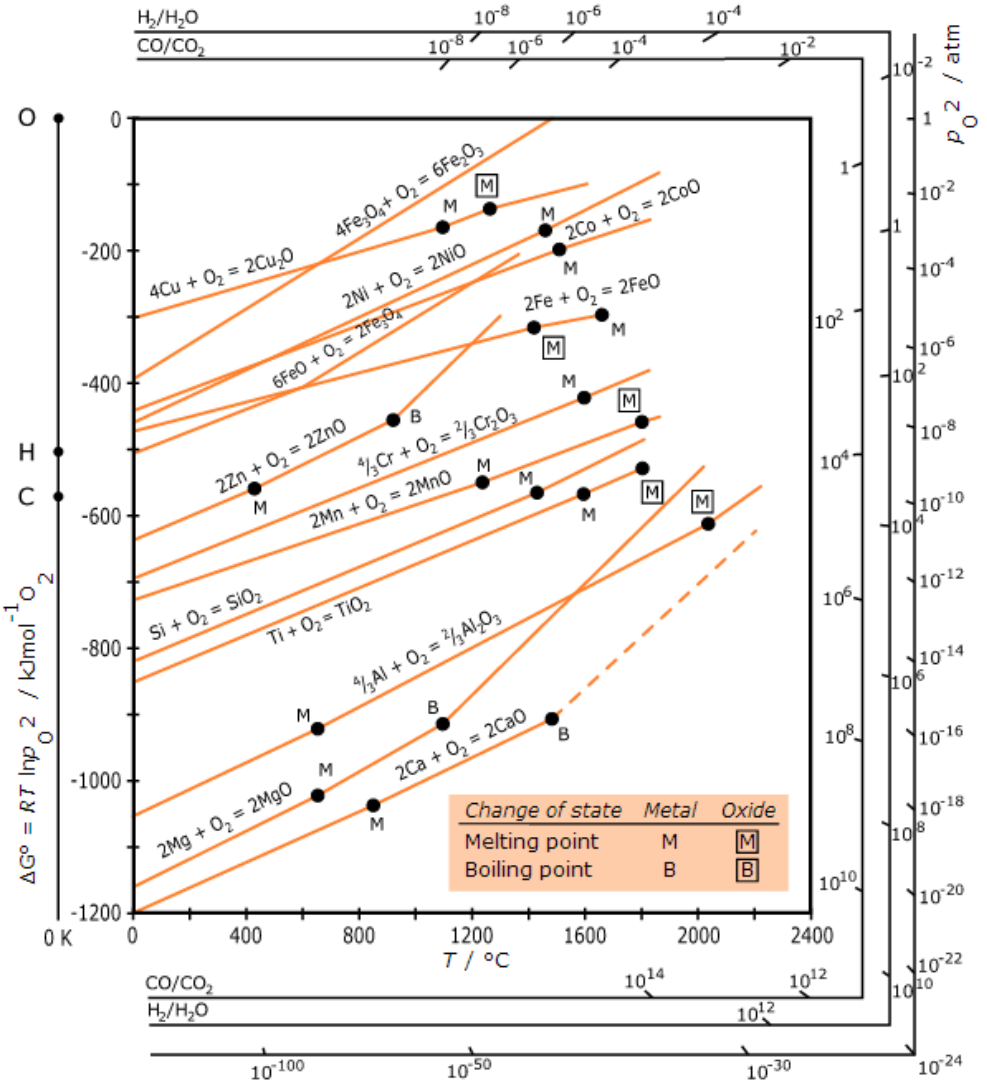

Fig. 2.4 Ellingham/Richardson diagram for several typical oxides

However, there are several limitations on the application of the Ellingham/Richardson diagram, i.e., (1) the diagram only can be used in an equilibrium system, is invalid for non-equilibrium system; (2) Basically, the diagram is for the reactions without any solution participates; (3) the diagram is capable for judging the possibility of oxidation reaction and forecasting its tendency, cannot indicate the oxidation rate quantitatively which belongs to the field of kinetics [46].

2.2.2 Kinetics aspect

The oxidation kinetics of metals on high temperature is another important knowledge for explaining the oxidation mechanisms since the Ellingham-Richardson diagram is unable to take into account for the kinetics of the oxidation process. The oxidation kinetics is focusing on the growth of oxide scales and its growth regulation, in other word, the rates of the scales formation. Generally, the rates of the oxidation are determined by chemical compositions, temperature, reaction time, surrounding air, surface preparation, etc. Due to the fact that the oxidized products are usually located on the surface of metals, the oxidation rate could be expressed with the mass gain on unit area, ΔW (mg/cm^2). The thickness of scale with the function of mass gain has been shown below,

$$y = \frac{\Delta W M_{OX}}{M_{O_2} D} \tag{2.13}$$

where y is the thickness of scale; ΔW is the mass gain on unit area; M_{OX} and M_{O_2} is the molar mass of the oxides and oxygen, respectively; D is the density of oxides.

The regulations of oxidation kinetics depend on a lot of factors, such as the kinds of metals, oxidation temperature and exposure time. It could obeys different oxidation kinetics even the same metals but oxidized at different temperature; whereas at a constant temperature, the oxidation kinetics would alter to be another one with the elongation of exposure time. In the case of the design for high temperature alloys, the oxidation kinetics has been paid high attention since that it's able to estimate the service life of the alloys components at a given temperature and atmosphere. Commonly, the oxidation kinetics curves follow the regulations of linear, parabolic, logarithmic and cubic [47].

2.2.2.1 Linear law

At high temperature, due to a fast adsorption of oxygen, an initial oxide film would be formed rapidly on the surface of the bare metals. If the oxide film cannot develop to be a protective scale, such as evaporating or spallation, the oxidation rate would be determined directly by the formation speed of the oxides. Thus, the growth rate of the oxide scale will be a constant, as shown below,

$$dy/d\tau = k \quad (2.14)$$

in which, y is the thickness of scale; τ is the oxidation time; *k* is a constant.

If taking the integral of Eq. (6), the following equation can be obtain,

$$y = k\tau + C \quad (2.15)$$

Thus, based on the Eq. (2.15), the thickness of scale possesses a linear relationship with exposure time. The integration constant (C) depends on the scale thickness at the initial stage of oxidation. If the oxidation starts from a bare metal without any oxides, the C could be equal to zero, and so,

$$y = k\tau \quad (2.16)$$

In general, it has been expressed with the mass gain in experiments,

$$\Delta m = k_1\tau \quad (2.17)$$

Actually, the scale growth of alkali metals and alkaline-earth metals show the linear law, such as the magnesium (Mg) oxidized at 503-575 ^{o}C. The linear regulation results from an invalid oxide scale, the oxidation rate is controlled only by the activation energy in the chemical reaction of the oxides.

2.2.2.2 Parabolic law

Once a continuous oxide film has been established on the surface of substrate, the further oxidation should be conducted via diffusion process, i.e., the cations diffuse outward and anions diffuse inward. The rate of the diffusion rate of these ions could be described with Fick's first law:

$$v_d = -D(d_c/d_y) \quad (2.18)$$

where D is diffusion coefficient; d_c/d_y is concentration gradient. If the oxidation process happens under a stable diffusion condition, the diffused ions won't accumulate at any sections of the scale, so the concentration gradient (d_c/d_y) could be replaced with the formula of (c_M-c_O)/y, and the Eq. (2.18) will be

$$v_d = -D(c_M/c_o)/y \quad (2.19)$$

in which c_M represents the concentration of oxygen at the interface of metal/scale; c_O represents the concentration of oxygen at the interface of scale/air.

Further assuming that the oxidation process would be dominated by oxygen inward diffusion, the c_M will equal to zero. In other word, due to a slow diffusion rate, all the oxygen diffused inside scale is consumed by the oxidation reaction, and the Eq. 2.19 should be written with the following formula,

$$v_d = Dc_o/y = v_O \quad (2.20)$$

Therefore, the oxidation rate (v_O) controlled by the diffusion process equals to the rate of diffusion, which is proportional to the concentration of oxygen in surrounding air and inversely proportional to the thickness of scale. Besides, the Eq. (2.20) proves that when the oxygen concentration is fixed, the v_O will be reduced with the increasing of the scale thickness at a given temperature, i.e.,

$$v_O \infty 1/y \quad (2.21)$$

If using the growth rate of the scale thickness to express the oxidation rate, the Eq. (2.21) changes to be next equation,

$$v_O = dy/d\tau = k'/y \quad (2.22)$$

Once to take the integral of Eq. (2.22),

$$\int ydy = k'd\tau, \text{ and then } y^2 = 2k'\tau + C \text{ or } y^2 = k\tau + C \quad (2.23)$$

where, k is the rate constant of parabolic; y is the thickness of scale; C is the integration constant.

In respect of most of common metals, the solid oxide scale with a compact structure would be formed during a wide temperature range. The diffusion rate of ions is relatively slow in the solid oxide scale, especially for the metal cations diffusion outward. Once the protective oxide scales form, the oxidation process basically shows a parabolic regulation and the oxidation rate will be decelerated with the increasing of scale thickness. However, based on actual measurements, a lot of metals were observed to deviate from the square parabolic law.

Usually, the Eq. (2.23) has been written as another common equation, as follows,

$$y^n = k\tau + C \quad (2.24)$$

In the case of $n < 2$, which indicting that the retardation of the diffusion did not increase proportionally with the growth of the scale thickness, the higher oxidation rate would be attributed to vacancies or some other defects in the scales and metals.

On the contrary, if the $n > 2$, it means that the retardation for the diffusion is stronger than the retardation caused by the growth of scale thickness. The formation of other new oxides which possess more compact structure than initial oxides would be one of the reasons, such as the spinel $Co(Al, Cr)_2O_4$.

2.2.2.3 Logarithmic law

In respect of the oxidations took place at a low temperature or room temperature, the formation rate of the oxide scales in several metals could be extremely rapid at the beginning, and then decrease to be a slow rate with the elongation of exposure time. This oxidation behavior follows the logarithmic and antilogarithmic regulations, in which the oxidation rate-scale thickness should be an exponential relation, and so

$$dy/d\tau = Ae^{-By} \quad (2.25)$$

$$dy/d\tau = Ae^{By} \quad (2.26)$$

in which, y is the thickness of oxide scale; τ is the exposure time; A, B are constant. Taking the integral of the above two equations, getting

$$y = k_1 \lg (k_2\tau + k_3) \quad (2.27)$$

$$1/y = k_4 - k_5 \lg\tau \quad (2.28)$$

the k_n represents constant.

Both the above two logarithmic and antilogarithmic regulations can only occur when the oxide scale is very thin, indicating that the retardation of oxidation is much stronger than the parabolic regulation. It's know that the oxidation of Fe obeys the logarithmic law at the temperature of 305 ^oC and 252 ^oC in air.

2.2.2.4 Cubic law

In a certain temperature range, the oxidation of some metals would follow the cubic law, such as Copper (Cu) at the temperature of 100 ^oC to 300 ^oC. The cubic regulation can be expressed with next formula,

$$y^3 = k\tau + C \quad (2.29)$$

where y is the thickness of scale; k is the constant of oxidation rate; τ is exposure time; C is a constant.

In general, the cubic law is only available for the short-term oxidation process, and occurs at a low temperature with the formation of a thin scale. The reasons for this characteristic may be associated with the transport process that passing from the space-charge region in oxides.

2.2.3 Influence of other alloying element on the oxidation behavior

As mentioned in above chapter, Cr is the main element which has been introduced into the Co-based alloys. In the most of Co–Cr alloys, in order to maintain a best oxidation resistance with the minimum parabolic rate constants, the content of Cr has to be adjusted within a maximum range of 20-25 (wt. %) and results in the formation of Cr_2O_3 scale and small amounts of CoO and spinel $CoCr_2O_4$. If decreasing the Cr content, the oxidized products is dominated by CoO which exhibits a faster oxidation rate. The formation of the Cr_2O_3 scale is not only depending on the content of Cr, but also on the atmosphere. Based on the reports focused on the oxidation behavior of Co-Cr alloys at 1000 ^oC, 35 wt. % Cr is needed to maintain a continuous Cr_2O_3 scale in oxygen at 760 torr, even though 20-25 wt. % Cr is enough for the formation of Cr_2O_3 scale in air at 1 atmosphere [20, 48, 49]. The Cr_2O_3 scale has been utilized as a main protective scale in the conventional Co-based alloys to prevent further oxidation. However, if the service temperature has risen above 900 ^oC-950 ^oC, the Cr_2O_3 scale will be decomposed with the volatile CrO_3 [21]. Alumina has been considered to be more protective scale than other conventional metal oxide scale due to its lower growth rate and nonvolatility at elevated temperature, but the production of alumina-forming in the alloys has high-demanding on alloys composition with high Al content.

In respect of Co-based alloys, the development of alumina scale also has been conducted. For example, Irving, et al, investigated the oxidation behavior of Co-Al binary system at 1000 ^oC [20]. They found that it's necessary to add the aluminum content of 10-13 wt. % to maintain the formation of a continuous Al_2O_3 scale. However, according to the reference that the Co-based superalloys usually cannot

form an alumina protective oxide layer in service, since the Al addition is generally deleterious effect on mechanical properties and no sufficient aluminium could be introduced. Interestingly, it has been claimed that the addition of Cr to Co-Al base alloys markedly reduced the level of Al required in the ternary alloy below that required in the binary to form a continuous external scale of Al_2O_3 [20].

Wallwork and Hed [28] summarized the oxidation behavior of Co-Cr-Al alloys via a mass of oxidation experiments in oxygen at 760 torr and the temperature from 1000 ^oC to 1200 ^oC. They find that the oxide scales in the Co-Cr-Al system could be divided to be four sections with the increasing of Al and Cr content, i.e., (1) With a low addition of Al/Cr, the scale is dominated by CoO, with possibly some Cr/Al in solution; (2) A duplex scales is developed with the increasing of Cr/Al concentration, an outer layer of CoO scale and an inner CoO layer with the distribution of $Co(Cr, Al)_2O_4$ spinel particles; (3) The formation of CoO oxide is suppressed if more Cr/Al is added, and an continuous Cr_2O_3 forms at external layer, with several Al_2O_3 particles at inner band; (4) An external Al_2O_3 could be established at surface if the sufficient content of Cr/Al is introduced. Beside, based on the abundant research work on the oxidation behaviors of Co-Cr-Al ternary system, the Co-Cr-Al oxide map at 1000 ^oC has also been achieved, as shown in **Fig 2.5**, in which the supposed four sections has been quantitatively divided with the content of Cr/Al.

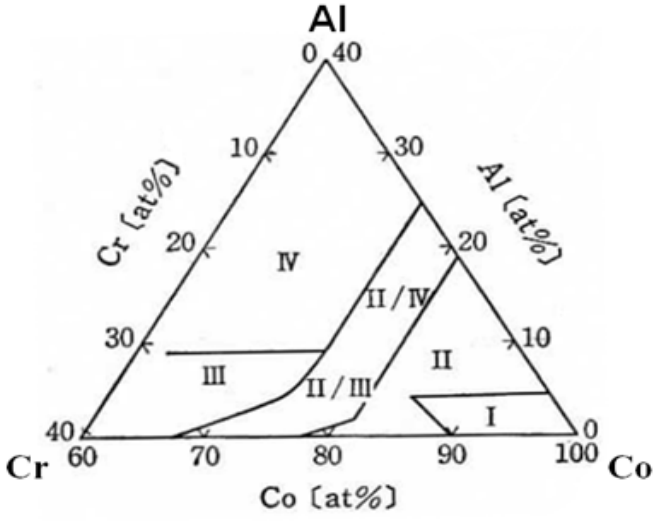

I: CoO; **II**: $CoO/CoAl_2O_4/CoCr_2O_4$;
III: External layer of Cr_2O_3, internal Al_2O_3;
IV: Al_2O_3.

Fig. 2.5 The oxide map of the Co-Cr-Al system at 1000 ^oC.

Besides, the effect of a lot of other element additions on the oxidation behavior of Co-based alloys also have been investigated, as shown in next **Table 2.5**, in which the substrate alloy is Co-(20-30)Cr (wt. %) alloys and the chromia is the main oxide product [50].

Table 2.5 The dissociation pressures of some typical oxides at 1000 ^{o}C.

Alloying element	Probable effect on the oxidation behavior
Iron	Beneficial; accelerates spinel formation
Manganese	Beneficial; accelerates spinel formation
Carbon	Deleterious; consumes Cr content
Yttrium	Beneficial; improves scale adherence
Vanadium	Harmful, even at 0.5%
Niobium	Harmful, even at 0.5%
Nickel	Slightly deleterious
Tungsten	Harmful at temperature above 1000 ^{o}C
Molybdenum	Deleterious; forms volatile oxides
Titanium	Innocuous at low level
Zirconium	Innocuous at low level

W.J. Quadakkers et al. also proved that the presence of the Y_2O_3 decreased oxide growth rates by reducing cation diffusion in scales and causing the oxides on the Fe-based ODS alloys to grow mainly by oxygen grain boundary transport [51]. In respect of the γ'-Co_3(Al, W) precipitate strengthened Co-Al-W system, as mentioned in above sections, since the γ'-phase is available only at a narrow composition range, there are not so much other alloying elements could be introduce to the system. For instance, the Cr addition which is beneficial to corrosion resistance has been determined to have a deleterious effect on γ' stability [9].

2.3 Scientific aims of the present work

Oxide dispersion strengthening is wildly used to develop high-temperature superalloys, such as Fe- and Ni-based ODS superalloys [12-16]. Besides their superior creep resistance and favorable high-temperature strength, ODS superalloys show better oxidation resistance than the ODS-free alloys with the same basic composition, which has been frequently proved with a large number of reports about oxidation behavior of Fe- and Ni based ODS superalloys [17-19]. However, a comparable attention on the development of Fe-based and Ni-based ODS superalloys has not been paid for Co-based ODS superalloys, and even no literatures could be referred about the high-temperature oxidation of Co-based ODS superalloys.

Nowadays, the Ni-based superalloys are widely used for the gas turbine blades and vanes, however their strength is lost at temperature beyond 1000 °C due to γ' dissolution; thus service temperature is restricted to 900 °C. Co-based alloys possess high hot corrosion resistance than Ni-based alloys, which is more suitable for the atmosphere of gas turbines. The conventional Co-based alloys is strengthened by carbides precipitate and latterly developed γ'-Co3(Al, W) precipitate, but both of these method should be invalid due to a poor stability at elevated temperature up to 900 ^{o}C. It's significant to enlarge the limitation of the using temperature in the Co-based alloys. Focusing on dispersed oxide particles, which are extremely high thermal-stability at the temperature above 1000 ºC; thus it could be trusted that the oxide dispersion strengthening (ODS) is an effective approach to increase service temperature of Co-based alloys beyond 1000 ºC. Consequently, the goal of this research is to develop innovative Co-based ODS superalloys, which should be utilized at elevated temperature up to 1000 ºC.

Chapter 3 Specimen fabrication

3.1 Investigated compositions

In order to develop Co-based ODS superalloys with excellent mechanical properties and oxidation resistance at the temperature above 1000 ºC, a strong ODS effect with the dispersion of fine secondary particles and the alumina-forming scale are the primary objects in the design of the novel Co-based ODS superalloys. Aimed at developing alumina-forming Co-based superalloys, an incremental aluminum content of the 5 wt.%, 10 wt.% and 15 wt.% were added into the designed Co-based superalloys, and 20 wt.% chromium was also introduced to promote the formation of alumina scale according to the reports on oxidation behavior of conventional Co-based alloys [20]. Based on the Co-Cr-Al phase diagram computed with the thermodynamic software Pandat, as shown in **Fig. 3.1**, the basic composition of Co-20Cr-(5, 10) Al (wt. %) system are composed with the Co solid solution phase with fcc structure and B2 phase with bcc structure, which offers the guarantee for a good ductility and a favorable strength, respectively. However, the volume fraction of B2 phase was increased significantly with the Al content from 5 wt. % to 10 wt. %, i.e., in contrast with an almost equal volume fraction of B2 and fcc phase in 10Al, the fcc phase is dominant in the 5Al. Besides, the Hf was added to refine the oxide dispersoids, based on the reports of Zhang et al that Hf is effective to reduce the oxide particles size by generating $Y_2Hf_2O_7$ particles [23], which is expected to provide a powerful guarantee for an improved strength at elevated temperature. In addition, since the advantages of the Cr and Y_2O_3 addition for the increasing of oxidation resistance in the Fe-based ODS superalloys, the samples without Cr and Y_2O_3 addition also has been prepared to investigate the effect of Cr and Y_2O_3 on the oxidation behavior of the Co-based ODS superalloys. All the investigated compositions in present work have been listed in following Table 3.1, in which the abbreviations of 5Al, 10Al and 15Al are used to define each alloy with the Al concentration from 5 wt.% to 15 wt.%.

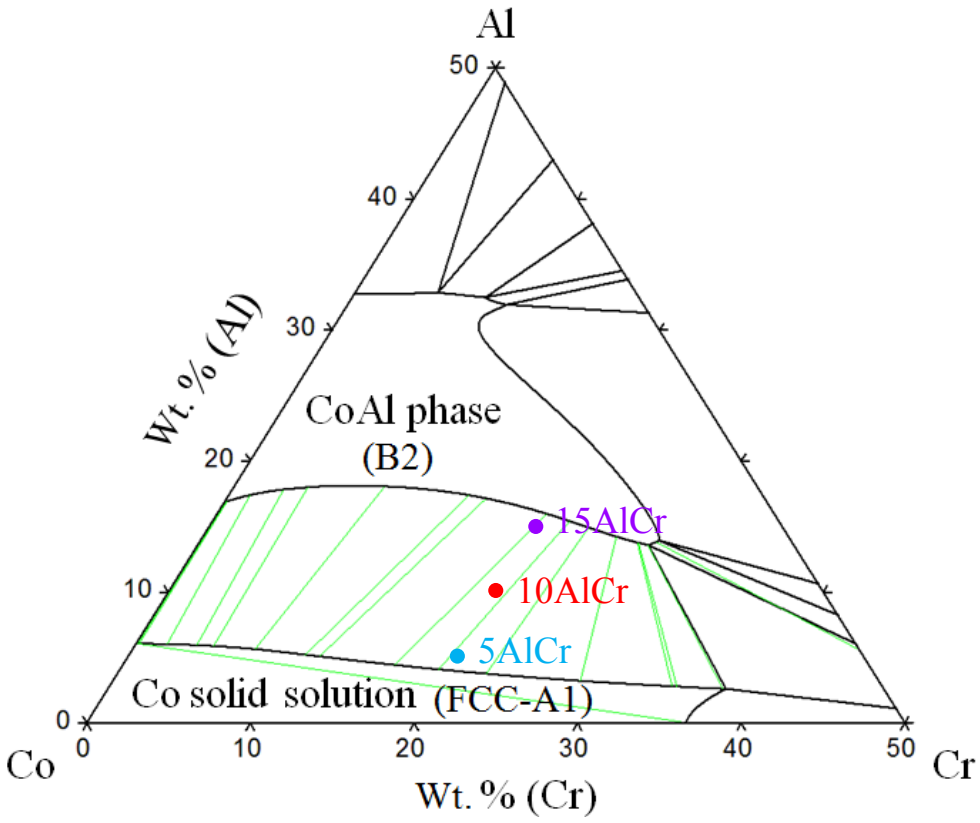

Fig. 3.1 The ternary Co-Cr-Al phase diagram calculated with Pandat software at 1100 ^{o}C.

Table 3.1 Nominal compositions of the investigated alloys and utilized abbreviations.

Alloys	**Elements, wt. %**				
	Co	**Cr**	**Al**	**Hf**	**Y_2O_3**
5AlCrY	Bal.	20	5	2.4	1.5
5AlCr	Bal.	20	5	0	0
10AlCrY	Bal.	20	10	2.4	1.5
10AlY	Bal.	0	10	2.4	1.5
10AlCr	Bal.	20	10	2.4	0
15AlCrY	Bal.	20	15	2.4	1.5

3.2 Fabrication process of alloys

All the investigated alloys in present work were basically fabricated with the following processes; Firstly, all the elemental powders were mixed and mechanically alloyed (MAed) for 48h under argon gas atmosphere using a planetary type ball mill (Fritsch P-5). Subsequently, the mechanically alloyed powders were consolidated in a graphite mold by spark plasma sintering (SPS) at 1100 ºC and 45MPa for 2h, an then followed by a hot-rolling at 1200 ºC into samples in 3 mm thickness. The final annealing was conducted at 1200 ºC for 1 h under vacuum of 10^{-4} Torr. **Fig. 3.2** schematically illustrates the detailed processes.

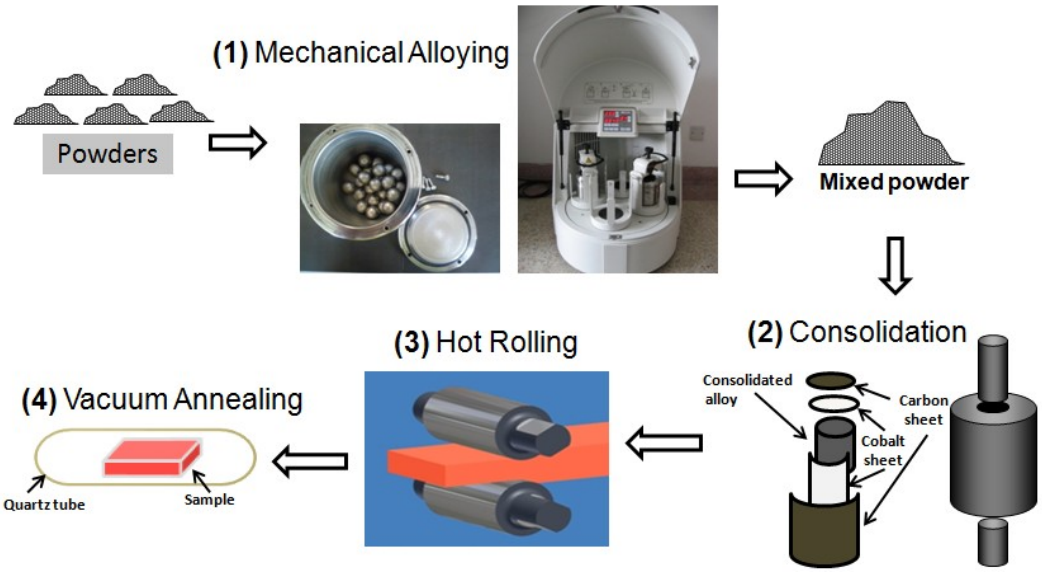

Fig. 3.2 The simple flow chart for the fabrication of the Co-based ODS superalloys.

3.2.1 Mechanical alloying

Mechanical Alloying (MA) is one of the most commonly used methods to prepare the powders of the oxide dispersion strengthened (ODS) superalloys. Conventional melt processing techniques cannot be applied to fabricate ODS superalloys, due to the extremely different density: density of Y_2O_3 is half of that of Co-alloy, which induces separation at the melting processing. MA is a process of high-energy ball milling and able to form nano-crystalline structures via the milling of powders, which has been claimed in many reports. On the effect of high-energy ball milling, particles are subjected to repeated flattening, cold welding, fracturing and rewelding, leading to a

severely plastic deformation repeatedly. The main function of MA is to break up the chemical bonds in the Y_2O_3 particles and to force the Y, Hf and O to compound and incorporate into the Cobalt matrix [23].

The detailed MA parameters used in present work are listed as follows,

Type of machine: FRITSCH Pulverisette 5 planetary ball mill;

Rotation speed: 300 rpm;

Total time: 72 hours (48 h milling and 24 h pause);

Ball/Powder ration: 10:1 (weight);

Milling atmosphere: Argon.

3.2.2 Consolidation

All the investigated samples were consolidated with spark plasma sintering (SPS). The SPS process depends on the electrical spark discharge phenomenon. High-temperature spark plasma appears in the microgaps between the powder particles, a local high temperature state of over 1000 ^{o}C momentarily occurs. This causes vaporization and the melting of the surfaces of the powder particles during the SPS process [52], resulting in a rapid consolidation with loading pressure. Besides, SPS is one of the consolidation methods to produce bulk materials with densities close to their theoretical values. In the present work, the mechanically alloyed powders were consolidated in the graphite mould with the dimension of 15 mm diameter and 30 mm length by (SPS). The SPS was carried out at 1100 ºC and 45MPa for 2h in vacuum of 6 Pa.

3.2.3 Hot rolling

In the process of consolidation, a pressure of 45MPa was loaded on the bulk materials along the vertical direction. The hot rolling is performed to further compact samples with loading shear stress, which could further compact bulks via eliminating residual pores. Besides, a high temperature at rolling process could avoid the occurrence of cracks, especially for the Co-based alloys with high aluminum addition,

which possesses a high brittleness with a high volume fraction of CoAl (B2) phase.

Before rolling process, the bulk materials would be loaded into a steel case and then heated to 1200 ºC with a super-furnace, followed by the rolling with a decrease of 1 mm per time. After each rolling, the samples would be reheated to 1200 ºC and then rolling again, until a final thickness of 3 mm. In this place, one point should be emphasized that the 15AlCrY samples were severe cracking after the hot-rolling, as shown in the **Fig. 3.3**, the processability is quite low with a relatively high volume fraction of CoAl phase.

Fig. 3.3 The 15AlCrY sample after hot rolling at 1200 ^{o}C.

3.2.4 Annealing

Followed the hot rolling, the final annealing was conducted at 1200 ºC for 1h under vacuum of 10^{-4} torr to release machining stress.

Chapter 4 Microstructural Characterization

4.1 Experimental details

The novel Co-20Cr-(5, 10, 15)Al-2.4Hf-1.5Y_2O_3 (wt. %) ODS superalloys were designed and fabricated by MA, SPS, hot rolling and final annealing at 1200 ºC. The crystalline morphology and the components distribution of MA powders were detected using X-ray diffraction (XRD, Philips X' Pert PRO) and electron probe micro-analyzer (EPMA, JEOL JXA-8530F) mapping. The microstructures of the annealed samples were observed by scanning electron microscope (SEM, Carl Zeiss Cross Beam 1540 EsB), and the elements distribution was quantitatively analyzed using electron probe micro-analyzer (EPMA, JEOL JXA-8530F). The distribution of nano-sized oxide particles was analyzed using transmission electron microscopy (TEM, FEI Tecnai T20 and FEI Titan G2 80-200), particularly their distribution between different phases. In addition, atom probe analysis was carried out through laser-assisted wide angle three-dimensional tomographic atom probe (LAWATAP) which utilized ultraviolet femtosecond laser with the wavelength of 343 nm. The nano-scale needle-like testing samples were prepared by electrochemical polishing.

4.2 Results

4.2.1 Morphology of MA powder

Fig. 4.1 shows the EPMA mapping of the cross-sectional microstructure of MA-ed 5AlCrY powders. The size of the final powder mixture is coarsened to more than 50 μm as compared with the original cobalt powder size (1.5 μm) due to repeating fracture and cold welding during MA. EPMA maps obviously indicate that most elements dissolved uniformly into the cobalt matrix. These results are confirmed by XRD analysis (**Fig. 4.2**), which shows that the peaks characteristic for Al, Cr, Hf and Y_2O_3 cannot be clearly detected. Decomposition of thermally very stable Y_2O_3 particles by the high energy ball milling has been studied in our group for Co-based ODS superalloys [23].

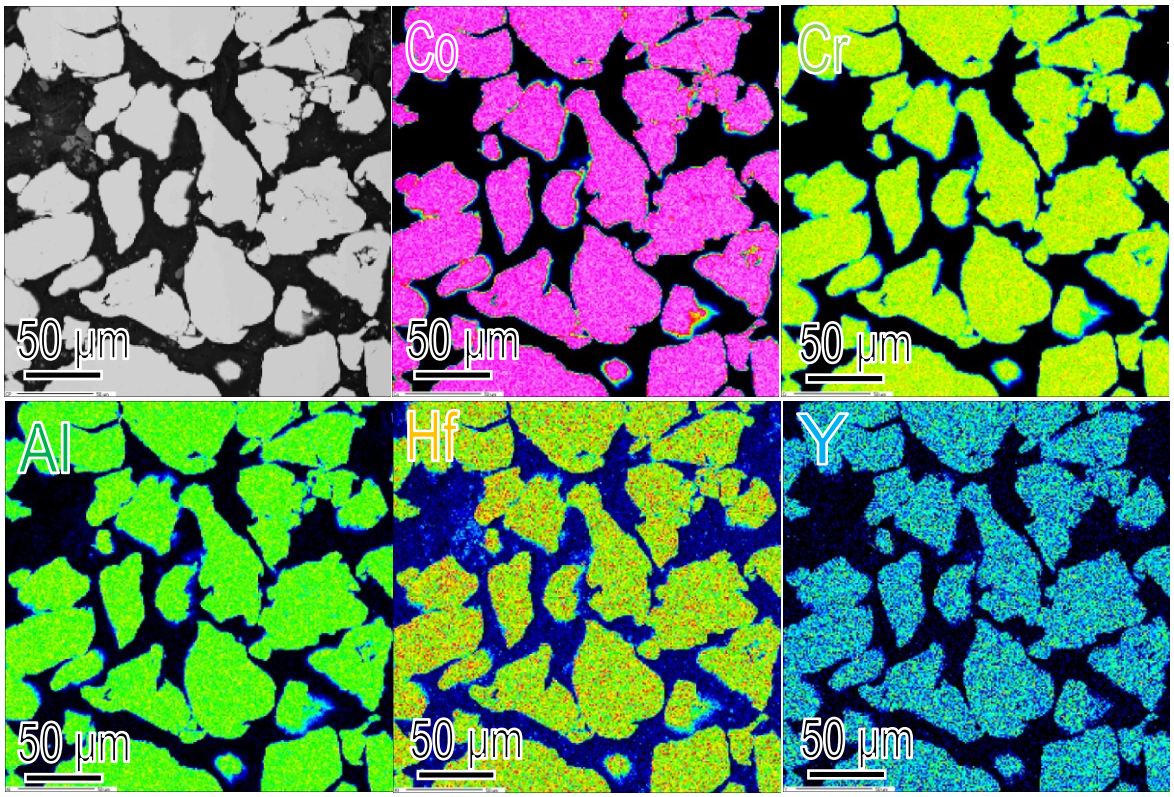

Fig. 4.1 EPMA element maps obtained from MA powders of 5AlCrY specimen.

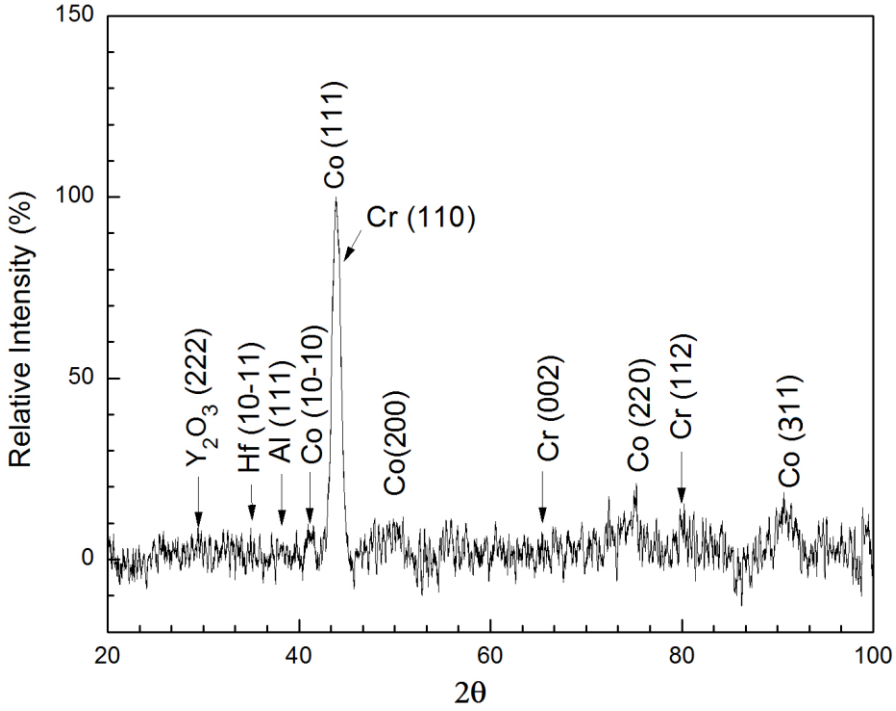

Fig. 4.2 XRD pattern of 5AlCrY powder milled for 48 h.

4.2.2 Microstructural characterization

Fig. 4.3 shows the results of elemental analyses of the 5AlCrY sample after SPS consolidation of the MA powder, followed by the hot-rolling and the final annealing. From the back scattered (a) and the secondary electron images (b), the 5AlCrY sample consists of three regions; i.e. the fine dark grey region with 0.2-0.4 μm scale marked by frame 1, the light grey matrix marked by frame 2 and the coarse light grey regions corresponding to frame 3. The phase 1 possesses high Al concentration according to the element map revealed in **Fig. 4.3** (c), which is considered to be B2 phase. Since dense secondary phases with tiny white imaging contrast can be obviously observed in the region 2 (but not in 3) in **Fig. 4.3** (b), and their dispersion is consistent with the heterogeneous distribution of Y, Hf and O shown on the element maps in **Fig. 4.3** (d) and (e), these are oxides particles distributed densely in the matrix 2, but sparsely in the coarse region 3. The oxide particles decomposed by the ball milling and then precipitated again, when the MA powers had been consolidated at 1100 ºC [23].

Fig. 4.4 shows the elemental analyses for the 10 AlCrY sample. Frame 1 is the B2 phase due to enrichment in Al. Larger area of the frame 1 is consistent with a higher volume fraction of the B2 phase predicted by the phase equilibrium because of increasing Al content from 5 to 10 wt% Al. The B2 phase contains a large number of oxide particles resulting from the participation of Y and Hf oxides in the area of frame 1 shown in **Fig. 4.4** (d) and (e). The matrix with abundant particles and the coarse smooth area with few particles have been also found in the alloy containing 10 wt.% Al, as shown in the frames in **Fig. 4.4** marked 2 and 3, respectively.

In addition, even the 15AlCrY alloys cracked severely during hot-rolling process, the microstructure observation was still conducted for some small parts of the hot-rolled 15AlCrY alloys. The SEM images and corresponding EPMA mapping are exhibited in **Fig. 4.5**, in which the same three areas with the 5AlCrY and the 10AlCrY samples were detected. However, due to the significant increasing of B2 phase volume fraction, a very limited grey area could be observed, as marked with frame 2.

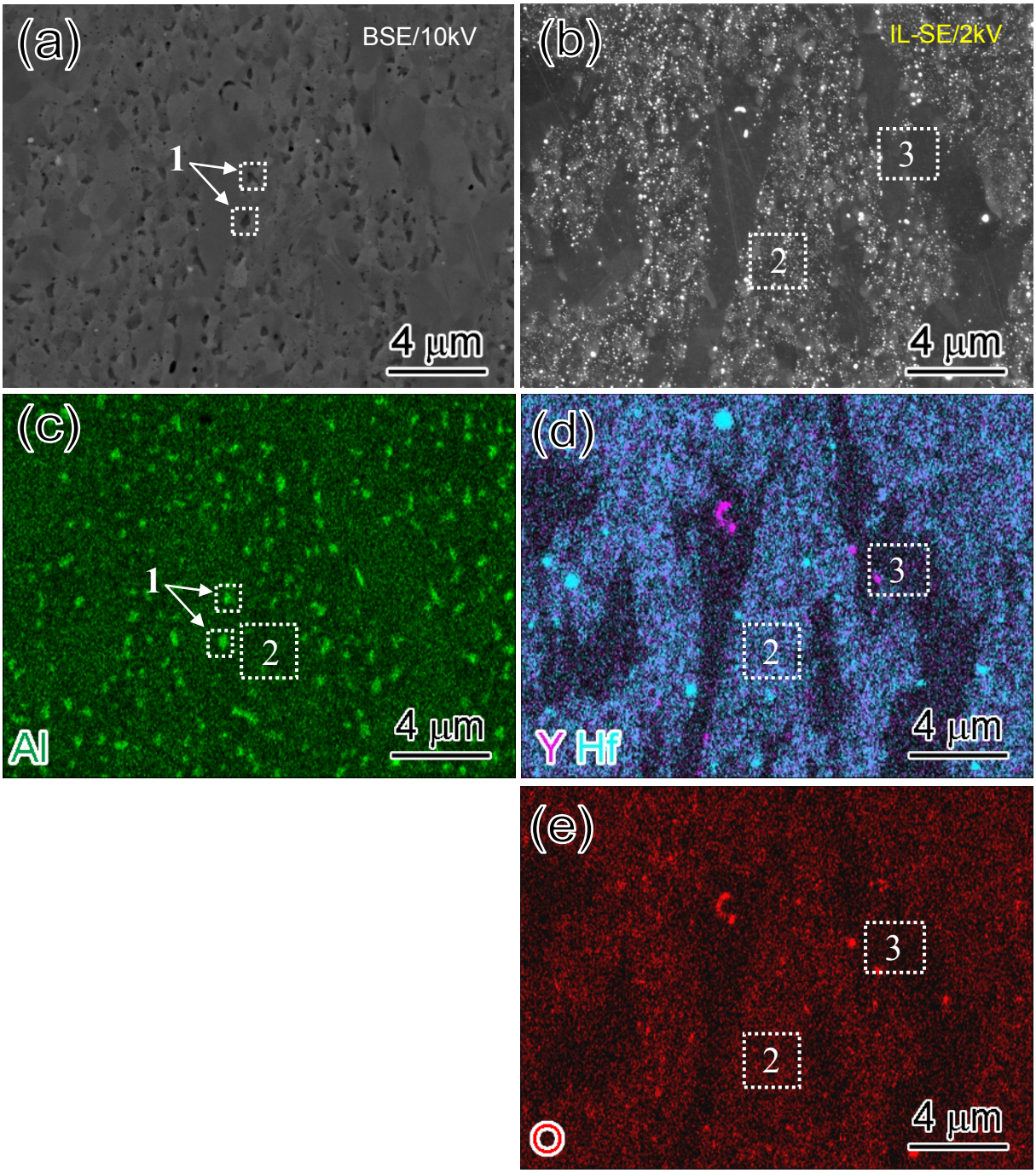

Fig. 4.3 SEM images of backscattered electron (a) and secondary electron (b) obtained from the same location in 5AlCrY sample, (c)-(d) are corresponding EDS element maps of Al, Y and Hf and O.

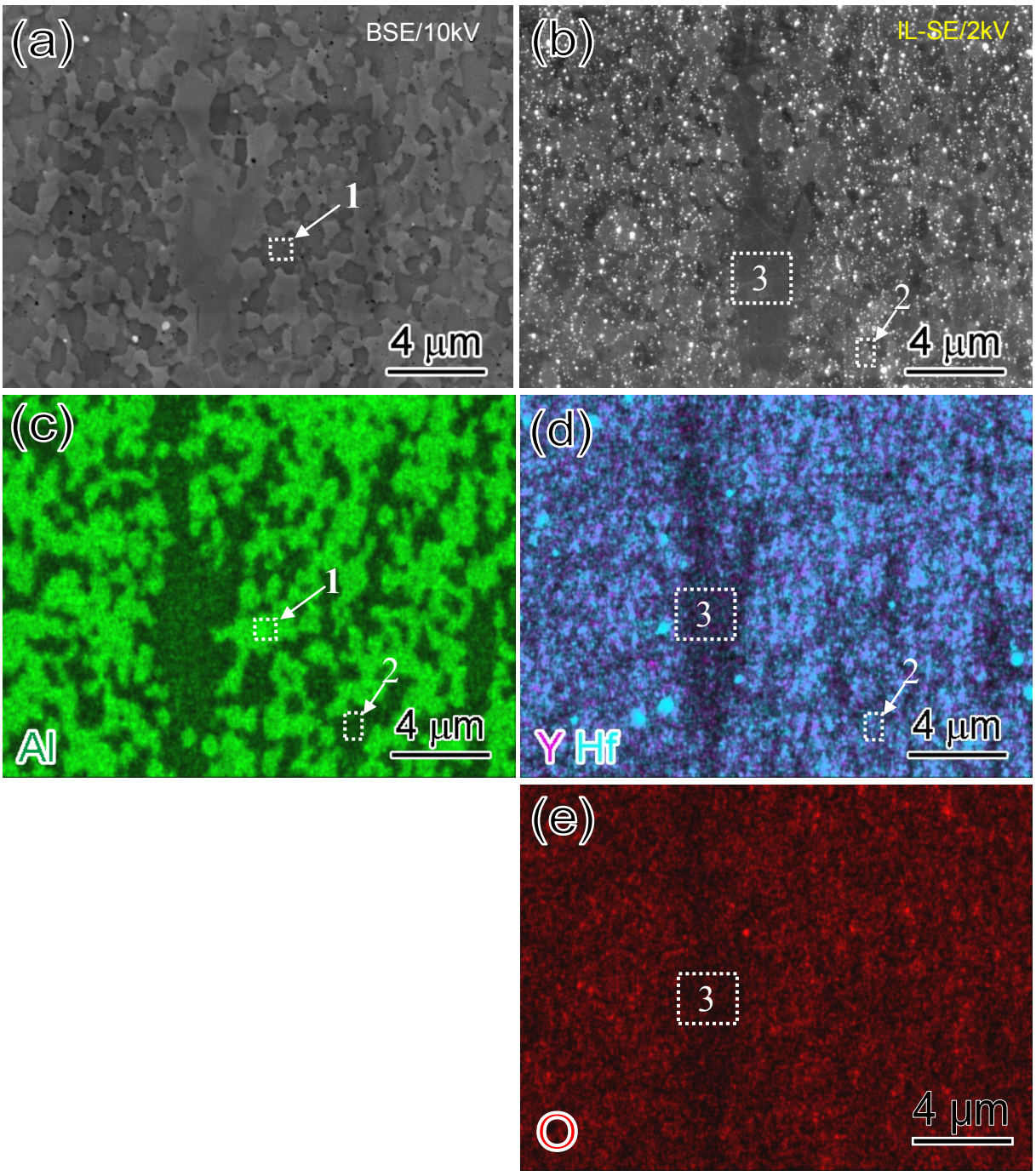

Fig. 4.4 SEM images of backscattered electron (a) and secondary electron (b) obtained from the same location in 10 AlCrY sample, (c)-(d) are corresponding EDS element maps of Al, Y and Hf and O.

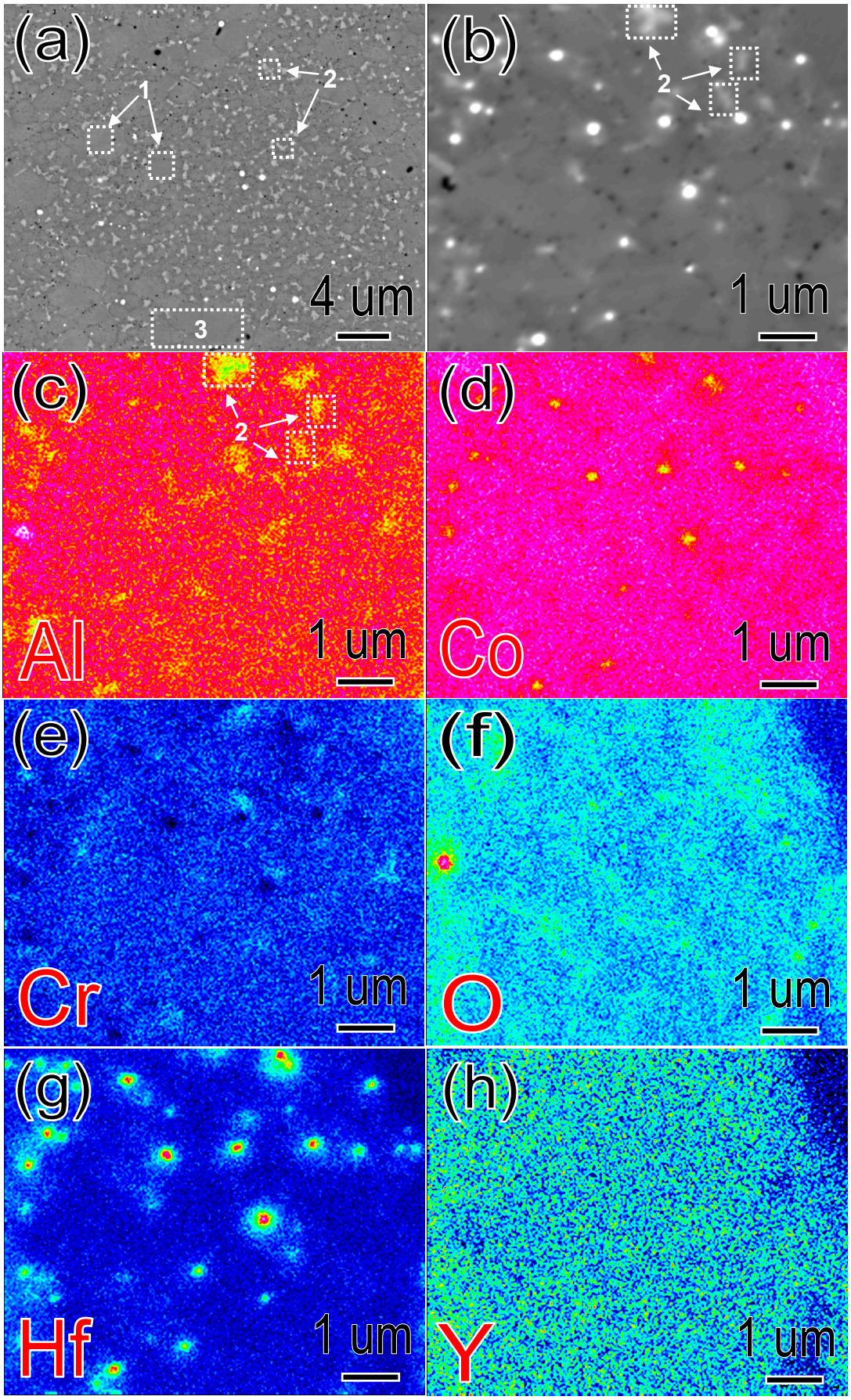

Fig. 4.5 SEM images obtained from the 15AlCrY sample, (c)-(h) are corresponding EPMA elemental maps of Al, Co, Cr, O, Hf and Y.

Fig. 4.6 (a) and (c) show the bright field TEM images of the 5AlCrY and 10AlCrY, and the corresponding aluminum elemental maps are shown in **Fig. 4.6** (b) and (d), respectively. The red color areas enriched with aluminum correspond to the B2 phase. The three different regions of the 5 and 10 wt% Al shown in **Fig. 4.3** and **Fig. 4.4** were detected in **Fig. 4.6**, namely the areas enriched in Al, the matrix filled with particles and the coarse smooth areas separately noted with 1, 2 and 3. Furthermore, the selected area diffraction (SAD) pattern of each region has been performed and their results are shown in **Fig. 4.6** (a) and (c). From the SAD pattern, the region 1 was confirmed to be the B2 phase, and the matrix 2 and the coarse smooth areas 3 were proved to be the fcc phases.

The volume fraction of the fcc matrix and the B2 phase computed with Pandat software is listed in **Table 4.1**. In addition, **Fig. 4.7** shows the concentration of each element predicted with the Pandat software in the fcc matrix and the B2 phase, as compared with the results of EPMA measurement. Both, the software analysis and the EPMA measurement, are almost consistent in predicting volume fraction and composition. The mechanical alloying including Y_2O_3 powder was able to produce almost the same results as those obtained for a thermal equilibrium condition in the Co-20Cr-(5,10)Al ODS superalloys.

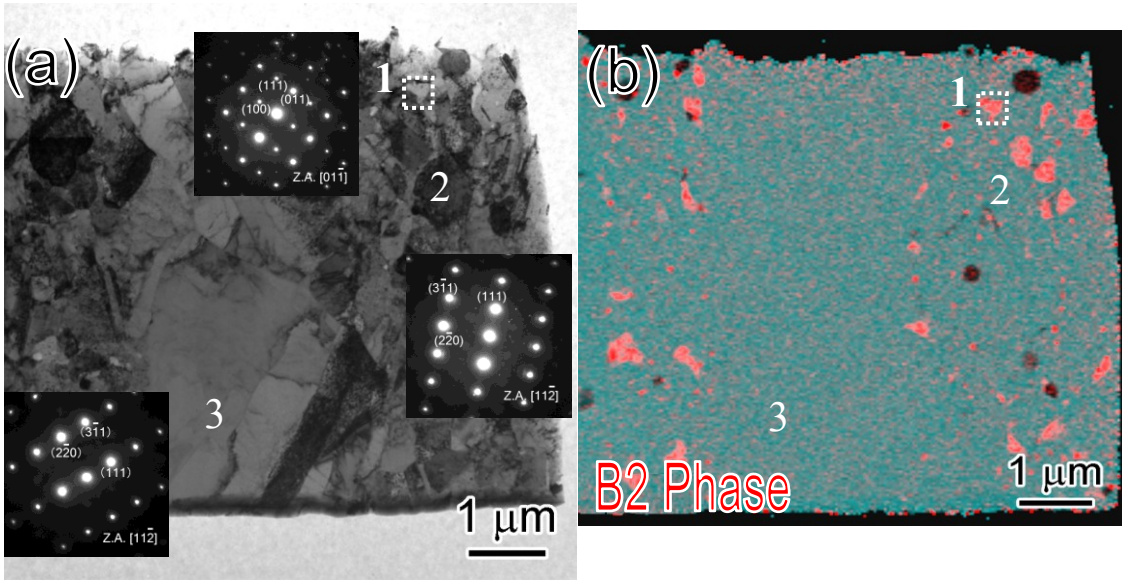

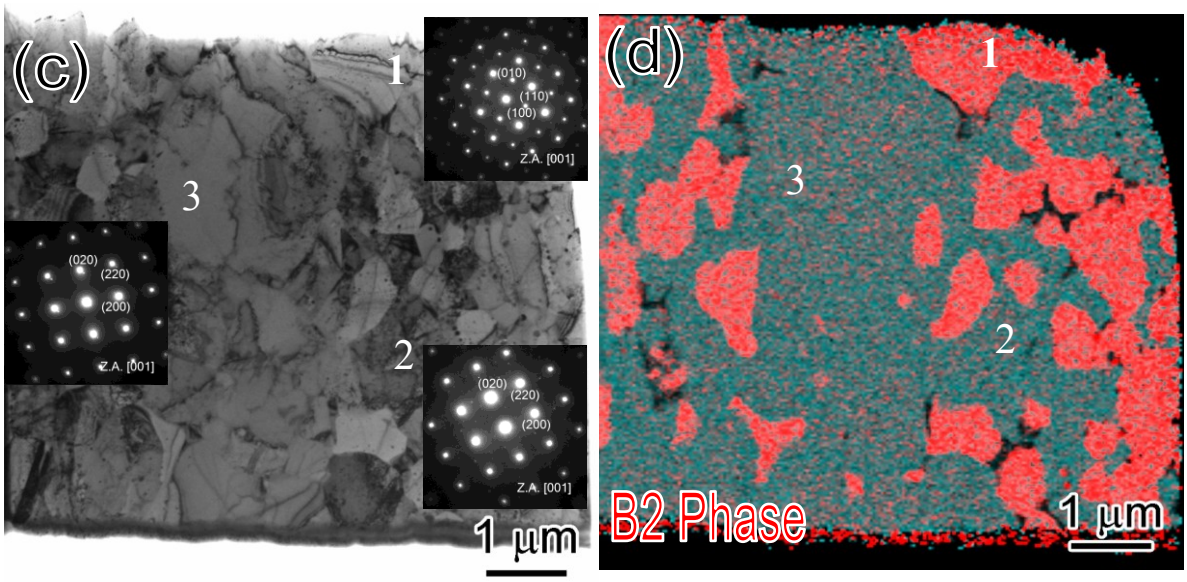

Fig. 4.6 TEM images and corresponding EDS element maps, (a), (b) for 5AlCrY and (c), (d) for 10AlCrY, respectively: Al distribution is presented by red color.

Table 4.1 Volume fraction of FCC phase and B2 phase computed by Pandat software code

Pandat	5CrYA1	10CrYAl
Phase FCC, %	90.4	45.7
Phase B2, %	9.6	54.3

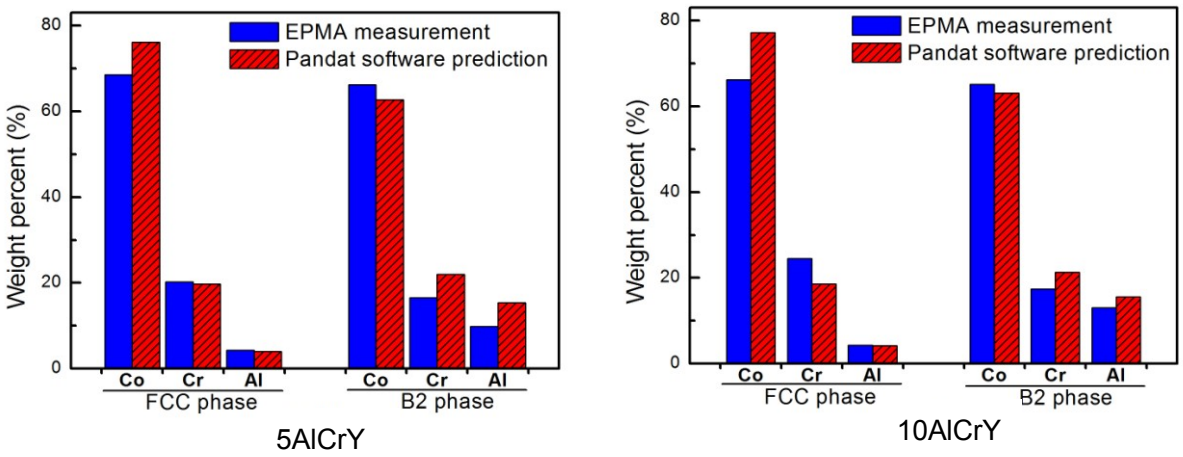

Fig. 4.7 The comparison of composition about FCC matrix and B2 phase of 5 AlCrY and 10 AlCrY samples measured via Pandat calculation and EPMA analysis, respectively.

4.2.3 Oxide particle characterization

Fig 4.8 (a) and (c) show HAADF-STEM images of the alloy containing 5 and 10 wt% Al, respectively. All phases, the matrix fcc, the B2 phase and the coarse fcc phase without oxide particles can be distinguished by the image contrast. According to the corresponding EDS maps obtained for Al, Hf, Y, O, as shown in **Fig. 4.8** (b) and (d), most of coarse oxide particles are mainly dispersed along grain boundaries and grain boundary triple junctions, whereas some of the fine oxide particles are located within grains.

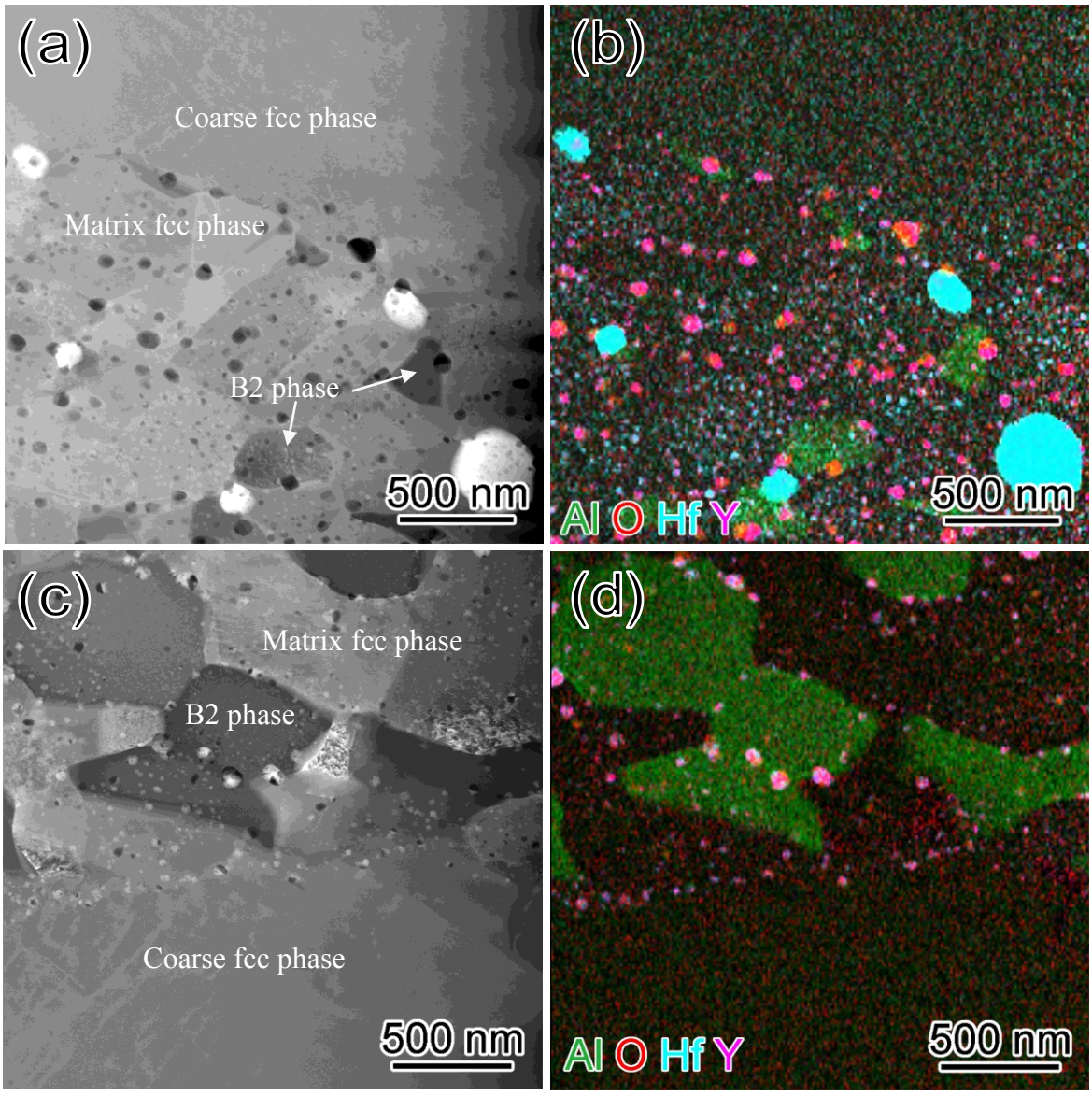

Fig. 4.8 HAADF-STEM images obtained in 5AlCrY (a) and 10AlCrY (c), (b) and (d) show corresponding EDS elemental maps.

Several larger white particles in **Fig. 4.8** (a) could be observed, and their dispersion is consistent with the Hf distribution in **Fig. 4.8** (b), which means the particles possess high Hf concentration, and also the presence of O and Y has been proved in these particles with EDS analysis.

Fig. 4.9 presents 3DAP maps of Al, Y, Hf and O elements in the fcc matrix of the 5AlCrY sample: Both, Al enriched oxide (Al_2O_3), and Y-Hf enriched oxide are observed. The size of the Y-Hf oxide particles is 5 nm in average, and they are finer than the Al_2O_3 particles except for one situated close to an Al_2O_3 particle. The 1-D compositional profiles along the larger Y-Hf oxide particle situated close to the Al_2O_3 and along a fine one are presented in **Fig. 4.9** (c) by introducing the cuboids with light blue and pink color, respectively. The composition of the coarser Y-Hf oxide particle as well as the fine one is calculated as Co-7.7Cr-17.6Al-10.7Hf-3.1Y-46.1O (at%) and Co-10.3Cr-7.7Al-6.6Hf-9.1Y-25.2O (at%) respectively, which are close to the compositions of $Y_2Hf_7O_{17}$ and $Y_2Hf_2O_7$ reported in the reference [23]. **Fig. 4.9** (d) shows the proximity diagram analyzed across the Al isoconcentration surface of an Al_2O_3 particle, which demonstrates that the boundary between the Al_2O_3 and the fcc matrix is enriched with Y and Hf.

Fig. 4.10 shows 3DAP maps of Al, Y, Hf and O distribution in the B2 phase of the 10AlCrY sample. It is noticed that the average size of Y-Hf particle in the B2 phase is 12 nm, and it is significantly larger than that in the fcc matrix (5 nm). The 1-D compositional profile across the Y-Hf oxide particle has revealed that Hf element (green line) is relatively enriched at the center, and Y element (blue line) is enriched at the periphery of the particle. The composition of a central part and a peripheral region shown in **Fig. 4.10** (c) is calculated as Co-13.0Cr-1.7Al-14.3Hf-5.7Y-49.2O (at. %) and Co-13.1Cr-13.2Al-7.7Hf-6.3Y-27.1O (at. %), which correspond to $Y_2Hf_7O_{17}$ and $Y_2Hf_2O_7$ compositions [23,26], respectively. This spherical core-shell structure of the Y-Hf oxide particle is schematically illustrated in **Fig. 4.10** (d).

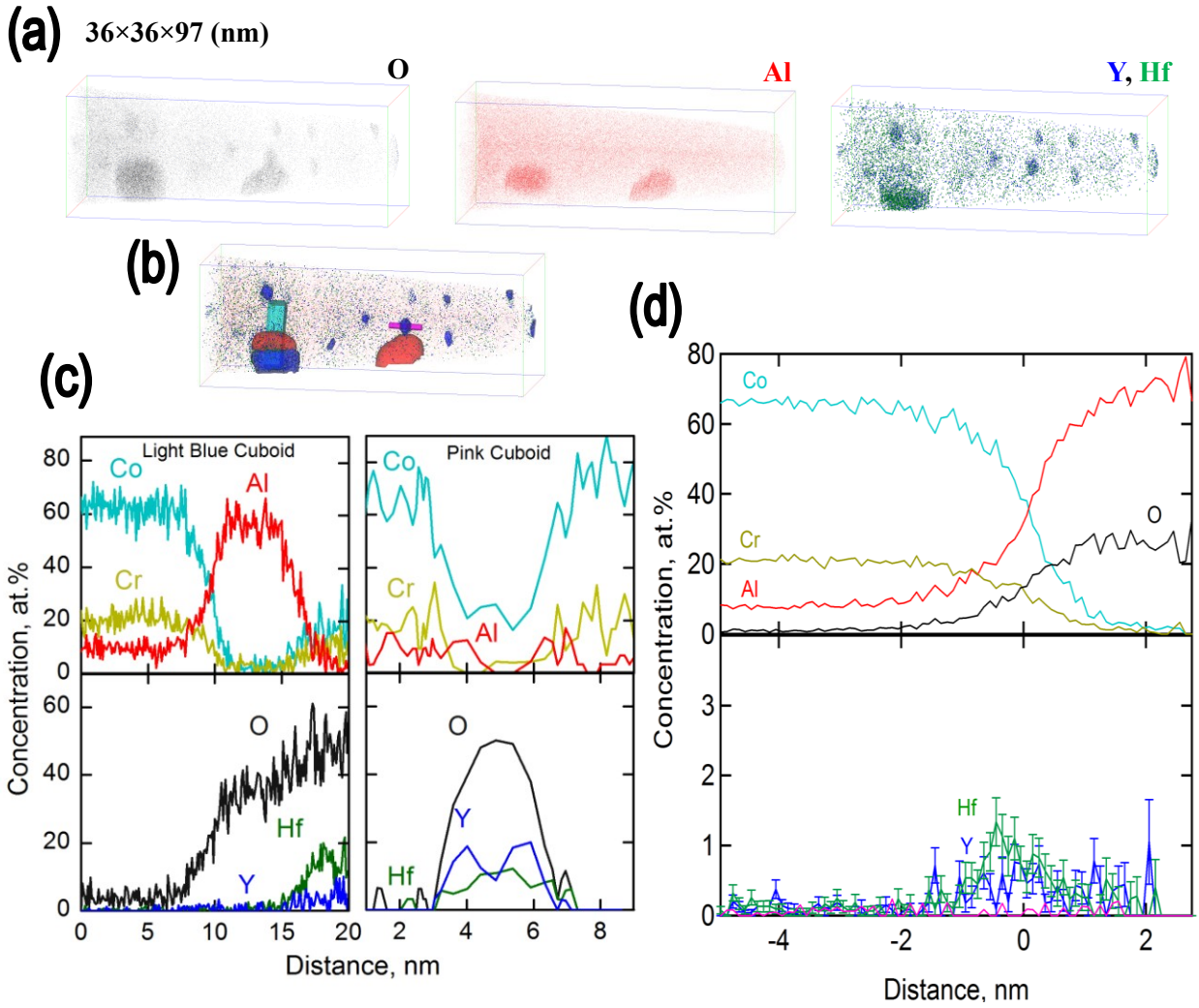

Fig. 4.9 The 3DAP atoms maps (a) and (b) obtained in fcc phase in 5 AlCrY, (c) shows 1D compositional profile along the longitudinal axis of the selected two cuboids in (b), (d) is proximity diagram across the Al isoconcentration surface of one Al_2O_3 particle taken from the bottom of (b).

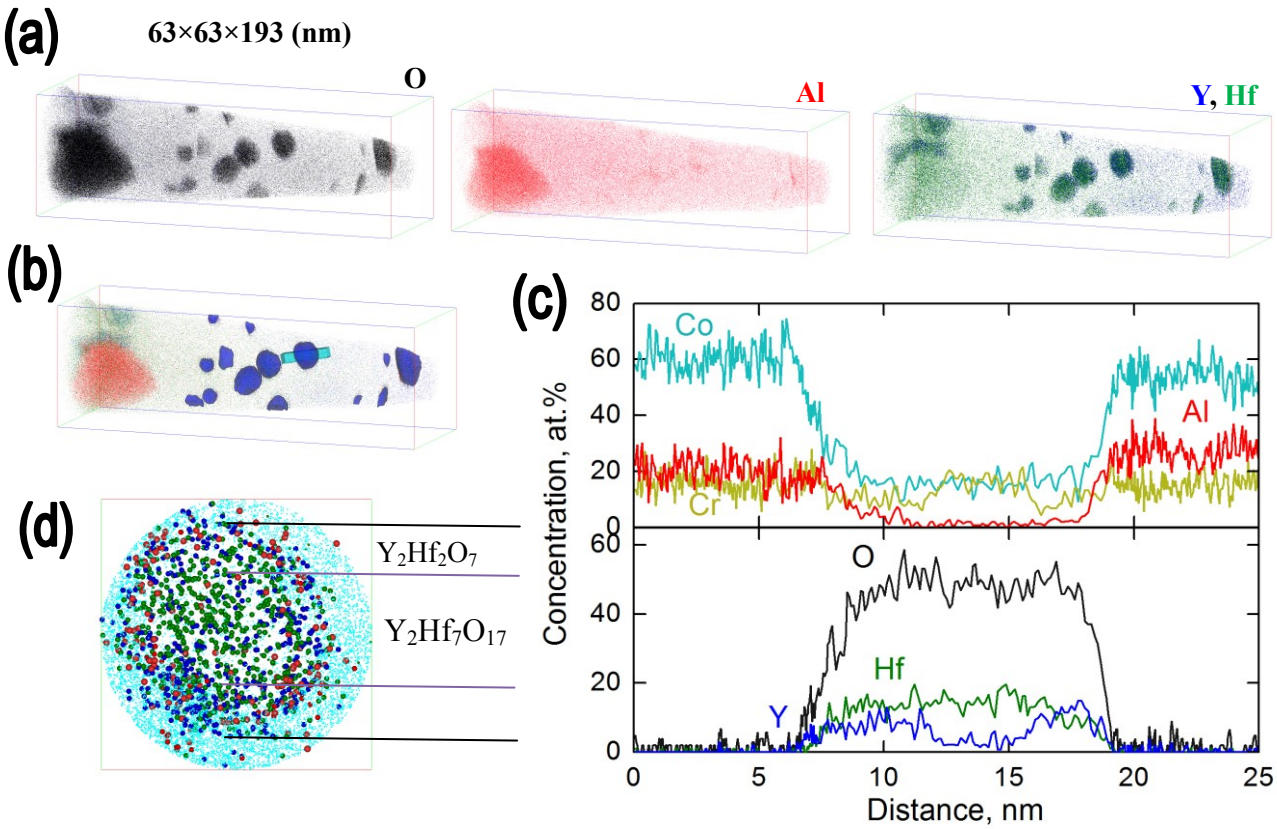

Fig. 4.10 The 3DAP atoms map (a) (b) obtained in B2 phase in 10 AlCrY, (c) is 1D compositional profile along light blue cuboid shown in (b), (d) exhibits core-shell structure consisted of $Y_2Hf_7O_{17}$ in the center and $Y_2Hf_2O_7$ at the periphery.

4.3 Discussion

It was verified by the microstructural characterization of the Co-20Cr-(5,10)Al ODS superalloys that composition and volume fraction of the Co-based solid solution in the fcc matrix and the B2 phase for the 5AlCrY and the 10AlCrY samples are almost consistent with the Pandat software prediction. This finding means that a thermal equilibrium condition can be attained in the process of SPS consolidation, hot-rolling and final annealing, even though during the mechanical alloying technique Y_2O_3 powder was included. The fine oxides particles are densely distributed inside the fcc solid solution and the B2 phase. Grain boundaries and phase boundaries are

decorated with the oxide particles, as shown in **Fig. 4.8**. It is beneficial to the grain and phase stability at elevated temperature, because the grain coarsening and the phase boundary migration can be effectively hampered by the pinning effects of oxide particles [53-55].

Concerning the oxide particles formation, the MA processing induces dissociation of Y_2O_3 particles, then yttrium, hafnium and oxygen atoms combine together and precipitate as fine oxide particles during SPS sintering [23]. Under that condition, the unique core-shell structure was formed, which is consisted of $Y_2Hf_7O_{17}$ in the core, and $Y_2Hf_2O_7$ at the periphery, suggesting that a coalescence of hafnium atoms is a key phenomenon accompanied with the initial nucleation stage of the oxide particles, because the core region contains higher Hf/Co atoms ratio.

From the 3D-AP results of the fcc matrix in the 5 wt% Al (**Fig. 4.9**) and the B2 phase of the 10 wt% Al (**Fig. 4.10**), Y-Hf oxide particles have been observed in both the fcc matrix and in the B2 phase, but the particles size in the B2 phase is much larger than that in the fcc matrix. The B2 phase is known as a bcc type of CoAl intermetallic compound [56, 57]. Following measured composition of the B2 phase shown in **Fig. 4.7**, the B2 phase produced in Co-Cr-Al ODS superalloys has smaller Al-concentration than atomic ratio of Al/(Co+Cr) = 1: thus, Al-sites are replaced with either Co-atoms or Cr-atoms[58]. Nakamura et al. pointed out that a deviation from the stoichiometric composition towards Al-depleted side accelerates the diffusion of Co-atoms [59]. Coarsening of the oxide particles in the B2 phase could be associated with the enhanced diffusion of Y-atoms and Hf-atoms in the Al-depleted phase.

A coarse size of Y-Hf oxide particle is eventually seen in the fcc matrix. An example is shown in **Fig. 4.9(c)**, for which the formation process is considered to be dominated by following two aspects. This coarse Y-Hf oxide particle is adjacent to a large Al_2O_3 particle, suggesting that the Y-Hf oxide particle was precipitated on the interface of the Al_2O_3 particle, and could be easily coarsened by rapid diffusion of yttrium and hafnium atoms through the Al_2O_3 particle/matrix interface. Another possible aspect is associated with the crystal structure of Y-Hf oxide particle. This Y-Hf oxide particle can correspond to $Y_2Hf_7O_{17}$ type of particles, as it is suggested by

the measurement of atomic concentration shown in **Fig. 4.9(c)**. Zhang et al. reported that oxide particles size increases with increasing Hf content by the formation of $Y_2Hf_7O_{17}$ type [23]. The size of Al_2O_3 particle is also smaller in the fcc matrix than in the B2 phase, as compared with **Fig. 4.9** and **Fig. 4.10**. This could be partly ascribed to the limited diffusion of aluminum atom in the fcc matrix. In addition, as shown in **Fig. 4.9(d)**, the Al_2O_3 particle is covered with segregated yttrium and hafnium elements, which is considered to effectively restrict the coarsening of Al_2O_3 particles by the solute drag-like effect [26]. Besides, due to low diffusion coefficient and solubility in the cobalt fcc matrix, the coalescence of Hf occurs more easily in the 5 AlCrY than the 10Al since the high fcc volume fraction, which leads to the formation of larger oxides rich in Hf observed in **Fig. 4.8 (a)**. Based on the report [23] that higher Hf content would cause the increase in the larger oxides rich in Hf since the coalescence of Hf, the alloy with low Hf addition (1.2 wt%) has been fabricated, in which less white coarse particles can be detected with SEM, shown in **Fig. 4.11**.

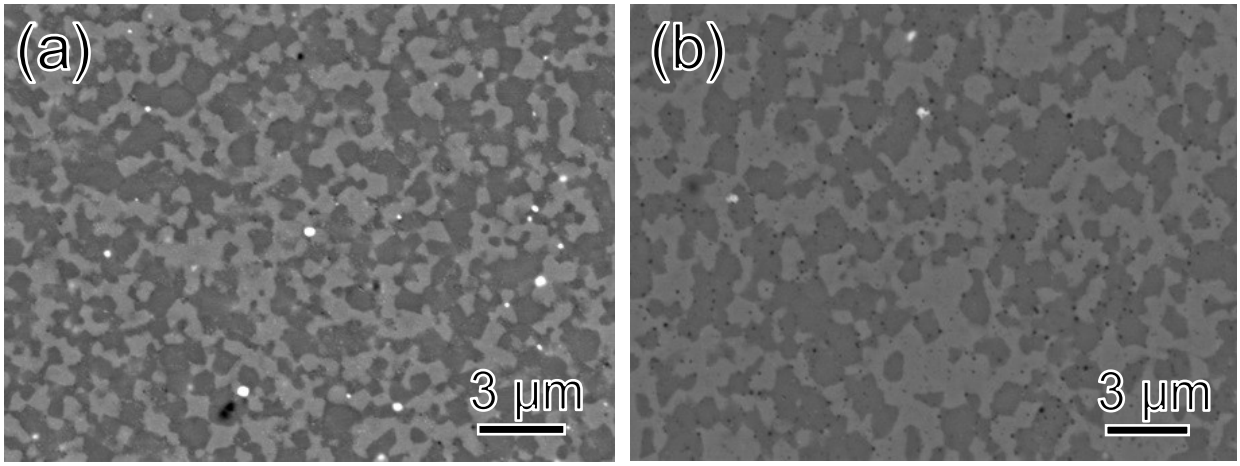

Fig. 4.11 SEM images obtained for 10 AlCrY sample with 2.4wt% Hf (a) and 1.2wt% Hf (b).

It is worth noting that another fcc phase with coarse grain was found to exist, in which few oxide particles are dispersed. A formation of the coarse grains with few oxide particles is likely to be associated with the melting. **Fig. 4.12** shows the pseudo-binary phase diagram computed with Pandat software, where the horizontal

axis denotes the aluminum concentration along 80Co-20Cr cross-section. The phase diagram indicates an incipient melting at 1200 ºC, which is the highest temperature in the process of fabrication, when aluminum content can reach about 30 wt.%.

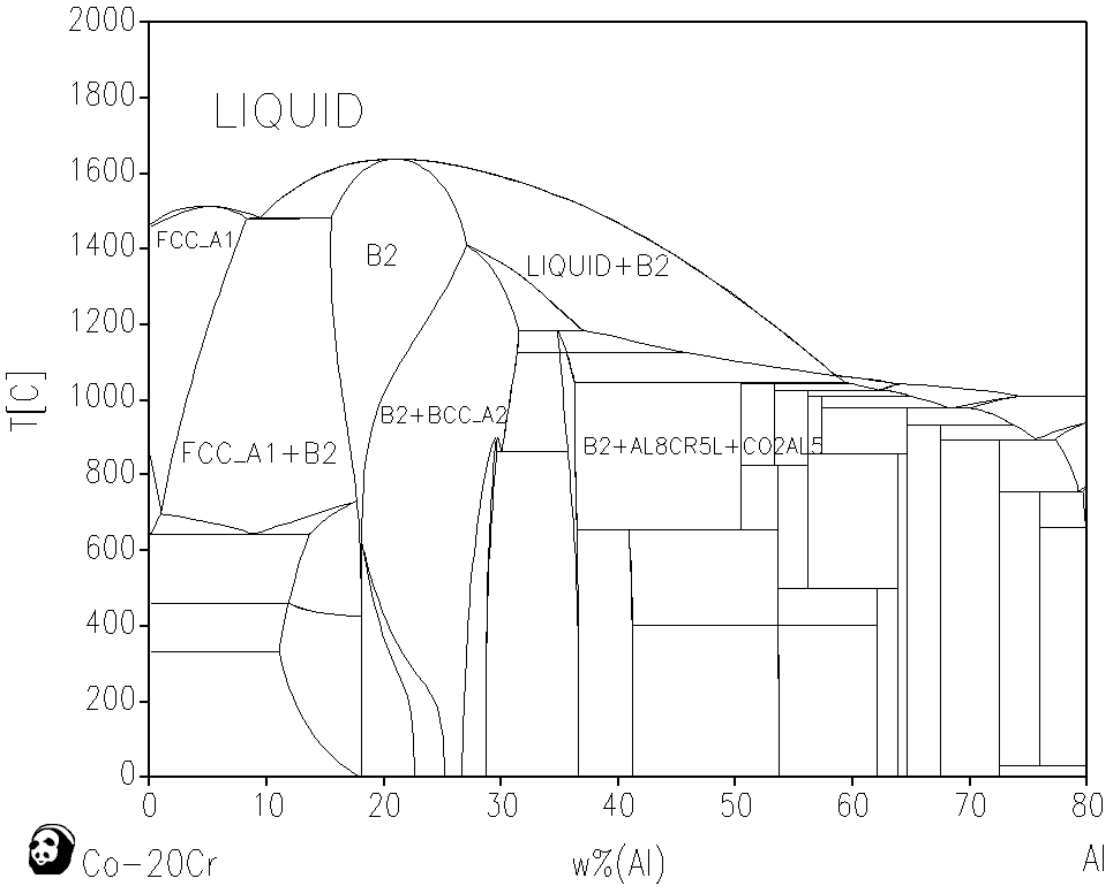

Fig. 4.12 Pseudo-binary phase diagram computed with Pandat software; horizontal axis shows aluminum concentration along Co-20Cr (wt%) cross-section.

However, the EPMA elemental maps show homogeneous aluminum distribution in the MA powder (**Fig. 4.1**). Even after final annealing, aluminum concentration is less than 20 wt% in each phase, as shown in **Fig. 4.7**. These results deny the supposition that the formation of the coarse fcc grains with few oxide particles is ascribed to the incipient melting caused by inhomogeneous distribution of Al content in the usual fabrication process. **Fig. 4.13** shows SEM micrograph of the 5AlCrY sample after SPS process at 1100 ºC sintered for just 5 minutes. The coarse smooth

region marked by 3 is obviously seen around pores even after 5 minutes of sintering. The residual pores still exist between original particles due to the insufficient time of SPS sintering equal to 5 minutes.

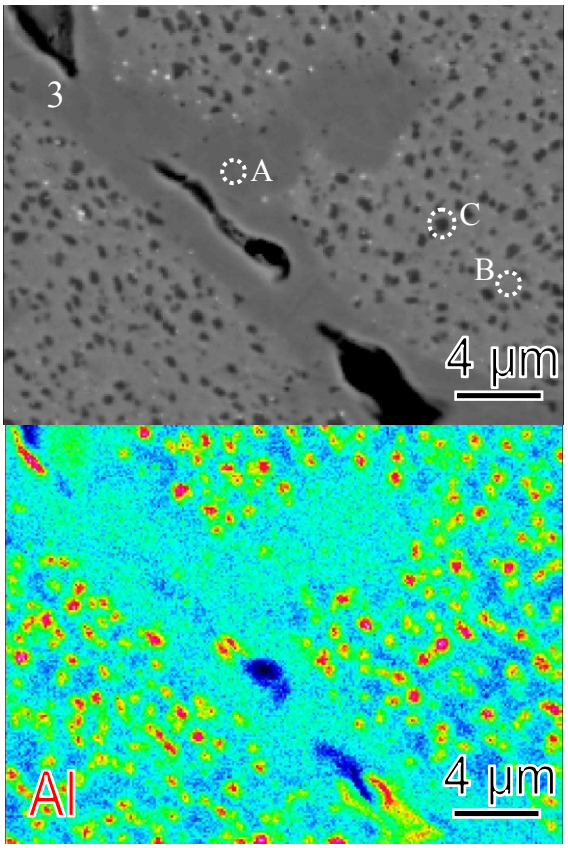

Fig. 4.13 SEM micrographs and corresponding EPMA maps obtained for 5AlCrY sample with SPS 5 minute.

Table 4.2 lists the results of EDS analyses, indicating that aluminum concentration in the coarse fcc phase is 2.6 wt. %, and it is the same as in the fcc matrix. Focusing on temperature change during SPS sintering, it is seen from the computed pseudo-binary phase diagram shown in **Fig. 4.12**, that the eutectic reaction can take place at around 1480 ºC. Thus, one possibility responsible for the incipient melting and the formation of the coarse fcc phase may be associated with a local overheating induced by discharged spark at the interface between particles in the initial stage of insufficient SPS sintering.

Table 4.2 EDS analysis of the different phases in 5 AlCrY after SPS for 5 minute (wt.%)

	Co	Cr	Al	Y	Hf
A (Coarse FCC)	72.151	20.928	2.635	0.134	0
B (Matrix FCC)	69.047	20.594	2.471	0.937	1.508
C (B2)	65.712	17.283	6.105	1.072	1.218

During the SPS process, a local high temperature state of over 1000 ^{o}C momentarily occurs in the microgaps between the powder particles, resulting in the vaporization and the melting of the surfaces of the powder particles [52]. It's difficult to measure the actual temperature between particle microgaps, and this specific local high temperature model during SPS process also can't be simulated by other sintering process. In order to prove the conjecture that the coarsened phase was induced by the incipient melting in SPS, I tried to consolidate the powders with Hot Press, which is much more uniform heating. However, the coarse phase was still observed in the 10Al consolidated with Hot Press, as shown in **Fig. 4.14**, in which few Y-Hf oxides distribution were proved through the EPMA elemental mapping (**Fig. 4.15**). Therefore, the formation of this coarse fcc phase with less dispersoids seems not to be determined by the consolidation process. Based on the reports [60], a bimodal distribution of grains was found in the ODS-304 austenitic steel, in which the fine Y-Ti-O were dispersed in the small grains but almost no dispersoids inside the large grains. Similar bimodal distribution of grains was also observed in reduced activation ferritic/martensitic steels [61] and 12-14% Cr ODS ferritic steels [62, 63]. Boulnat et al. [64, 65] claimed that the bimodal grain size distribution in the Fe-14Cr-1W-0.3Ti-Y2O3 steels prepared by MA and SPS arises from an initial, heterogeneous spatial distribution of stored energy from MA, leading to inhomogeneous recrystallization. Thus, the coarse phase in the Co-based ODS superalloys could be supposed to associate with the MA process, and further experiments should be conducted to prove this hypothesis.

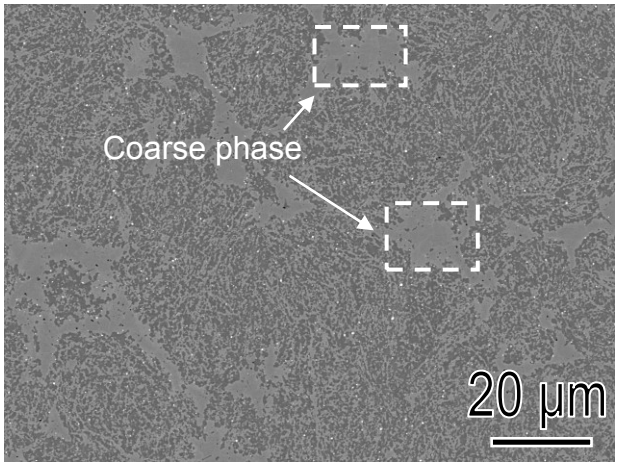

Fig 4.14 SEM images obtained from 10AlCrY sample consolidated with Hot Press.

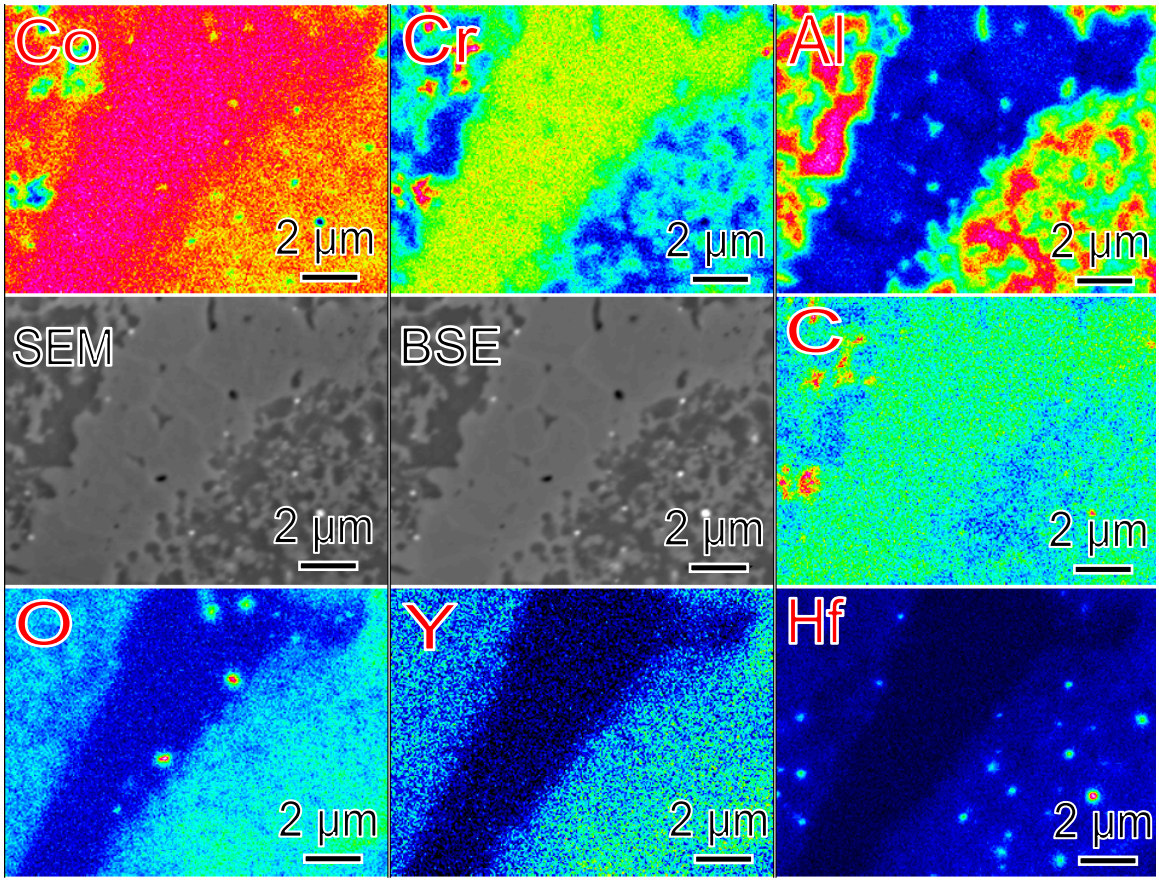

Fig. 4.15 SEM / BSE micrographs and corresponding EPMA elemental maps obtained from 10AlCrY sample consolidated with Hot Press.

4.4 Summary

Microstructures of the fabricated Co-20Cr-(5,10)Al Co-based ODS superalloys were characterized, and following results are obtained:

(1) The 5 wt% Al and the 10 wt% Co-base superalloys contain basically two phases: a Co-based solid solution with fcc structure, and a B2 phase enriched with Aluminum. The composition and volume fraction of the fcc phase and the B2 phase in both superalloys are almost consistent with a Co-Cr-Al ternary phase diagram computed with Pandat software. In addition, a coarse fcc phase with less content of oxide particles was characterized. The formation of this phase shows no relationship with the consolidation process of SPS or Hot Press, which was considered to attribute to the inhomogeneous distribution from MA process.

(2) Fine oxides particles are densely distributed inside the fcc solid solution and in the B2 phase. The size of Y-Hf oxide and Al_2O_3 particles in the fcc solid solution is much smaller than in the B2 phase. Grain boundaries and phase boundaries are decorated with the oxide particles, which is beneficial to grain and phase stability at elevated temperature. One unique core-shell structure was identified in the oxide particles which consisted of $Y_2Hf_7O_{17}$ type in the core and $Y_2Hf_2O_7$ type at the periphery.

Chapter 5 Oxidation behavior

5.1 Experimental details

High-temperature oxidation behavior of the Co-20Cr-(5, 10)Al-2.4Hf-1.5Y_2O_3 (wt.%) ODS superalloys was investigated by the isothermal oxidation test at 900 ^oC and 1000 ^oC in air, which effectively reflected the influence of Al content in the Co-based ODS system. Besides, in order to evaluate the effect of Cr and Y_2O_3 on oxidation behavior at 900 ºC and 1000 ºC, other two compositions of Co-10Al-2.4Hf-1.5Y_2O_3 (wt. %) and Co-20Cr-10Al-2.4Hf (wt. %) were prepared and investigated. The nominal chemical compositions and corresponding abbreviations are listed in **Table 5.1**.

The samples for oxidation test were cut into a cuboidal shape, and all the surfaces of investigated samples were wet ground using SiC paper up to 2400-grit, and then polished with 3 μm and 1 μm-diamond paste. After confirming that no residual scratches can be observed in the surfaces by an optical microscopy, the samples were ultrasonically cleaned in alcohol, and dried in hot air. Isothermal oxidation test at 900 ºC and 1000 ºC was carried out inside a muffle furnace in air. In order to determine the oxidation kinetics, the oxidation weight gains in different exposure durations (1, 4, 16, 25, 49, 100, 225 h) were measured at room temperature via a Sartorius precision electronic balance with a resolution of 1 μg.

The crystalline structures of oxide layers were detected using X-ray diffraction (XRD, Philips X' Pert PRO), and the 3 º incident angle has been adopted to emphasize the semaphore of thin oxide scales. The surface morphologies of oxide scales were investigated by scanning electron microscope (SEM, Carl Zeiss Cross Beam 1540 EsB), also the fractured surface observation was carried out by the SEM. The polished cross sections of oxidized samples were analyzed by the electron probe micro-analyzer (EPMA, JEOL JXA-8530F), in which the elemental mapping and quantitative point analysis by WDS were carried out, besides, the distribution of trace element (Y and Hf) inside oxide scales has been investigated with high magnification EPMA elemental mapping. The distribution of nano-sized oxide particles in oxide scales was analyzed using transmission electron microscopy (TEM, JEM-2010 and

FEI Titan3 G2 60-300), in which the cross-sections in a thickness near 100 nm were prepared by Focused Ion Beam Milling and FE-SEM Imaging (FIB-SEM, JEOL JIB-4600F/HKD).

Table 5.1 Nominal compositions of the investigated alloys and utilized abbreviations.

Alloys	Elements, wt%				
	Co	Cr	Al	Hf	Y_2O_3
5AlCrY	Bal.	20	5	2.4	1.5
10AlCrY	Bal.	20	10	2.4	1.5
10AlY	Bal.	0	10	2.4	1.5
10AlCr	Bal.	20	10	2.4	0

5.2 Results

5.2.1 Effect of Al-content

Fig. 5.1 shows the weight gain per unit surface area as a function of exposure time for all the observed 5AlCrY and 10AlCrY Co-based superalloys at 900 ºC and 1000 ºC in 225 h. It can be confirmed that all the Co-based ODS superalloys are qualified to form stable oxide scales without scale spallation during isothermal oxidation at 900 °C and 1000 °C in air. In addition, in comparison with the 5AlCrY, the 10AlCrY alloys exhibit better oxidation resistance with smaller weight gains at 900 °C and 1000 °C. In respect of the 10AlCrY, it should be noted that the oxidation weight gain after 225 h of oxidation at 1000 °C is smaller than at 900 °C.

Fig. 5.2 shows the fitted parabolic curves drawn with mass gains as a function of square root of time, which reveal that the oxidation kinetics of the 5AlCrY and the 10AlCrY Co-based superallys follow a parabolic rate law during the oxidation process at both 900 °C and 1000 °C. However, a significant difference of the parabolic rate constants (k_p) for two temperatures has been found, i.e., the oxidation at 900 °C shows with an almost constant k_p value up to 225 h, whereas at 1000 °C the k_p has been obviously separated into two stages, which means that the oxidation at 1000 °C

for both the 5AlCrY and the 10AlCrY Co-based ODS specimens experienced an altered mechanism along with the exposed time. In accordance with the definition of corresponding parabolic rate constants (k_p):

$$k_p{}^{1/2} = \frac{\Delta W}{t^{1/2}} \quad (1)$$

where ΔW is measured weight change and t is corresponding exposure time, the k_p values at 900 °C and 1000 °C were calculated and presented in **Table 5.2**.

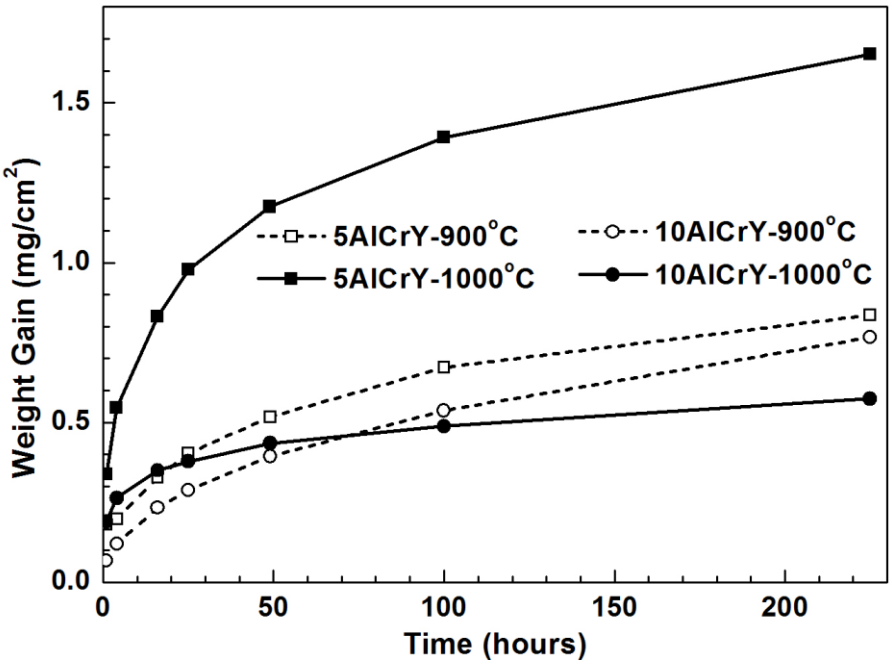

Fig. 5.1 Weight gain curves for the 5AlCrY and the 10AlCrY Co-based ODS superalloys oxidized at 900 ºC and 1000 ºC in air for 225 h.

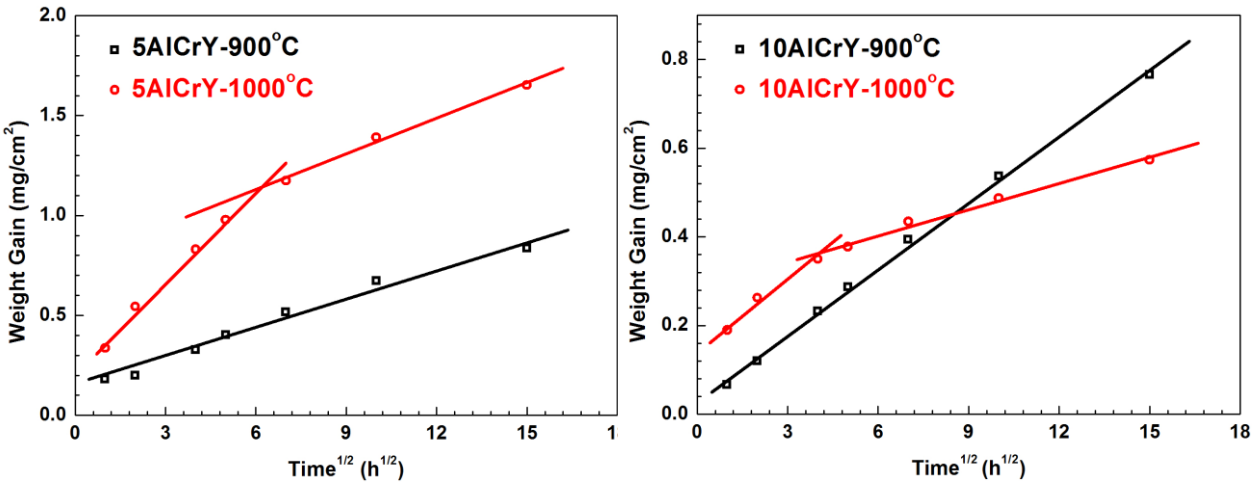

Fig. 5.2 The fitted parabolic curves for the 5AlCrY and the 10AlCrY Co-based ODS superalloys oxidized at 900 ºC and 1000 ºC in air for 225 h.

Table 5.2 Parabolic rate constants for the high-temperature oxidation of the 5AlCrY and the 10AlCrY Co-based ODS superalloys.

Superalloys	Parabolic rate constant, k_p ($g^2 \cdot cm^{-4} \cdot s^{-1}$)	
	900 ºC	1000 ºC
5AlCrY	6.9×10^{-13}	6.0×10^{-12} (~25 h)
		9.9×10^{-13} (25~225 h)
10AlCrY	6.5×10^{-13}	8.7×10^{-13} (~16 h)
		1.1×10^{-13} (16~225 h)

Fig. 5.3 shows the XRD patterns for the Co-based ODS superalloys oxidized at 900 °C and 1000 °C with the exposure time of 225 h, in which (a) and (b) represents the results of 5AlCrY and 10AlCrY, respectively. In addition to the characteristic peaks coming from matrix, the obvious diffraction peaks of oxide products were detected. In the case of 5AlCrY, the $CoCr_2O_3$ and Cr_2O_3 are dominated no matter at 900 °C or at 1000 °C, and several α-Al_2O_3 peaks could be found in the samples oxidized at 1000 °C. On the other hand, for the 10AlCrY samples, only the α-Al_2O_3 has been detected at both the 900 °C and 1000 °C, and some faint peaks of θ-Al_2O_3 have been demonstrated in the samples oxidized at 900 °C.

In order to obtain more information about the crystalline structure of alumina, a low incidence angle (3° incident angle) in XRD testing was conducted for the 10AlCrY alloys. It was proved through a number of short-term oxidation shown in **Fig. 5.4 (a)** and **(b)** that the change during the θ- to α-alumina transformation significantly depends on temperature and exposure time. In contrast with the co-existing of θ and α-alumina throughout the oxidation at 900 °C in 225 h, the α-alumina predominates with a transient period of the θ- and α-alumina co-existing in the initial stage at 1000 °C.

Fig. 5.5 shows the surface morphologies of the 10AlCrY samples oxidized at 900 °C and 1000 °C. In the initial stage of oxidation for 25 h at 900 °C, compared with the case at 1000 °C, a noticeable blade-like morphology appeared, and it was

clarified to be the intrinsic structure of metastable θ-alumina by many researches [66, 67]. With the extending of exposure time up to 225 h, a distinct θ-alumina was still detected as needles at 900 °C, whereas a stable α-alumina with equiaxed grains was observed at 1000 °C.

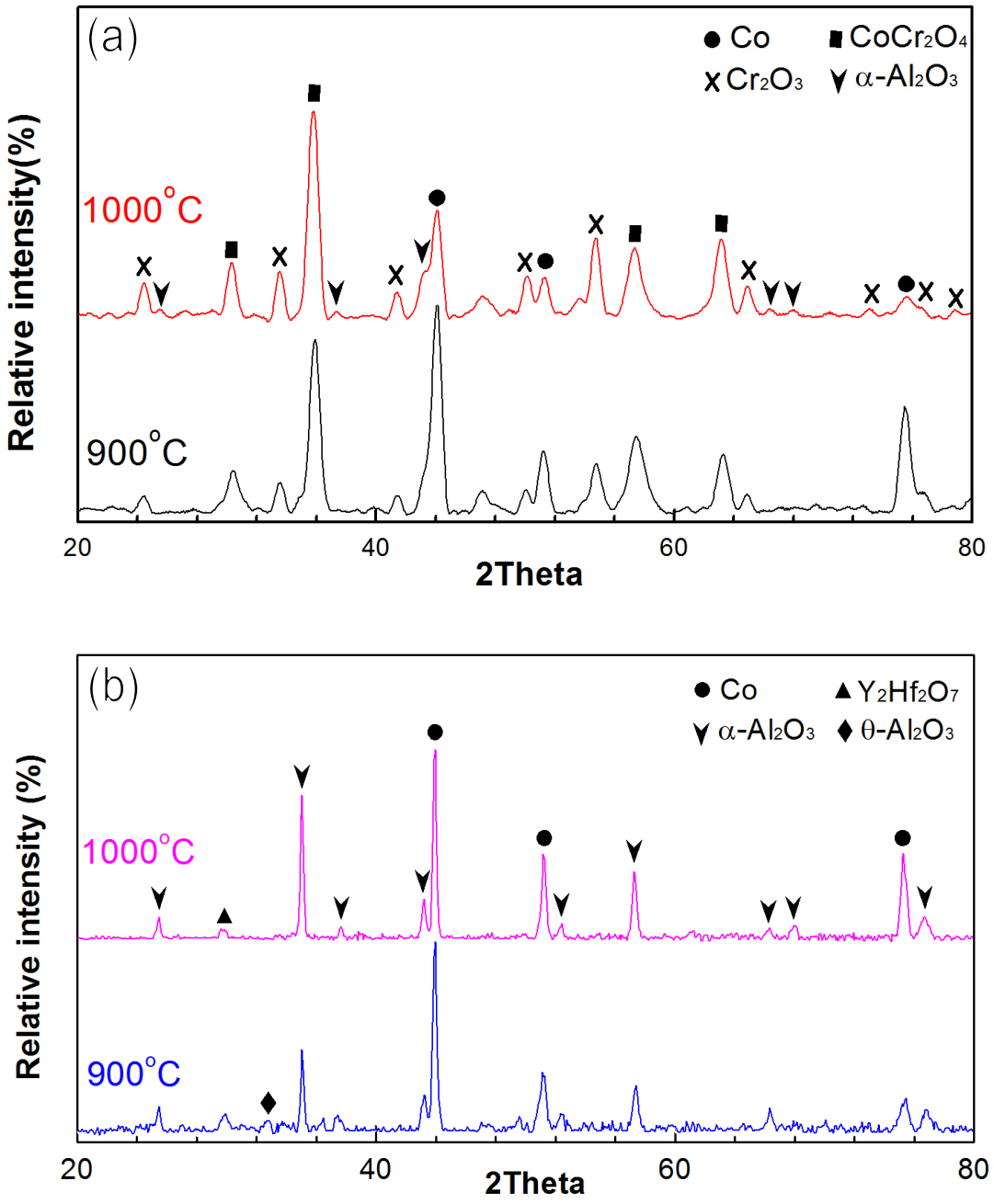

Fig. 5.3 XRD results for the 5AlCrY (a) and the 10AlCrY (b) Co-based ODS superalloys oxidized at 900 ºC and 1000 ºC in 225 h.

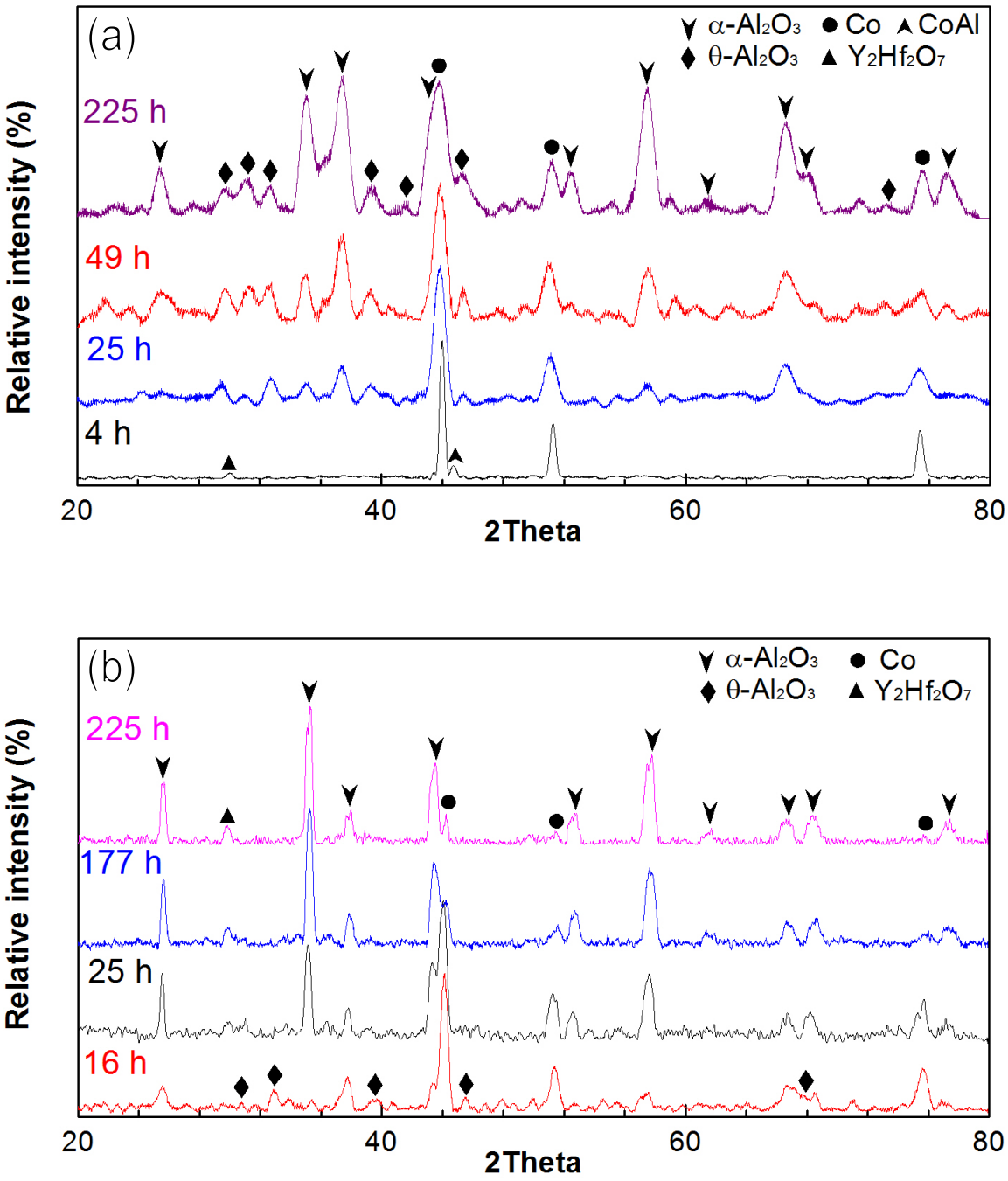

Fig. 5.4 XRD patterns in a number of short-term oxidation, (a) and (b) represents the results of the 10AlCrY alloys obtained at 900 ºC and 1000 ºC, respectively.

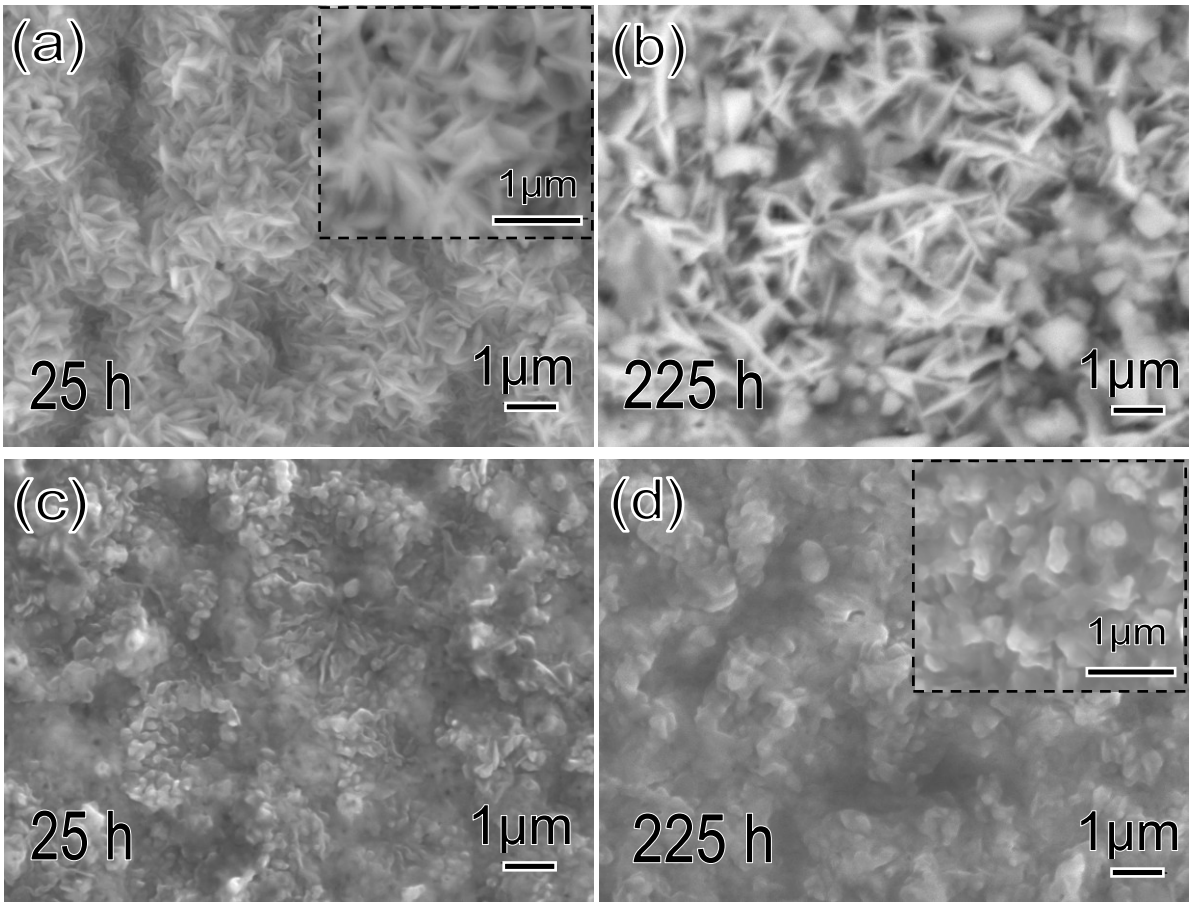

Fig. 5.5 Surface morphologies obtained from the 10AlCrY samples oxidized in 25 h and 225 h, (a) and (b) for 900 ºC as well as (c) and (d) for 1000 ºC.

The cross sections of samples oxidized at 900 °C and 1000 °C for 225 h were examined with the backscattered electron pattern (BSE), as shown in **Fig. 5.6**, in which (a)-(b) belong to the 5AlCrY samples as well as (c)-(d) belong to the 10AlCrY samples. **Fig. 5.6 (a)** shows the oxide scales at 900 °C for the 5Al, which is composed of a gray layer at surface and internal precipitates in the subsurface region with a dark contrast. With increasing temperature to 1000 °C, as shown in **Fig. 5.6 (b)**, the outer scale becomes porous with many visible voids, and the internal oxide precipitates become a continuous layer. In contrast, 10AlCrY contains only a single oxide scale generated at outer layer with a dark contrast in the BSE images. It is to be emphasized that the thickness of the single scale is significantly decreased through comparing **Fig. 5.6 (c)** and **(d)**, when the temperature increases from the 900 °C to the 1000 °C.

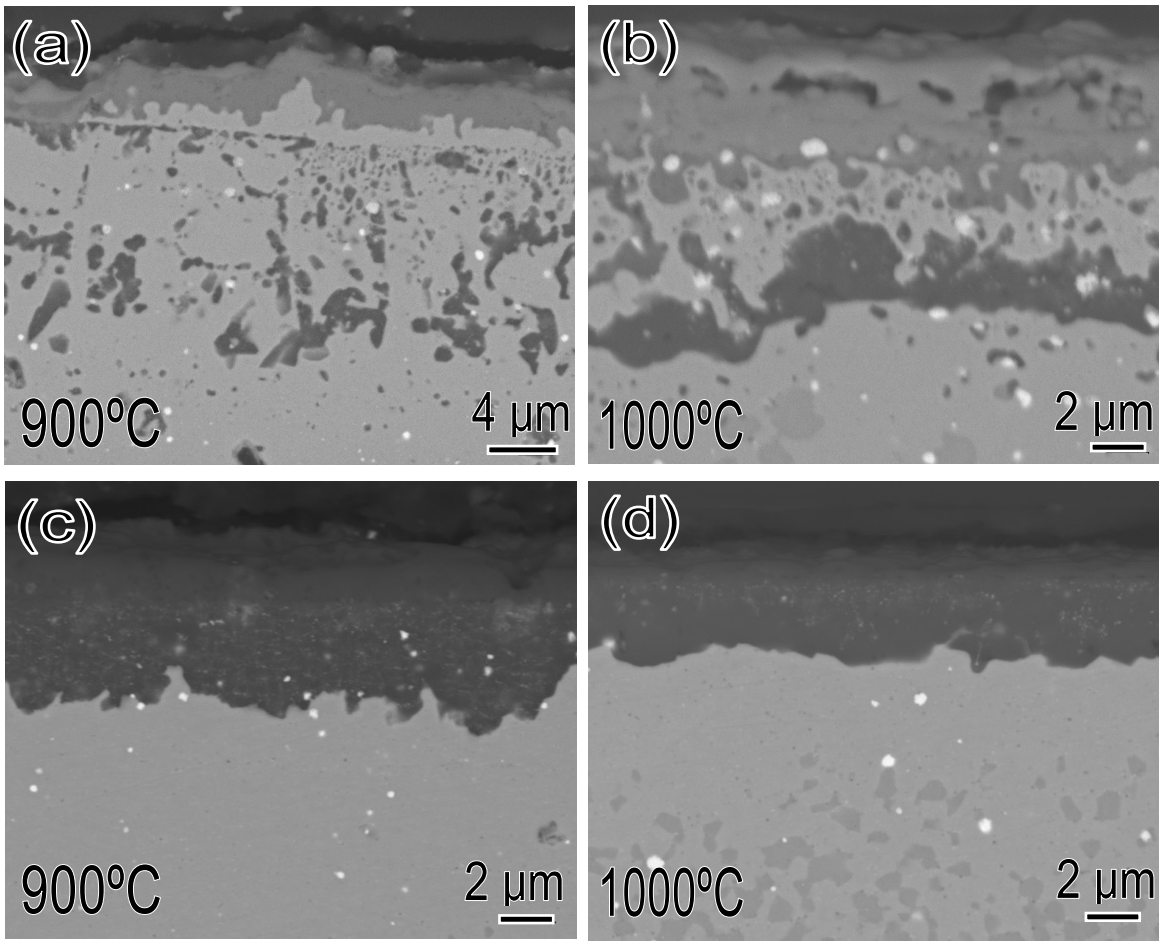

Fig. 5.6 Cross sections of the samples oxidized at 900 ºC and 1000 ºC in 225 h, (a) and (b) for the 5AlCrY samples as well as (c) and (d) for the 10AlCrY samples.

In order to further identify the distribution of elements in the oxide scale, the EPMA elemental mapping was carried out for the specimens oxidized at 900 °C and 1000 °C in 225 h, and the results of the 5AlCrY samples and the 10AlCrY samples are displayed in **Fig. 5.7 (a, b)** and **Fig. 5.8 (a, b)**, respectively.

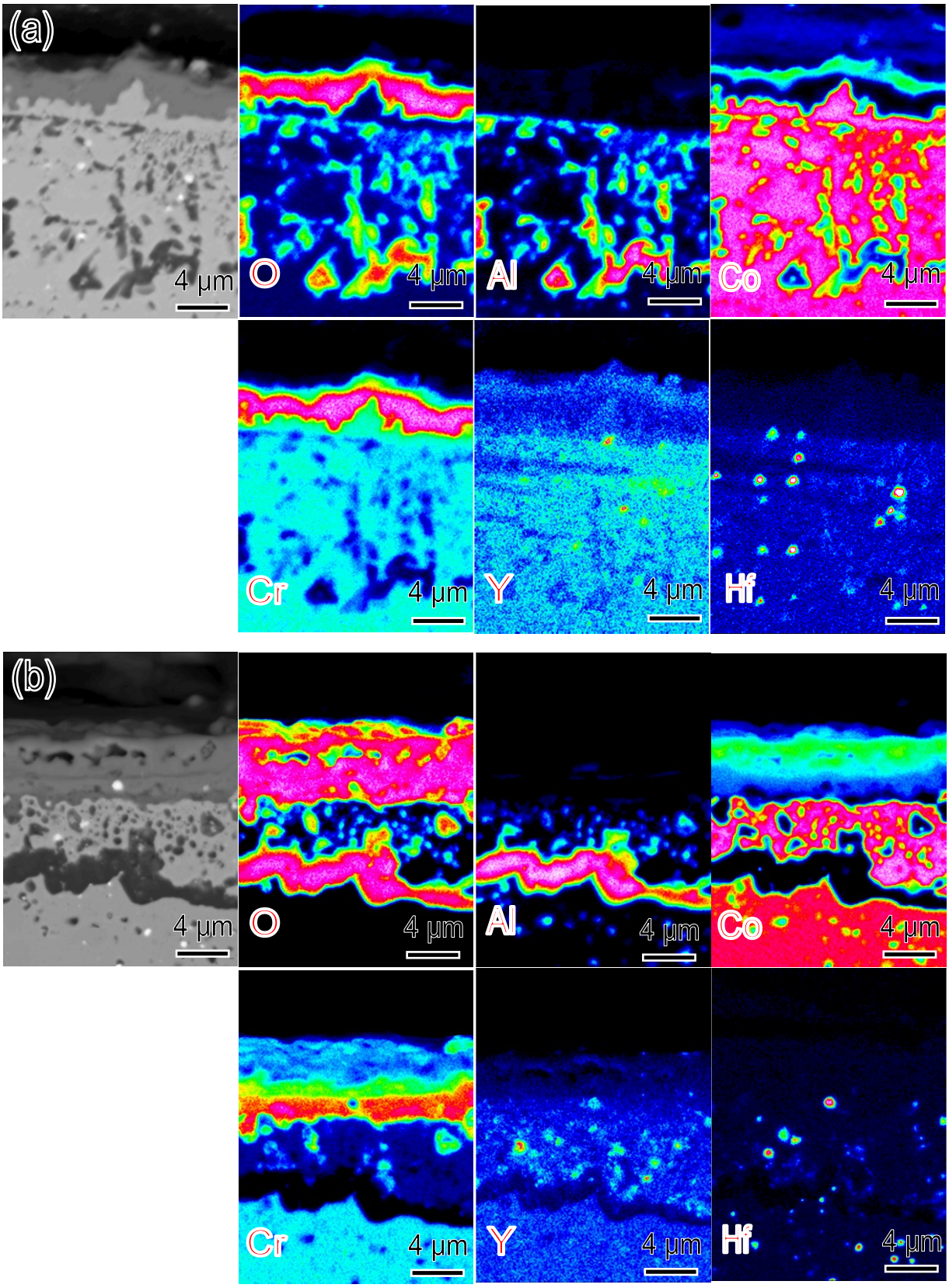

Fig. 5.7 EPMA elemental mappings obtained from the 5AlCrY samples oxidized in 225 h, (a) and (b) represents the results at 900 ºC and at 1000 ºC, respectively.

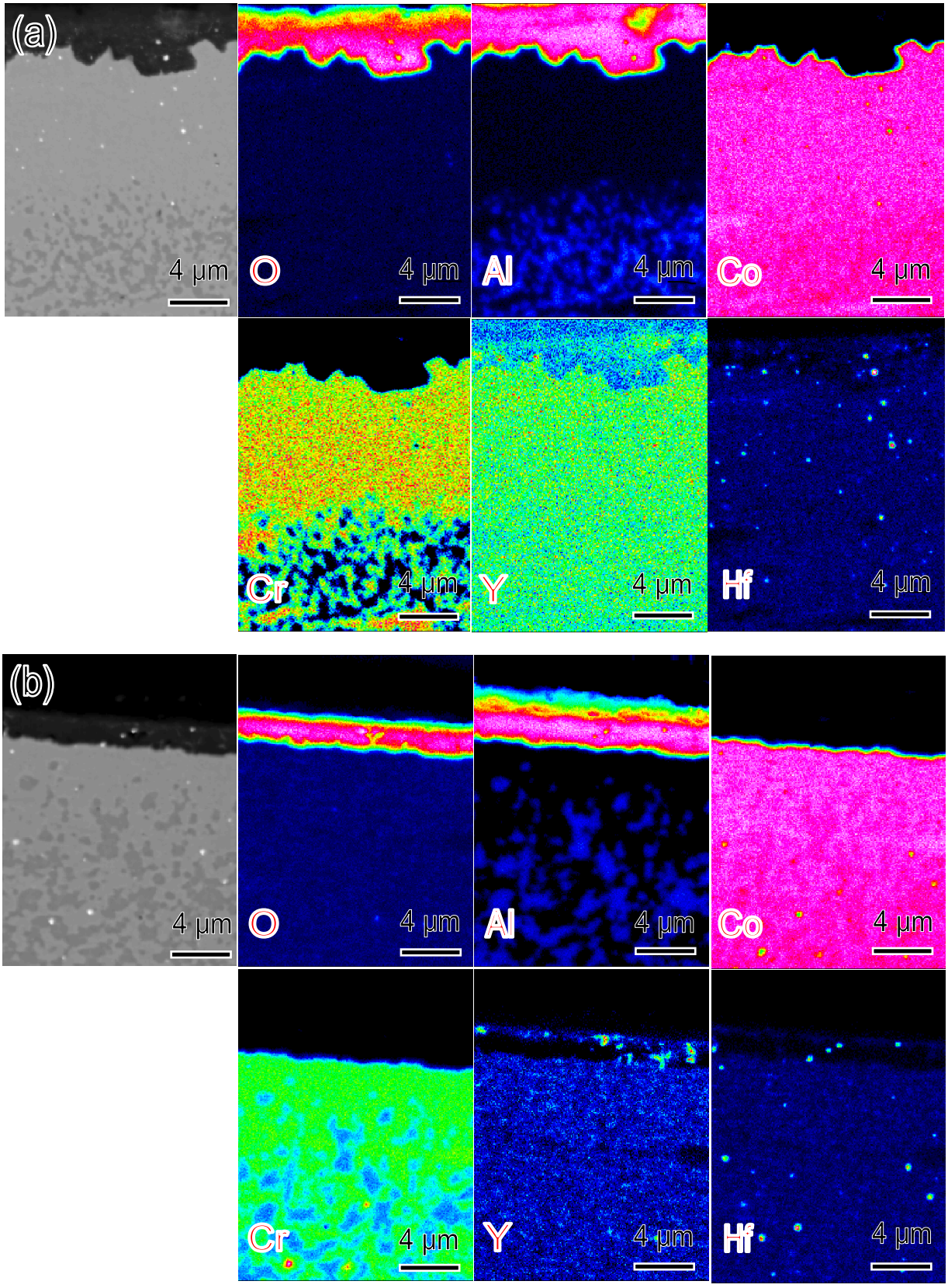

Fig. 5.8 EPMA elemental mappings obtained from the 10AlCr samples oxidized in 225 h, (a) and (b) represents the result at 900 ºC and 1000 ºC, respectively.

Based on the **Fig. 5.7 (a)** at 900 °C, the gray scale of the 5AlCrY is mainly composed of chromium and oxygen elements, and above this scale, a thin layer enriched cobalt, chromium and oxygen could be found. According to the XRD diffraction pattern in **Fig. 5.3 (a)**, those two scales were considered to be Cr_2O_3 and $CoCr_2O_4$, respectively. However, with increasing temperature to 1000 °C shown in **Fig. 5.7 (b),** the Cr_2O_3 scale becomes thinner and the $CoCr_2O_4$ region changes to be thicker. Besides, the internal oxides with dark contrast in 5AlCrY is consider to be Al_2O_3 due to being enriched both aluminum and oxygen elements, and Al_2O_3-scale has grown from the discontinuous alumina oxides at 900 °C to a continuous alumina scale at 1000 °C, which is quite consistent with the appearance of the obvious alumina diffraction peaks in the 5AlCrY oxidized at 1000 °C. On the other hand for the 10AlCrY, based on the enrichment of aluminum and oxygen elements at the outer layer, as shown in the **Fig. 5.8 (a, b)**, and the alumina diffraction peaks obtained from the XRD results in **Fig. 5.3 (b)**, the oxide scales of the 10AlCrY alloys at 900 °C and 1000 °C are defined as alumina.

In addition, secondary particles dispersing inside the alumina scales of 10AlCrY specimen could be detected with a white contrast in the BSE images, as shown in **Fig. 5.9 (a)** and **(b)**. These particles are considered to be Y-Hf oxides in accordance with the reference [68]. The distribution of those Y-Hf oxides is separated at 900 °C and 1000 °C, i.e. the particles distribute densely along the inner layer of alumina scale at 900 °C but along the outer part of inner layer at 1000 °C. According to the corresponding WDS point analysis, the concentration of Y and Hf is fit with the heterogeneous arrangement of the oxide particles inside alumina scales. Furthermore, the high magnification of EPMA observation focused on the alumina scales in the 10AlCrY samples was carried out, as shown in **Fig. 5.10**, in which the element distribution of yttrium and hafnium were detected to be consistent with the distribution of the secondary particles.

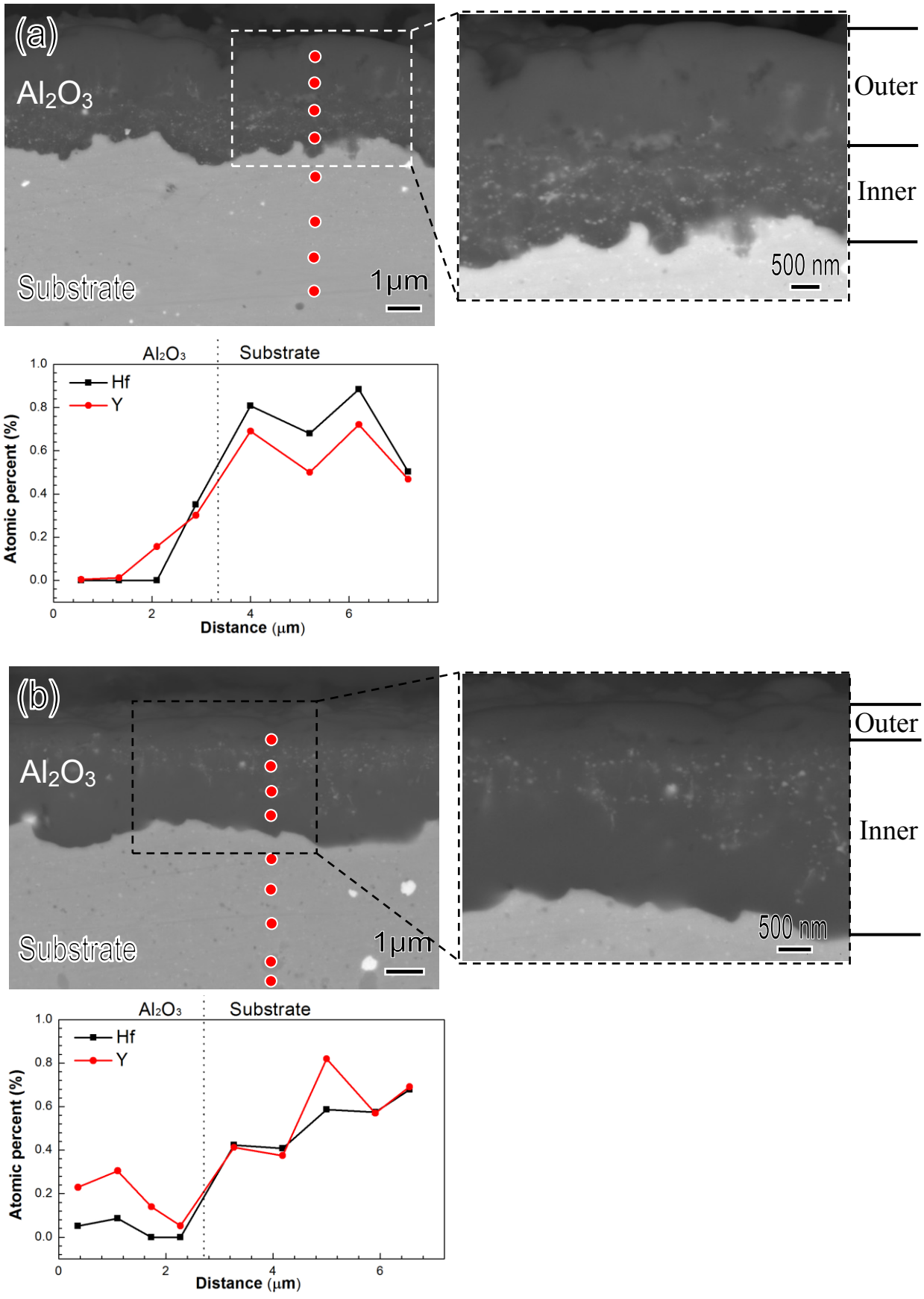

Fig. 5.9 The BSE images of cross-sections and corresponding EPMA WDS point analysis for the scales of the 10 AlCrY samples oxidized at 900 ºC in 100 h (a), and 1000 ºC in 225 h (b).

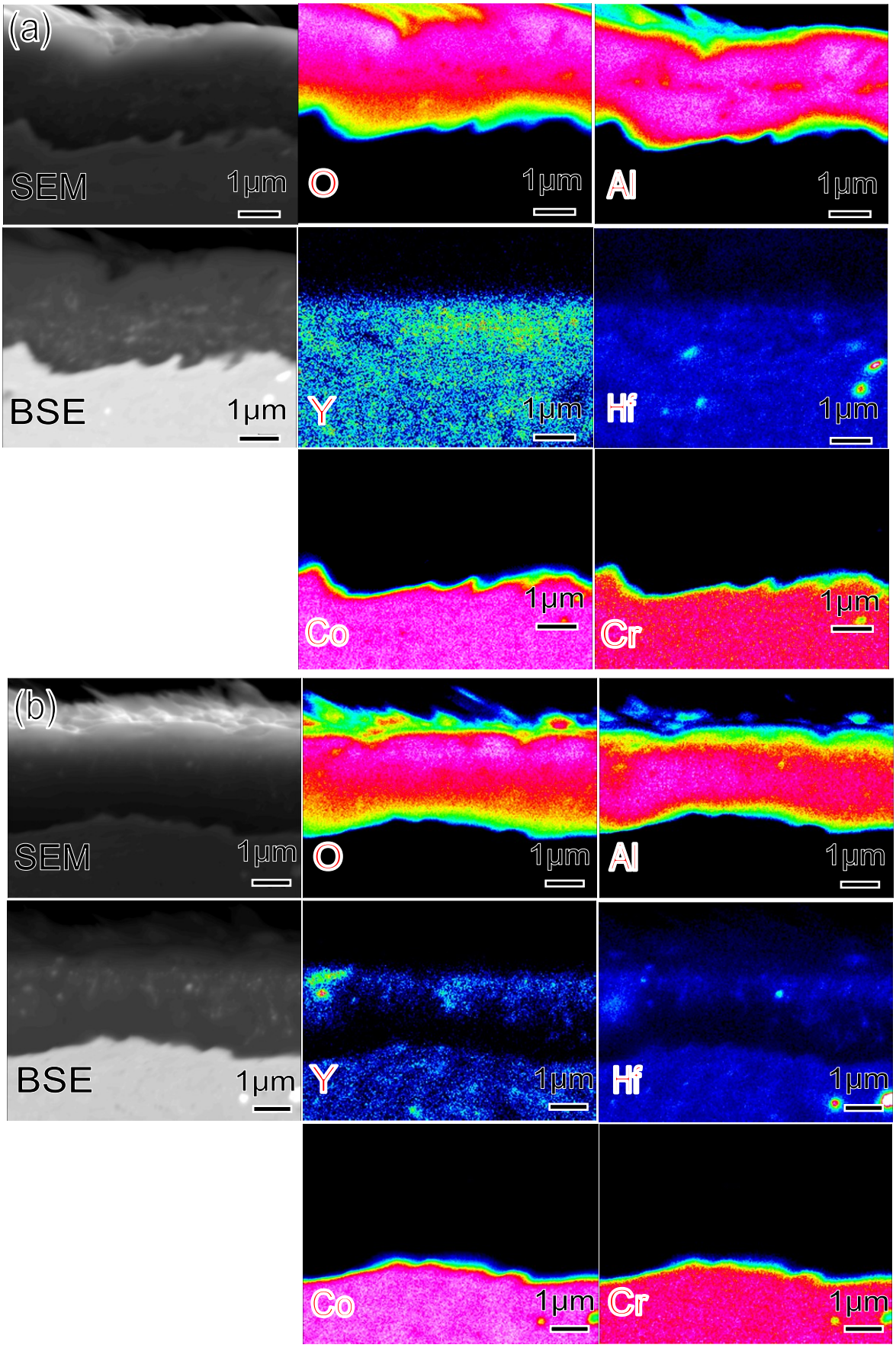

Fig. 5.10 Distribution of Y/Hf oxides in alumina scales of the 10AlCr samples. (a) shows the results at 900 ºC in 100 h, (b) is obtained at 1000 ºC in 225 h.

Fig. 5.11 (a) and **(b)** shows the fractured surfaces of 10AlCrY samples oxidized at 900 °C and 1000 °C, respectively. An obvious stratification of Y-Hf oxides happens in the alumina scale generated at 900 °C; in contrast with the dense particles close to substrate, outer layer possesses few secondary particles.

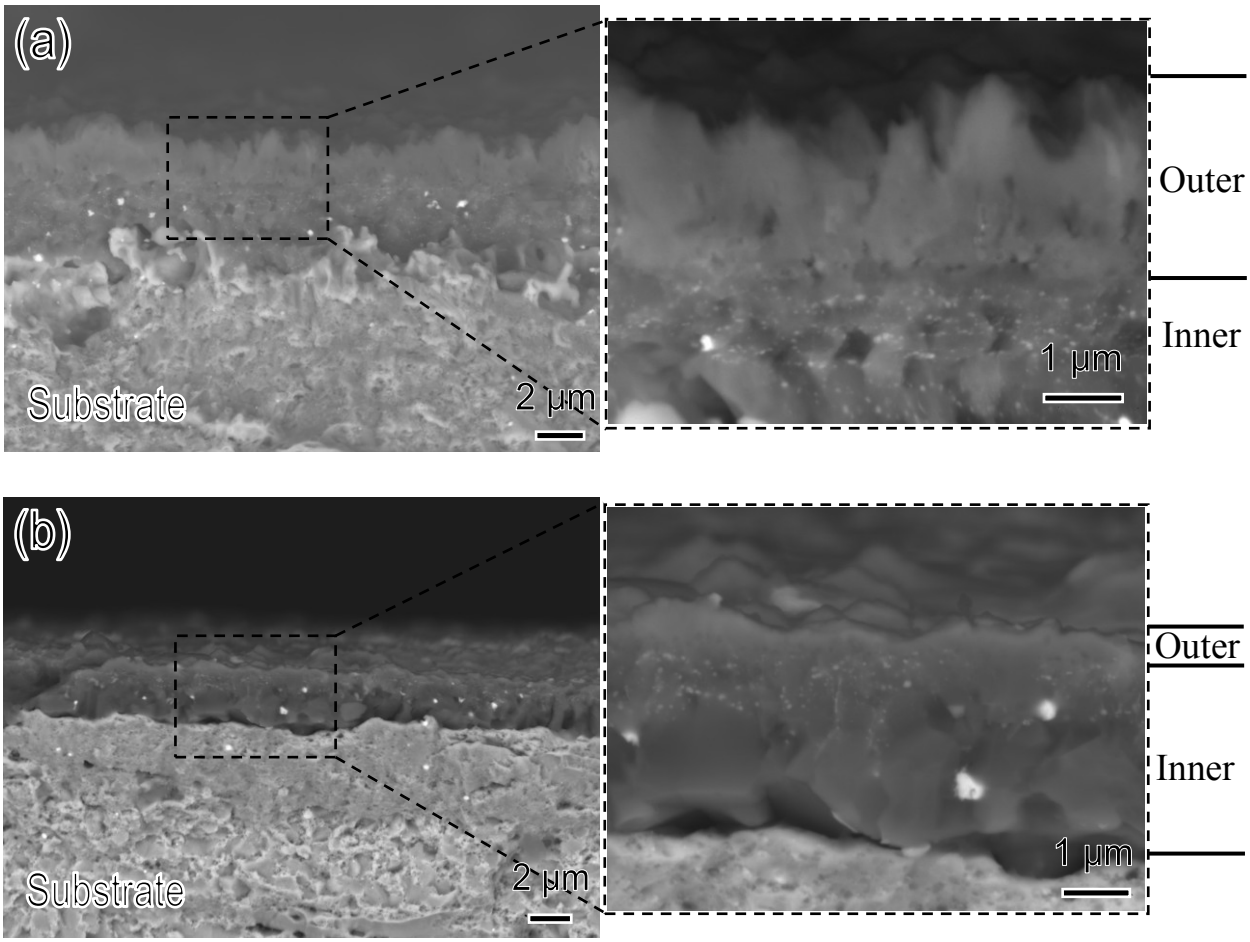

Fig. 5.11 BSE images obtained from the fractured surface of the 10AlCrY samples oxidized in 225h. (a) and (b) shows the result at 900 ºC and 1000 ºC,

Due to the exclusive blade-like structure located at the outer part of alumina scale, the outer layer with sparse oxide particles was confirmed to be θ-alumina. Besides, the inner area with dense particles was supposed to be mainly composed of α-alumina since its strong diffraction peaks detected in the XRD pattern. However, even though the alumina scale has been proved to be dominated with α-alumina at 1000 °C for 225 h and no blade-like structure could be found at the surface, a layered distribution of Y-Hf oxides particles still exists, i.e. outer part of the inner layer contains large

number of particles whereas an extremely thin outer layer and the inner region show free of particles. Moreover, the coarsened alumina grains could be observed at the inner area, as shown in the **Fig. 5.11 (b)**, where the obvious outline of grain boundaries could be observed.

TEM observation has been conducted for the alumina scales of 10AlCrY formed at 900 ^{o}C and 1000 ^{o}C. **Fig. 5.12** shows the results at 900 ^{o}C, in which dense dispersoids could be confirmed to distribute in the inner part, whilst few particles disperse in outer layer. Besides, a special tail structure of dispersoids was observed, as shown in **Fig. 5.13**, a spherical head region drags a long tail toward air. In the case of the sample oxidized at 1000 ^{o}C, particles are found in the outer layer but free in inner. The alumina grain size in the Y-Hf oxide free zone is much larger than that in the outer layer with Y-Hf oxides, as shown in the TEM black field image (BF) of **Fig. 5.14**. **Fig. 5.15** shows the HAADF-STEM images and the corresponding EDS maps for the oxide scale in the 10AlCrY alloy, in which (a) and (b) are obtained from the specimens oxidized in 225 h at 900 ^{o}C and 1000 ^{o}C, respectively. The Y-Hf oxides in the alumina formed at 1000 ^{o}C is much bigger than that at 900 ^{o}C. Therefore, it's evident that the Y-Hf dispersoids distribution in the alumina scale depends on the oxidation temperature. Namely, the Y-Hf particles disperse in the inner layer with a small size at 900 ^{o}C but prefer to the outer layer with a large size at 1000 ^{o}C. In respect of 900 ^{o}C, the HAADF-STEM images and corresponding elemental mapping (**Fig. 5.15 (a)**) proved that the dispersoids with long tails are Y-Hf oxides. In addition, an enrichment of Y and Hf in the alumina grain boundary was able to be confirmed.

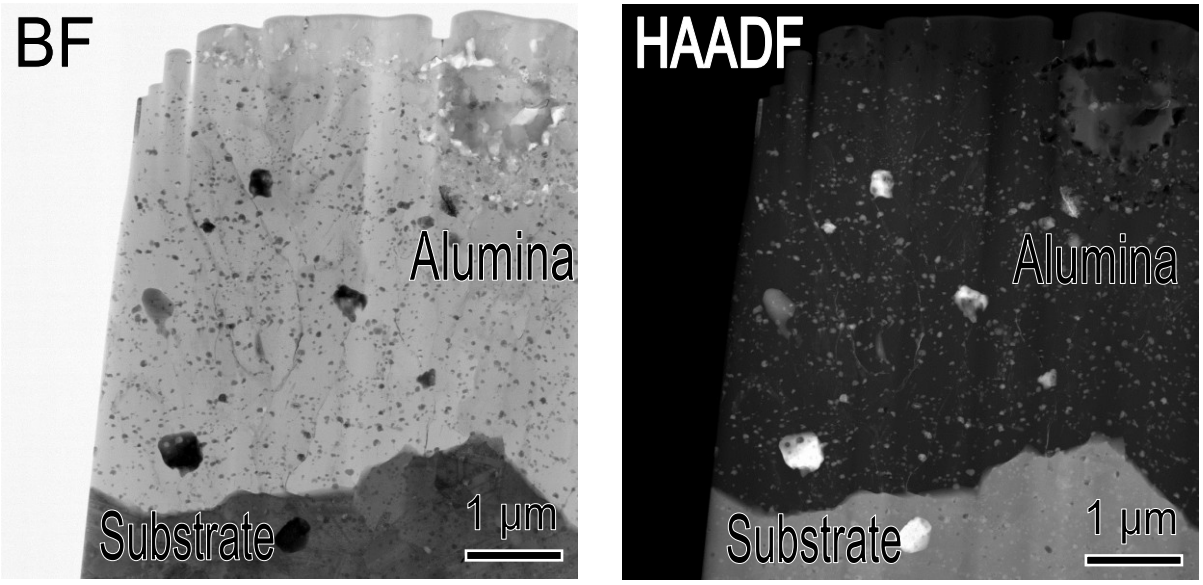

Fig. 5.12 HAADF-STEM images of 10AlCrY sample oxidized at 900 ^{o}C in 225 h. A large number of dispersoids at inner alumina layer but free at outer layer is exhibited.

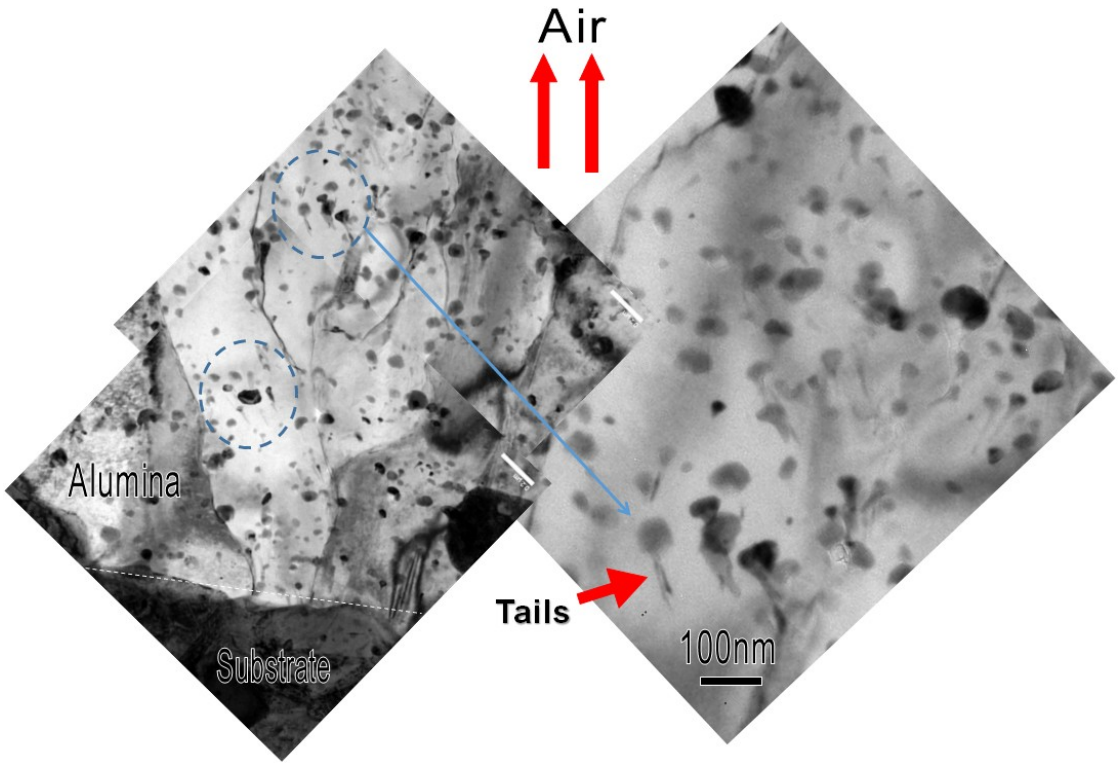

Fig. 5.13 TEM images of 10AlCrY sample oxidized at 900 ^{o}C in 225 h. A special structure of dispersoids with spherical head region and long tail could be observed.

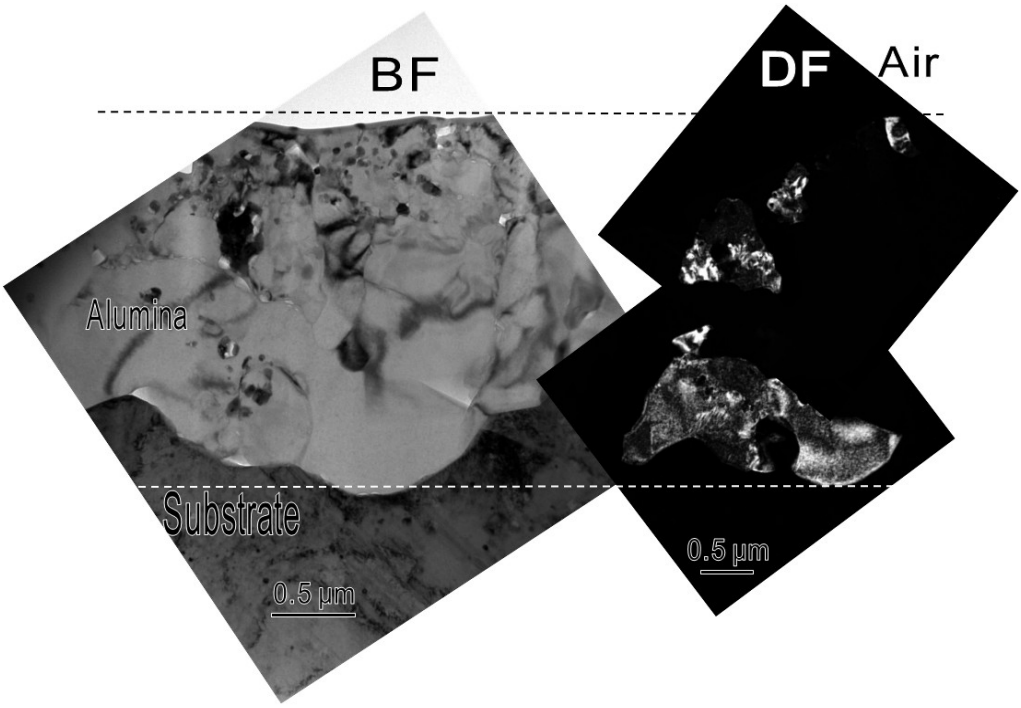

Fig. 5.14 TEM images of 10AlCrY sample oxidized at 1000 ^{o}C in 225 h. BF image shows amounts of dispersoids at outer layer but free at inner layer; DF image proved the grain size is smaller at outer layer but larger at inner.

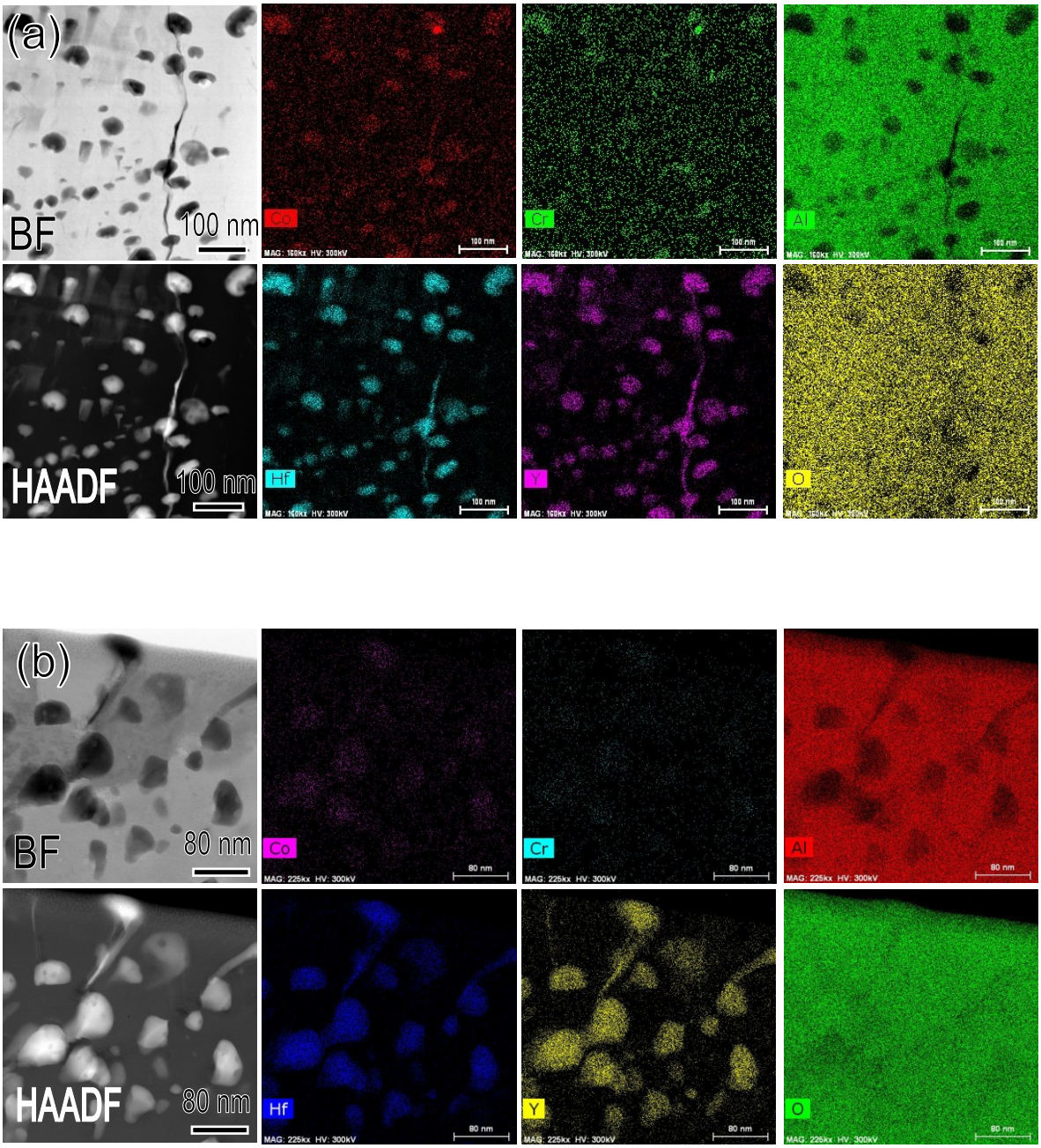

Fig. 5.15 HAADF-STEM images of nanoscale particles in the alumina scales of the 10AlCrY alloy and corresponding EDS elemental maps of Co, Cr, Al, Hf, Y and O, in which (a) and (b) are obtained at 900 ^{o}C and 1000 ^{o}C with 225 h, respectively.

5.2.2 Effect of Cr-addition

Fig. 5.16 shows the Co-Cr-Al phase diagram computed by the thermodynamic software Pandat [69], where the composition of Co-10Al (wt.%) and Co-20Cr-10Al (wt.%) has been marked with round and triangle symbol, respectively. The volume ratio of CoAl in B2 to Co solid solution in fcc is almost equal for Co-20Cr-10Al (wt.%), but less for Co-10Al (wt.%).

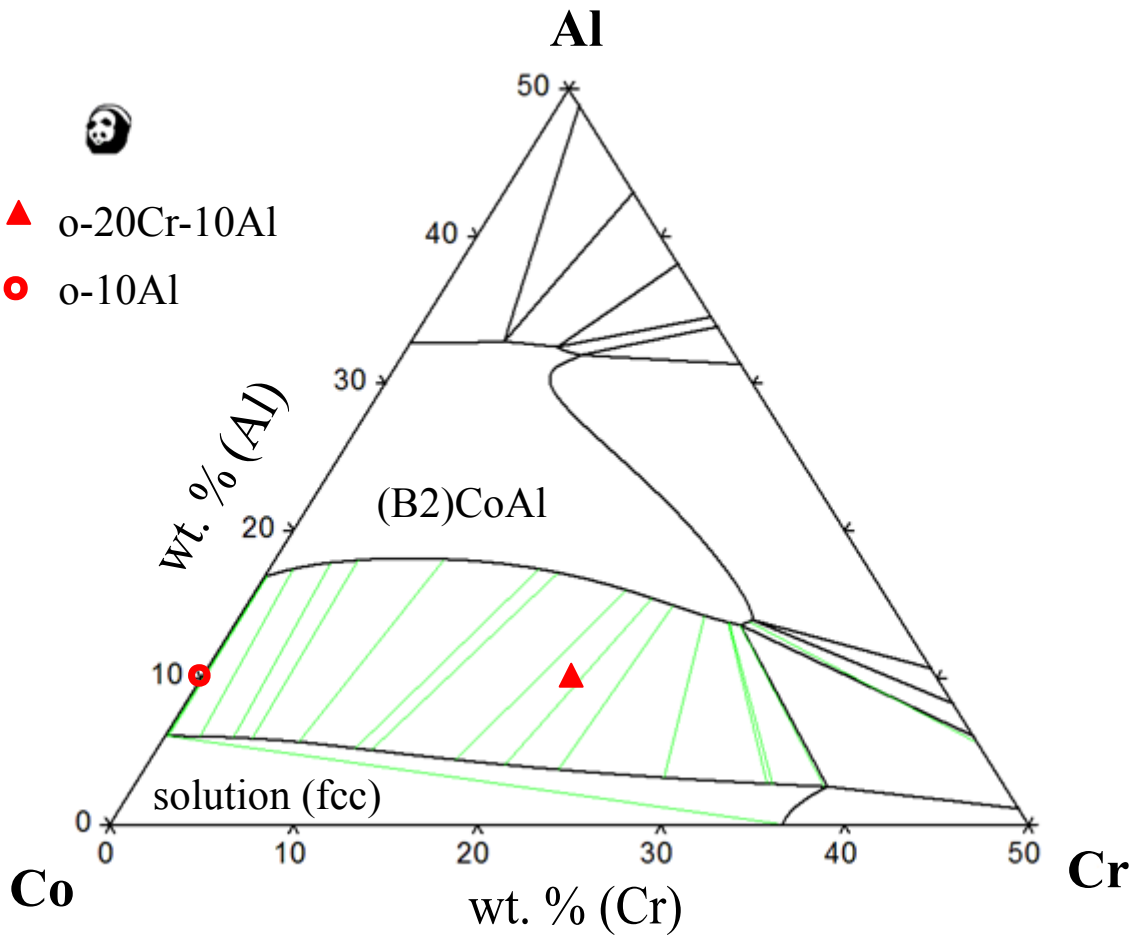

Fig. 5.16 The ternary Co-Cr-Al phase diagram calculated with Pandat software at 1100 ^{o}C.

Fig. 5.17 shows the SEM images of the fabricated 10AlCrY and 10AlY alloys, where the gray areas mean the fcc matrix and the dark regions represent B2 phase. The 10AlCrY alloys contains almost equivalent volume fraction in fcc phase and B2 phase, whereas the 10AlY possesses only 39% B2 phase. This result is consistent with the computed phase diagram shown in **Fig. 5.16**.

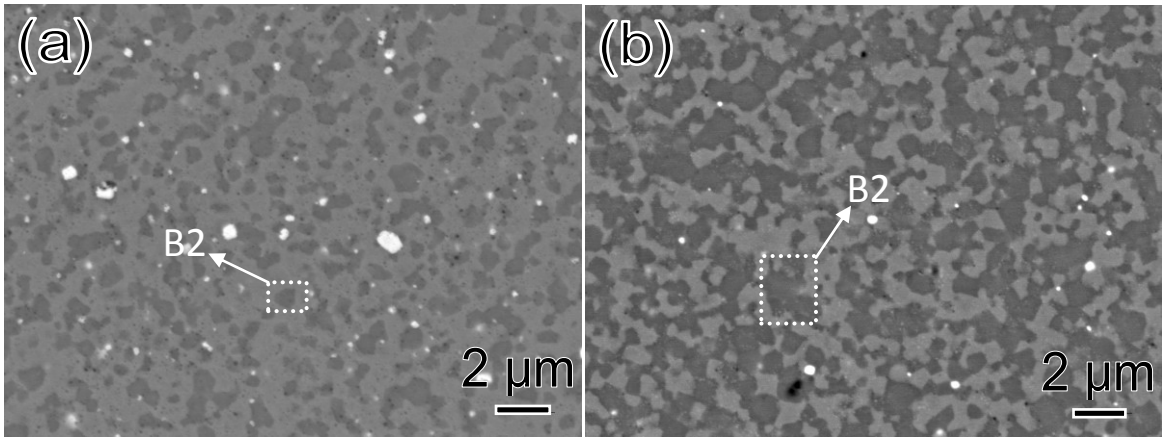

Fig. 5.17 SEM images obtained from the samples prior to oxidation, (a) and (b) represent the 10AlY samples and the 10AlCrY samples, respectively.

The observed weight changes for the 10AlY and 10AlCrY as a function of time during exposure at 900 ºC in air are shown in **Fig. 5.18**.

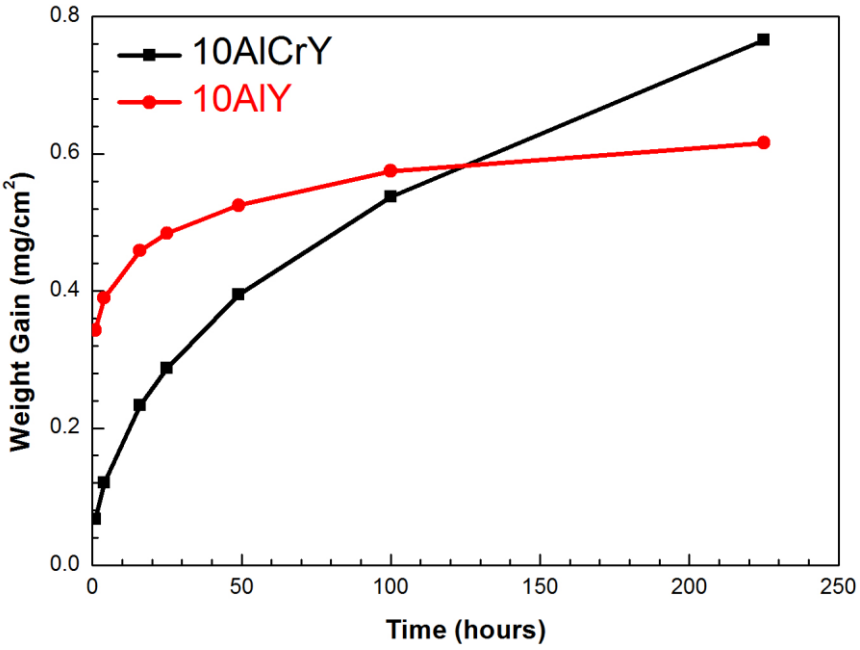

Fig. 5.18 Mass gain vs time curves of the 10AlY samples and the 10AlCrY samples at 900 ºC in air.

Both Co-based ODS superalloys with and without Cr addition have presented a low oxidized rate and a good spalling resistance up to 225 h. However, the oxidation kinetics has been changed significantly with Cr addition, i.e. in comparison with the 10AlY exhibiting an extremely rapid oxidation at initial stage and a quite slow

oxidation process at the subsequent duration, the 10AlCrY shows a relatively smooth oxidation behavior during exposure time. Firstly, the oxidation rate of 10AlY sample in the initial stage up to 1 h was much faster than the 10AlCrY sample, resulting in an evident mass gain of up to 0.34 mg/cm^2 in 1 h, which is more than half of the total mass gain in the entire experiment. Subsequently, the rate of mass gain in 10AlY alloy decreased much more quickly with time than the 10AlCrY alloy, such that the mass gain after 130 h was progressively less for this alloy, which leads to the appearance of an intersection between two thermogravimetric curves in **Fig. 5.18**.

Fig. 5.19 and **Fig. 5.20** show the scales crystalline structures and surface microstructures of two specimens oxidized at 900 ºC. Based on the characteristic peaks of CoO/$CoAl_2O_4$ and A_2O_3 in X-ray diffraction pattern, the attendance of CoO/$CoAl_2O_4$ in 10AlY oxide scales and A_2O_3 in the 10AlCrY oxide scales were determined, which is corresponding to the unique granule-like shape of CoO and typical blade-like structure of alumina in **Fig. 5.20 (a)** and **(b)**, respectively.

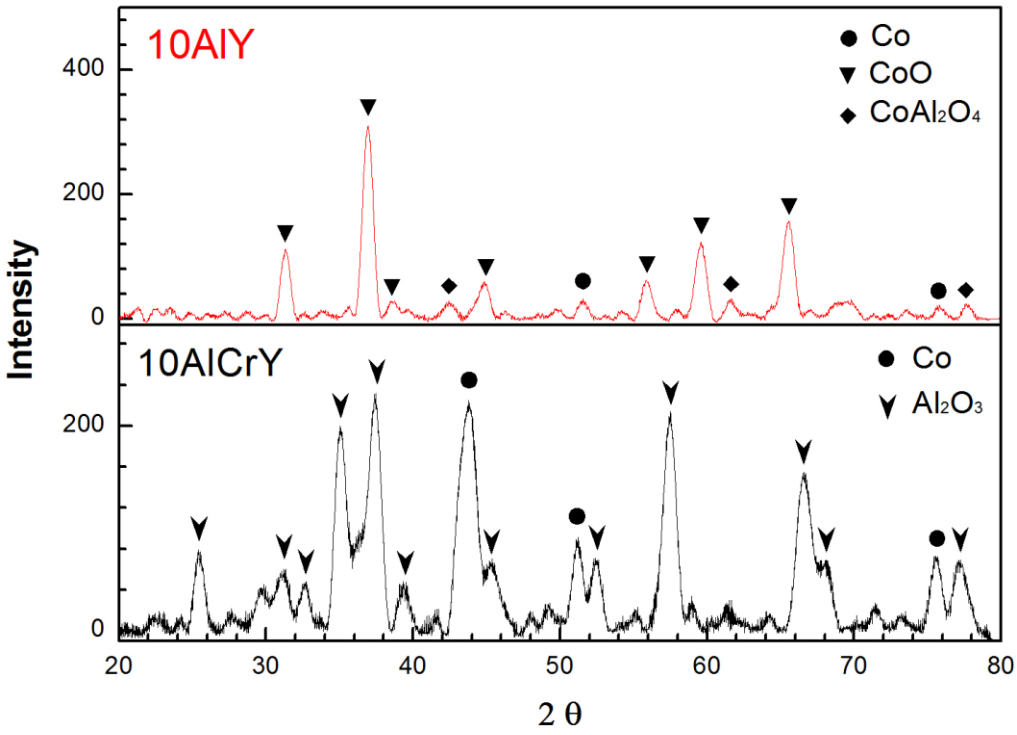

Fig. 5.19 XRD results for the 10AlY samples and the 10AlCrY samples after 225 h at 900 ºC in air.

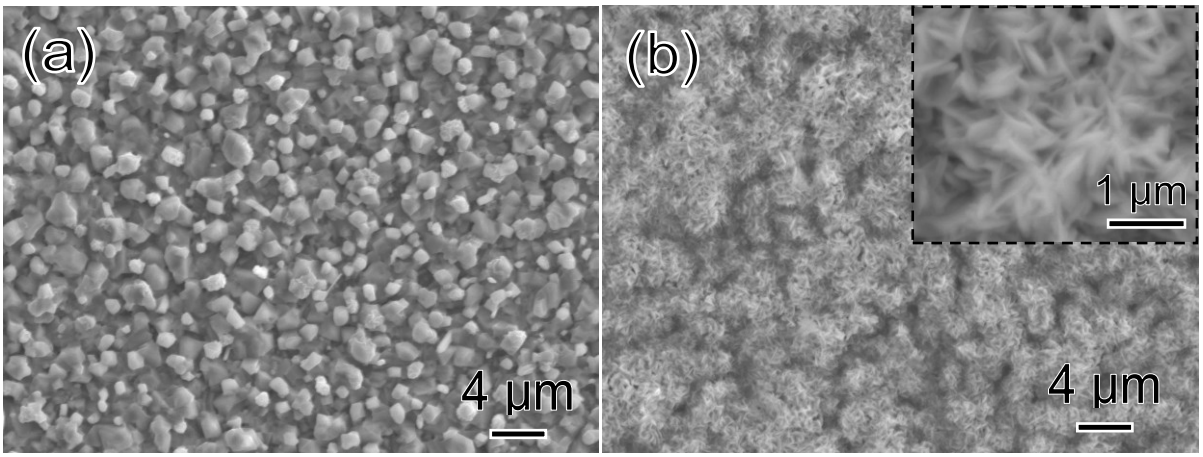

Fig. 5.20 Surface morphologies of oxide scales oxidized in 25 h at 900 ºC, (a) for 10AlY sample and (b) for 10AlCrY.

The cross-sections of oxide scale formed on 10AlY and 10AlCrY after different exposure time (1h, 4h, 25h and 100h) at 900 ºC were observed. **Fig. 5.21** shows the results of 1 h, in which the EPMA elemental mapping was conducted to investigate the initial scales. A thin oxide scale was found in the 10AlCrY sample, as shown in the **Fig. 5.21 (a)**, an Al-containing scale developed near the dark area (B2) and a Cr-containing scale formed on the gray area (fcc). In contrast, **Fig. 5.21 (b)** shows an obvious gray oxide film (CoO) on the surface of the 10AlY sample, which is much thicker than the scale formed in the 10AlCrY sample. Besides, Al_2O_3 was confirmed to form below the outer cobalt oxide.

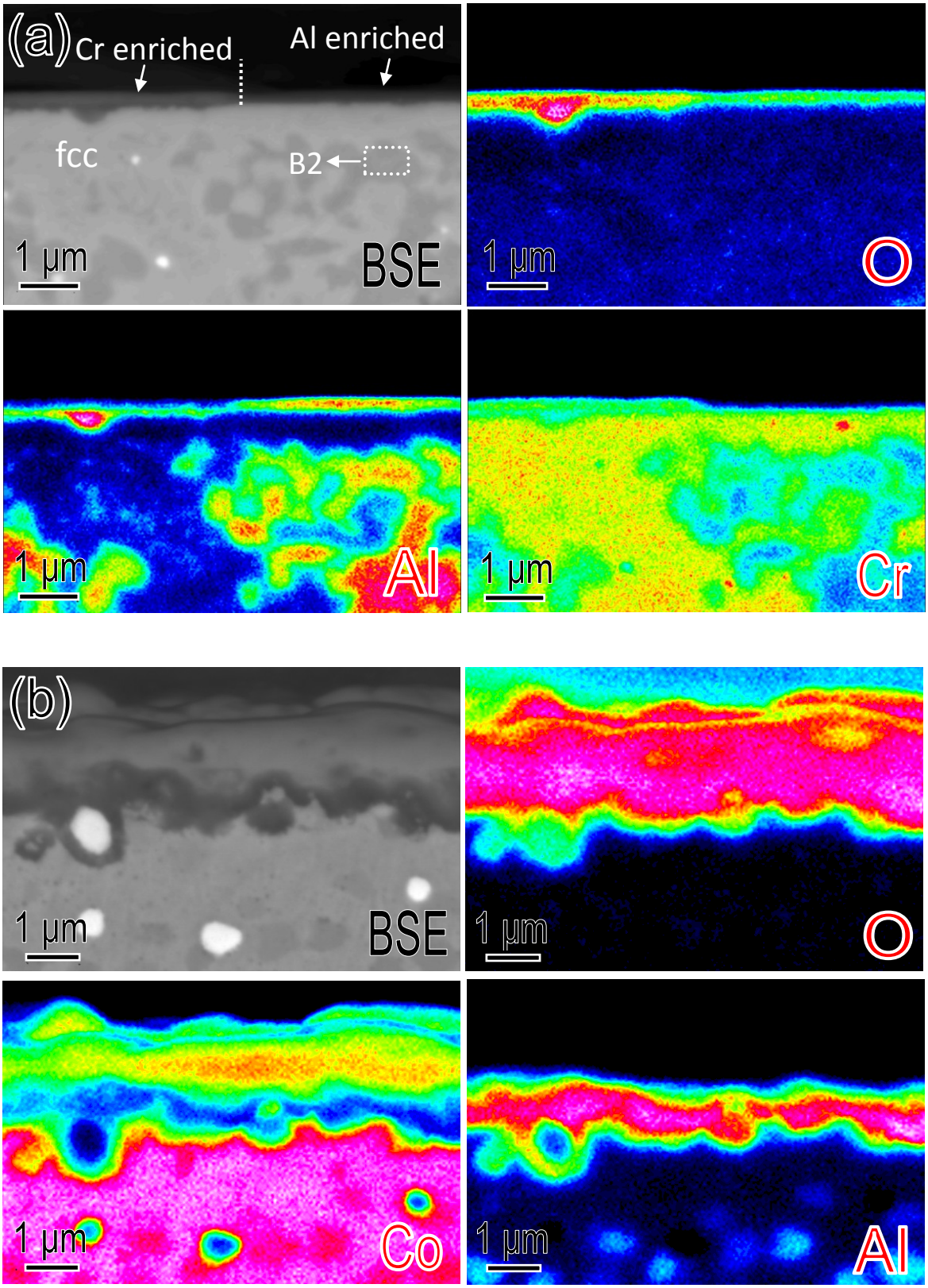

Fig. 5.21 EPMA elemental mappings obtained from the 10AlCrY sample (a) and the 10AlY sample (b) oxidized at 900 ºC with1 h.

Fig. 5.22 shows the cross-sections of 4h, 25h and 100h, based on a different contrast in the oxide layers with the back scattered electron image (BSE), the formation of a multilayered oxide scale on the 10AlY alloys and a single scale on 10AlCrY samples could be confirmed along with the oxidation time.

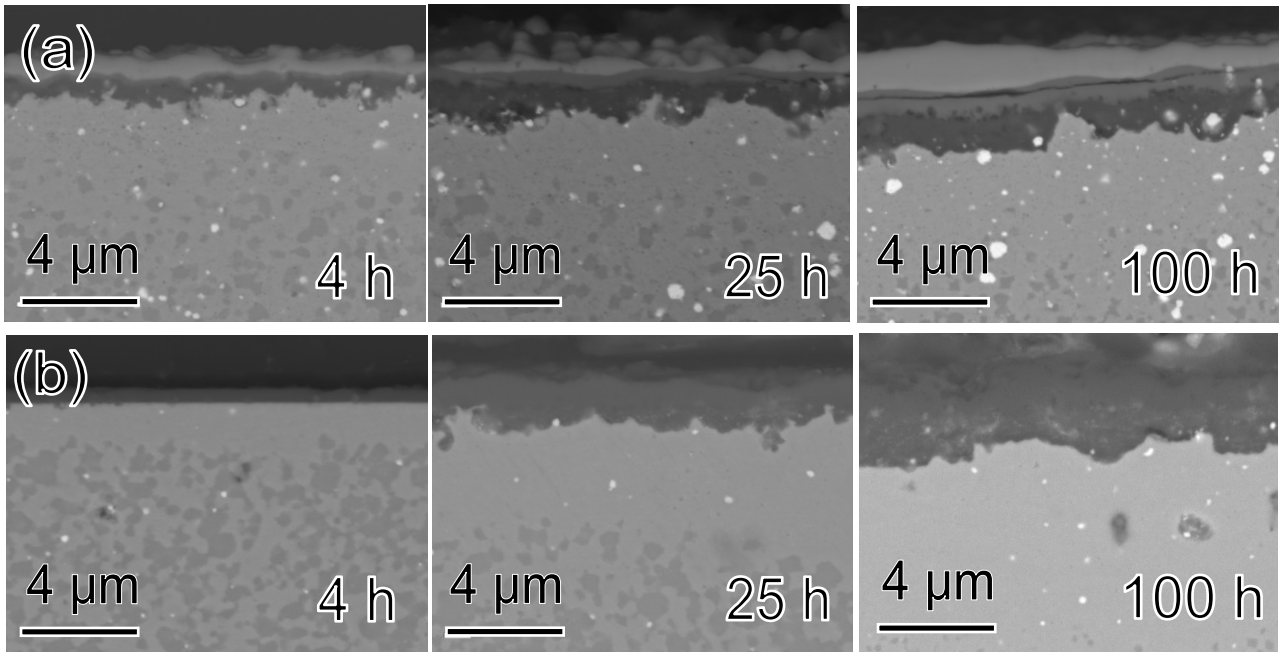

Fig. 5.22 The scales morphologies of oxidized samples with different exposure time (4 h, 25 h, 100 h) at 900 ºC, (a) is 10AlY samples and (b) is 10AlCrY samples.

In order to make certain of the element distribution in each oxide scale, the EPMA elemental mappings of the cross-sections were conducted and the results are presented in **Fig. 5.23**. **Fig. 5.23 (a)** proves that the oxide scales in the 10AlY alloys are composed of three layers; i.e. in addition to an external scale containing Co and an inner scale including Al, there is another intermediate layer of enriched Co and Al. **Fig. 5.23 (b)** shows that the homogeneous oxide layer in the 10AlCrY contains aluminum and oxygen elements, which could be easily defined as alumina according to the results of XRD. The chromia was not able to be identified at 25 h.

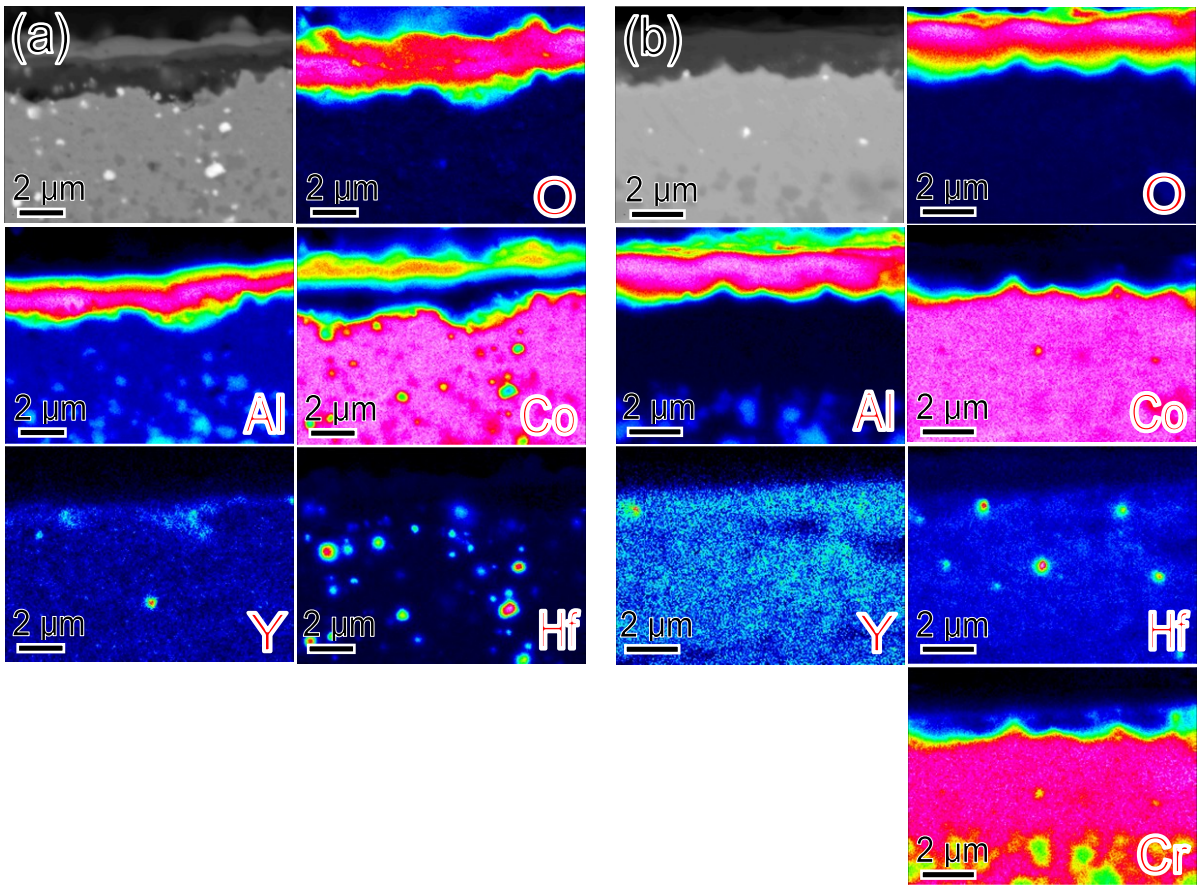

Fig. 5.23 EPMA elemental mappings obtained from 10AlY (a) sample and 10AlCrY (b) sample oxidized at 900 ºC for 25 h.

The EPMA WDS point analysis was carried out to more accurately determine the complex scales in the 10AlY alloys with 225 h, as shown in **Fig. 5.24**. Results suggested that the atomic percentages of all layers are approximate to external CoO, inner Al_2O_3 and intermediate layer of $CoAl_2O_4$. Besides, the outer CoO is found to be uneven with different thickness as well as the inner Al_2O_3 is decorated with amounts of white secondary particles, as shown in the **Fig. 5.25** of the fractured cross-sections.

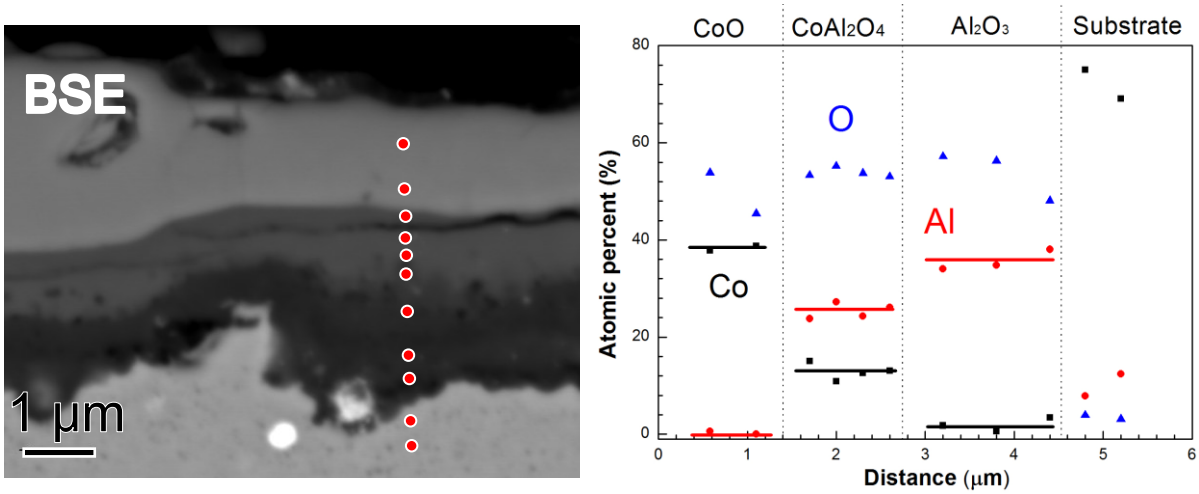

Fig. 5.24 The EPMA WDS point analysis on the metal atomic percent of the 10AlY samples oxidized at 900 ºC for 225 h.

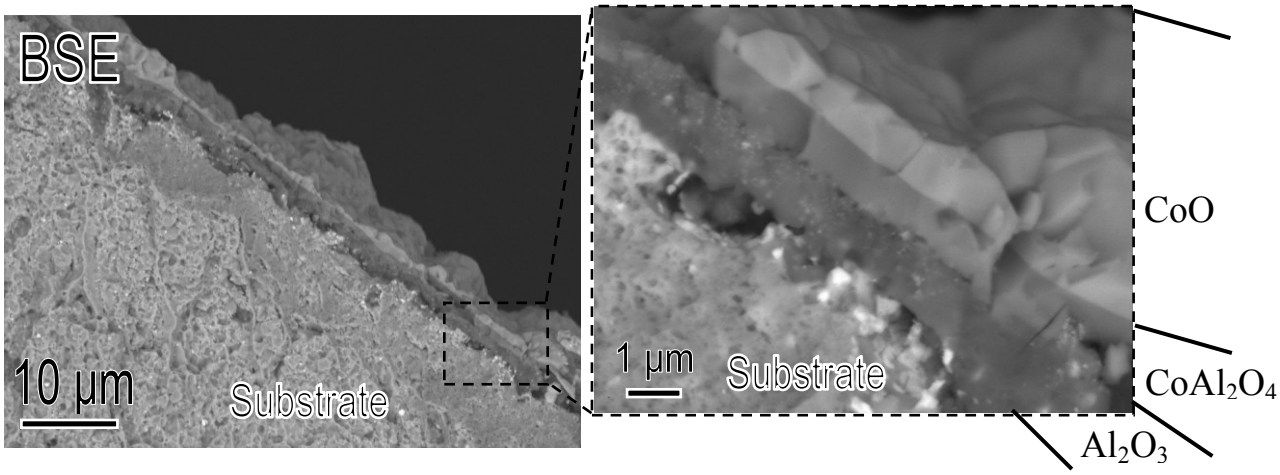

Fig. 5.25 SEM images of the fractured surface obtained from the 10AlY alloys oxidized at 900 ºC in 100 h.

At temperature increasing to 1000°C, a drastic weight loss happened in the 10AlY samples, whilst keeping a smooth oxidation process in the 10AlCrY alloys, as shown in the **Fig. 5.26**. The cross sections of two samples oxidized at 1000°C were observed with SEM and the results are exhibited in **Fig. 5.27**. In comparison with a stable scale in the sample of 10AlCrY, the scales of 10AlY are found to be heterogeneous and seem to be easily detached from the outer layer, which is well consistent with the weight loss. The EPMA elemental mapping (**Fig. 5.28)** confirms that the incomplete film at outer layer is CoO.

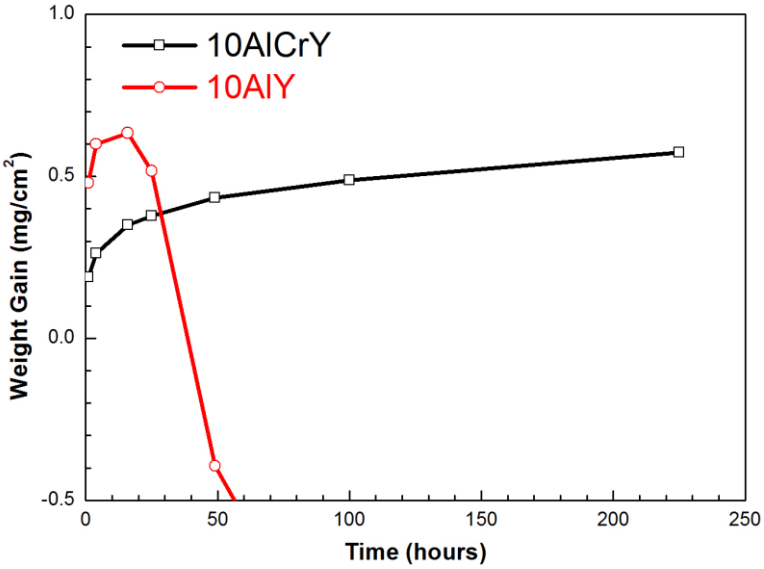

Fig. 5.26 Mass gain vs time curves of the 10AlY samples and the 10AlCrY samples oxidized at 1000 ºC in air.

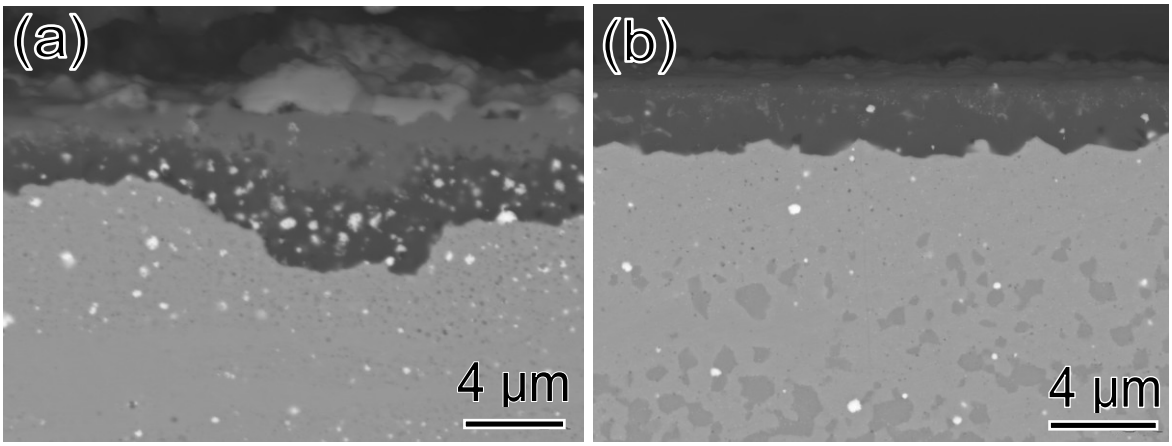

Fig. 5.27 Scales morphologies of the 10AlY (a) samples and the 10AlCrY (b) samples oxidized at 1000 ºC for 100 h.

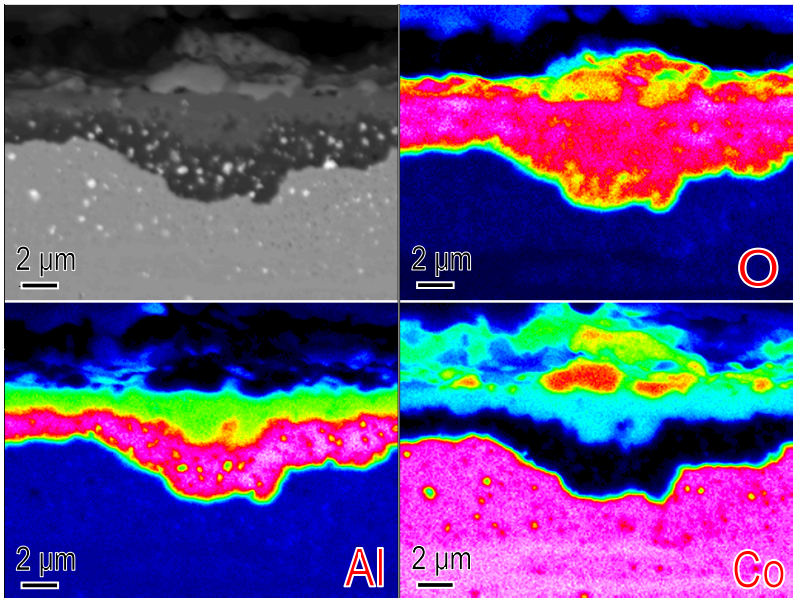

Fig. 5.28 EPMA elemental mappings obtained from the 10AlY samples oxidized at 1000 ºC for 100 h.

5.2.3 Effect of Y_2O_3-addition

Fig. 5.29 shows the oxidation kinetics of 10AlCr alloys at 900°C, in which the result of 10AlCrY is also inserted to highlight the effect of Y_2O_3 addition.

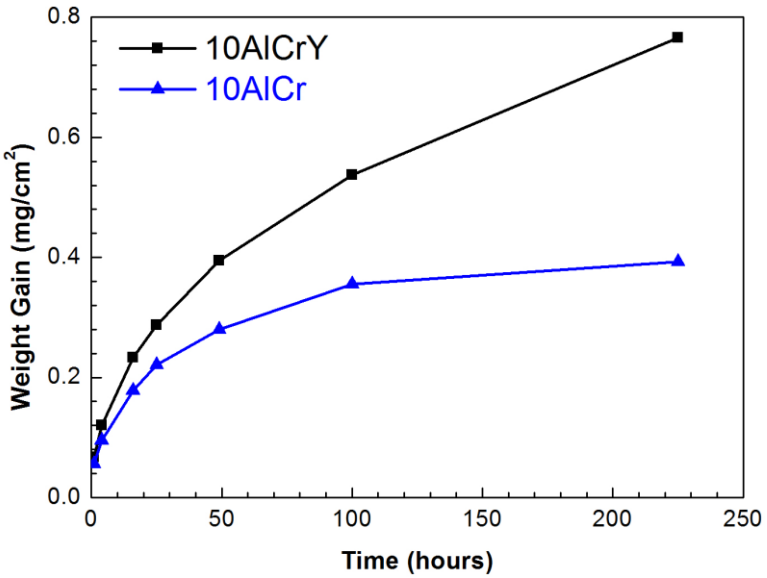

Fig. 5.29 Mass gain vs time curves of the 10AlCr samples and the 10AlCrY samples oxidized at 900 ºC in air.

In contrast to 10AlCrY ODS superalloys, the 10AlCr without yttria addition seems to maintain a better oxidation resistance, characterized by a smaller weight gain and a slower oxidation rate. Based on the XRD and EPMA characterization, as shown in **Fig. 5.30** and **Fig. 5.31**, the scale formed in the 10AlCr alloys was determined as alumina, too.

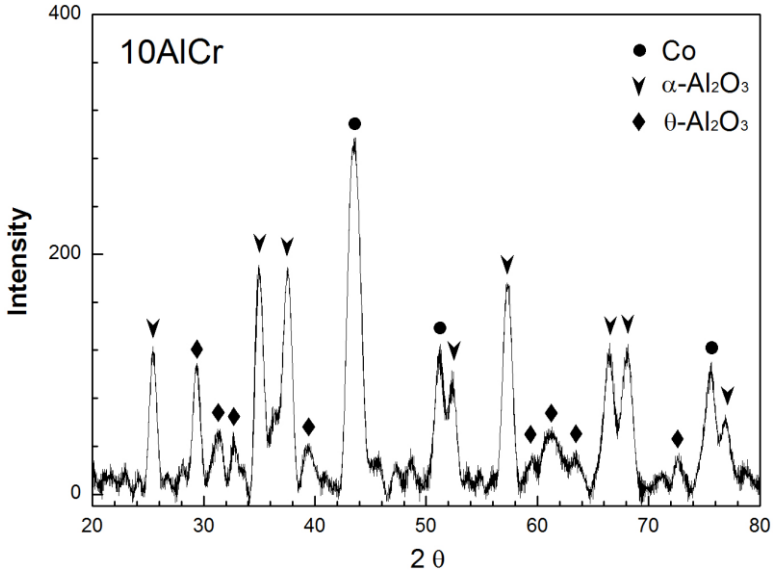

Fig. 5.30 XRD result for the 10AlCr samples oxidized at 900 ºC for 225 h in air.

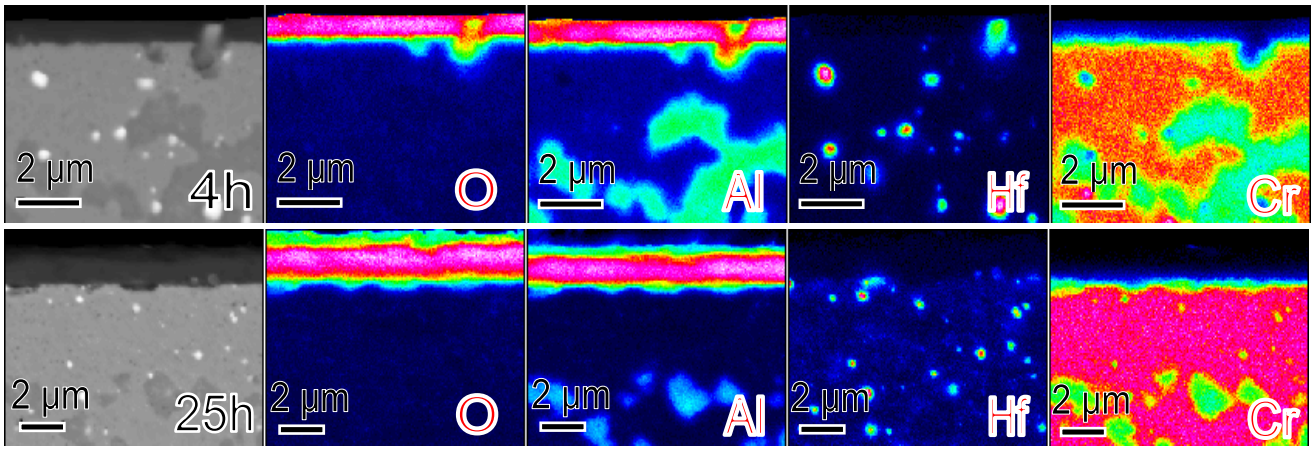

Fig. 5.31 EPMA elemental mappings obtained from the 10AlCr samples oxidized at 900 ºC with 4 h and 25 h.

However, amounts of voids along the matrix/scale interface in the 10AlCr have been found from the SEM images of **Fig. 5.32 (a)**, which evidences an inferior adherence of oxide scale in 10AlCr than that in 10AlCrY, and the detachment becomes serious along with the temperature increasing to 1000°C, as shown in **Fig. 5.32 (b)**.

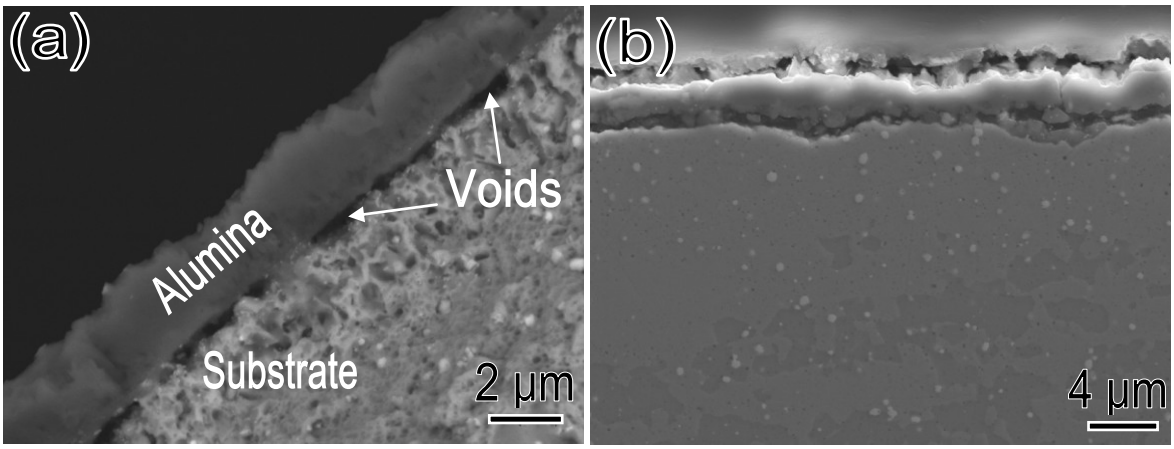

Fig. 5.32 SEM images of the 10AlCr alloys oxidized in 100 h at different temperature, (a) is fractured surface obtained at 900 ºC and (b) is cross-section obtained at 1000ºC.

In order to distinguish the difference between the two alumina scales generated in 10AlCr and 10AlCrY at 900°C, the TEM observation was performed on cross-sections, as shown in **Fig. 5.33**. It's obvious that the Al_2O_3 scale in 10AlCrY has been decorated with a mass of particles through comparing the TEM bright-field images of **Fig. 5.33 (a)** and **(b)**. Besides, the alumina grains in the 10AlCrY samples are quite smaller than that in the 10AlCr, as shown in the TEM dark-field images of **Fig. 5.33 (c)** and **(d)**.

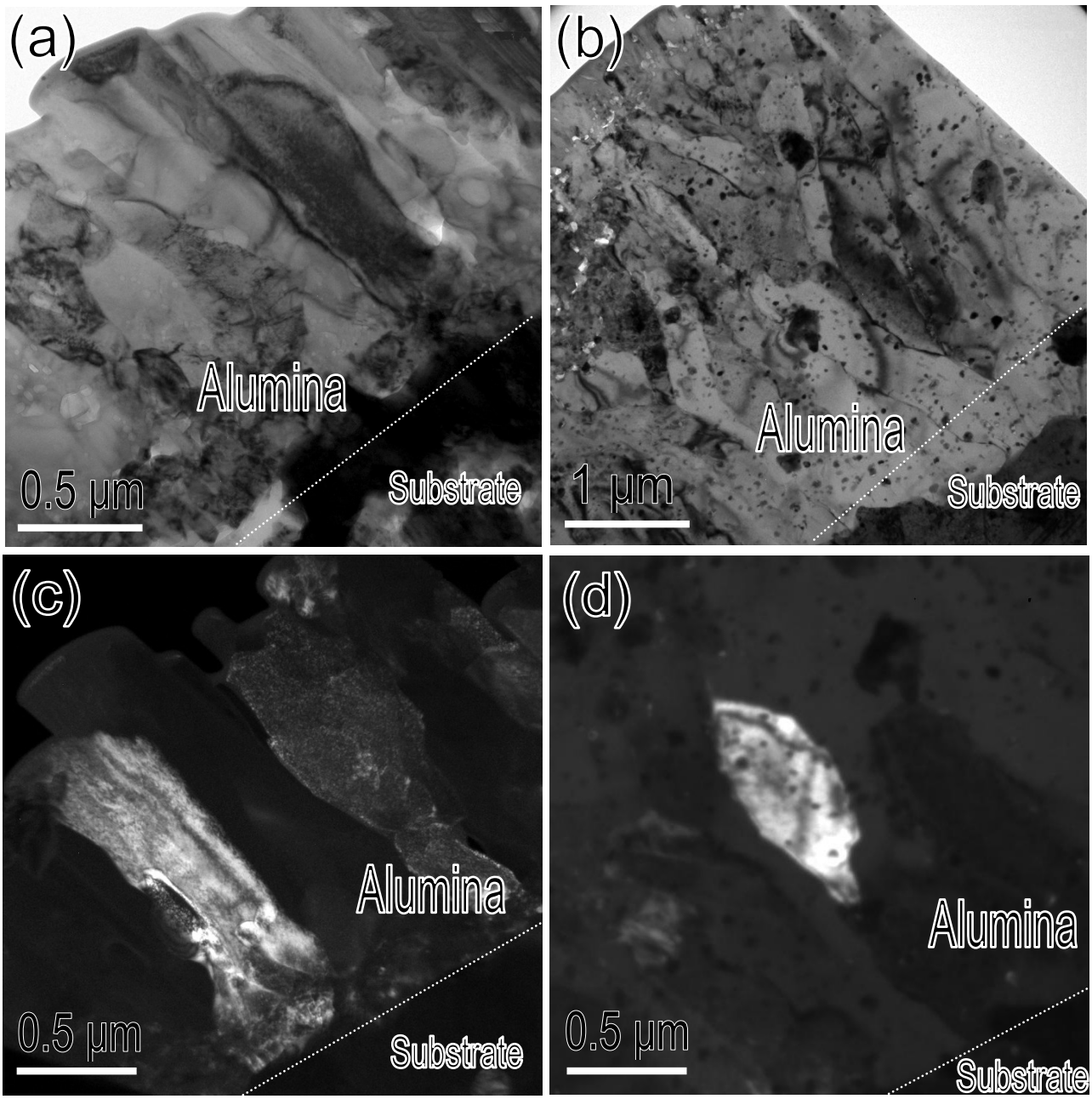

Fig. 5.33 (a) and (b) represent the alumina scales obtained from the 10AlCr samples and the 10AlCrY samples at 900 ºC for 225 h with the TEM bright-field pattern, (c) and (d) show the morphologies of the alumina grains in 10AlCr and 10AlCrY with the TEM dark-field pattern.

Based on the EPMA elemental mappings of Y and Hf in the alumina-scale (**Fig. 5.34)**, and the unique Hf-included oxides with white contrast, those secondary particles were determined as Y-Hf oxides in accordance with the oxides characterization in reference [68].

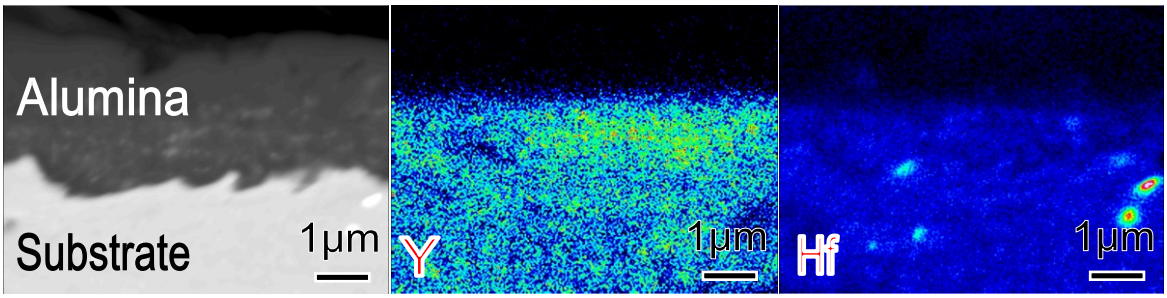

Fig. 5.34 EPMA elemental mappings of Y and Hf in alumina scales of the 10AlCrY samples oxidized at 900 ºC for 100 h.

5.3. Discussion

5.3.1 Effect of Al-content

The present results confirm that both the 5AlCrY and the 10AlCrY Co-based ODS superalloys possess a superior oxidation resistance with favored scale adhesion and a slow oxidation rate at 900 °C and 1000 °C. In addition, due to the increasing of Al content from 5 wt.% to 10 wt.%, 10AlCrY samples shows a higher oxidation resistance with the formation of the exclusive alumina scale. The oxide scales formed on those two Co-based ODS superalloys seem to fit with the conventional Co-Cr-Al oxide map [20] even the oxide particles had been implanted during alloy manufacturing, as shown in **Fig. 5.35**.

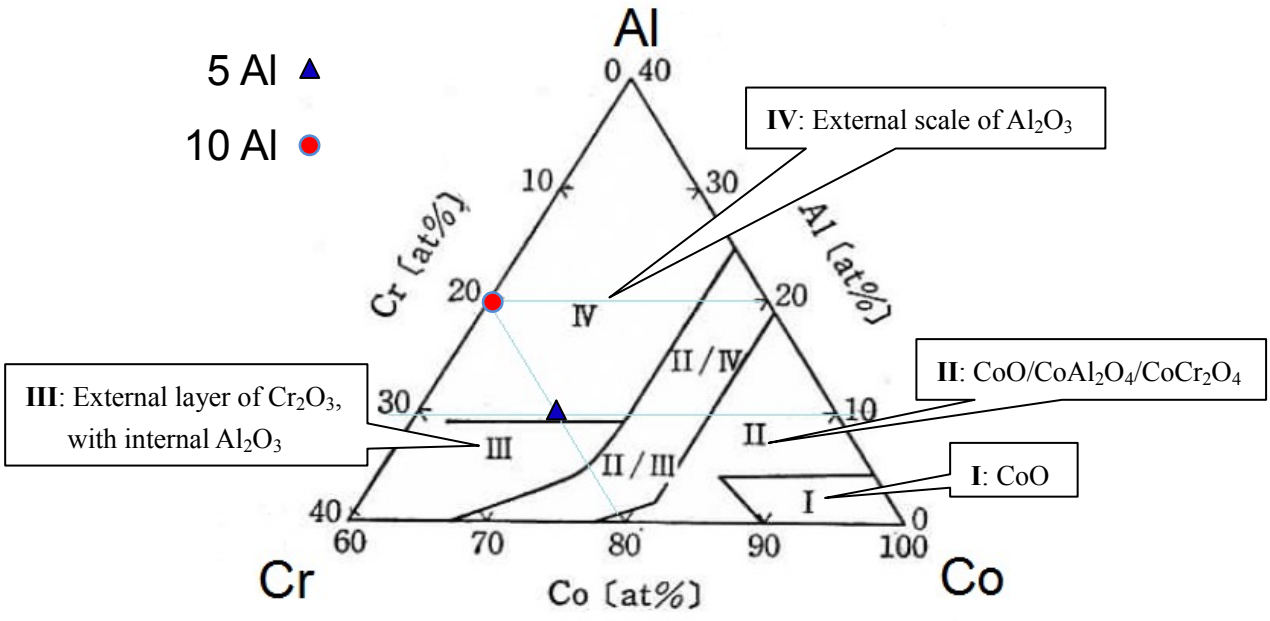

Fig. 5.35 The oxide map of the Co-Cr-Al system at 1000 °C

The 10Al (20 at.%) sample exhibits single alumina former as well as 5Al (10 at.%) shows duplex scale with an outer chromia and inner alumina. The only difference is the existence of $CoCr_2O_4$ scale in 5AlCrY samples, which is thin at 900 °C but thicker at 1000 °C. In the case of Cr-containing Co-based alloys, the cobalt is oxidized to CoO and could in turn react with Cr_2O_3 to form the protective $CoCr_2O_4$ compound oxide with a spinel structure [21, 48, 49, 70]. The formation of this $CoCr_2O_4$ oxide in the Co-based ODS alloys was supposed to owe to the small substrate grain size, which could significantly improve the diffusivity of the Co along substrate grain boundaries [71].

Fig. 5.36 shows the comparison of k_p values between the 5AlCrY and the 10AlCrY samples with the reported chromia- and alumina-forming alloys [72, 73].

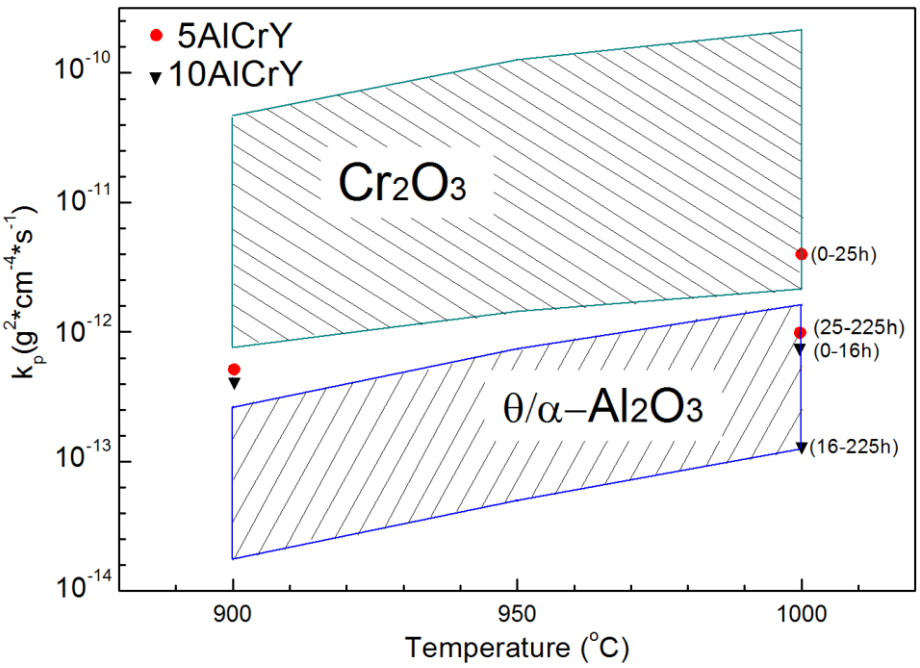

Fig. 5.36 Comparison of the parabolic rate constants between the 5Al and 10Al samples with reported Cr_2O_3 and Al_2O_3 formers.

In respect of 5AlCrY samples, the k_p value is constant and lower than conventional chromia-forming alloys at 900 °C. Whilst it is separated into two stages at 1000 °C; the k_p value is close to the minimum value of the reported chromia-forming alloys at the initial stage (-25 h) and reaches the region of alumina-forming alloys at later duration (25-225 h). As shown in the XRD pattern

(**Fig. 5.3**) and EPMA elemental mapping (**Fig. 5.7**), in addition to the Cr_2O_3 scale, the existence of outer $CoCr_2O_4$ layer and inner Al_2O_3 oxides have been proved, which is associated with the lower oxidation rate of 5AlCrY than the conventional chromia-forming alloys. With the temperature increasing to 1000 °C, the formation of the inner Al_2O_3 scale has been enhanced, which is responsible to the altered k_p value at 1000 °C. Once the continuous Al_2O_3 scale formed, the oxidation behavior could be dominated by this inner Al_2O_3 layer since a more compact structure. In the case of 10AlCrY specimen, **Fig. 5.13** exhibits that the 10AlCrY possesses a faster oxidation rate than conventional alumina former at 900 ^oC in 225 h. This reason could be associated with the formation and a faster growth of θ- alumina. After increasing the temperature to 1000 °C, as described in previous sections, 10AlCrY samples also exhibited an altered k_p. The changing of the k_p value after 16 h in the 10AlCrY is attributed to a rapid transformation from θ- to α-alumina at 1000°C, the details will be expounded later.

In addition, **Table 5.3** lists the comparison of high-temperature oxidation behaviors between different kinds of alloys, in which the non-ODS Co-based alloys and typical Ni-based and Fe-based ODS superalloys have been introduced [20, 22, 74, 75]. It's obvious that the oxidation resistance of the 5AlCrY and the 10AlCrY is better than the listed conventional Co-based alloys, and even comparable to the Ni-based and Fe-based ODS superalloys with the approximate magnitude of k_p. A different transport mechanism of scale growth has been claimed in the non-ODS and ODS Fe and Ni-based alloys [18, 19, 51, 76], i.e., the α-Al_2O_3 scale growth on conventional alloys is conducted with cation as well as oxygen transport along grain boundaries, but for the ODS alloys with yttria participation, the diffusion of cation is blocked and leading to a reduced cation outward transport, in which the growth is dominated by inward oxygen grain boundary transport. The restrained cation diffusion imparted by oxide particles addition seems to also play a role in the case of the Co-based ODS superalloys, since amounts of fine oxide particles inside alumina scales were observed. The particles with white contrast were confirmed to be Y-Hf-O dispersoids, which are formed during the manufacturing process and possess extremely high thermodynamic

stability [23, 68]. The particles were existed in the substrate before oxidation, and incorporated in the alumina scale due to the metal surface recession with the growth of alumina. Hence, the particles in alumina scales are a kind of the marker to indicate the original metal surface.

Table 5.3 Comparison of oxidation behaviors between alloys.

Alloy (wt. %)	Temp. (^oC)	Oxidation behavior	k_p ($g^2 \cdot cm^{-4} \cdot s^{-1}$)	Reference
5AlCrY (ODS Co-20Cr-5Al)	900	Duplex scale of outer $CoCr_2O_4$ and innerCr_2O_3, internal formation of Al_2O_3 particles	6.9×10^{-13}	--
	1000	Duplex scale of $CoCr_2O_4$ and Cr_2O_3, but voids in outer $CoCr_2O_4$ layer, Al_2O_3 scale generated internally	6.0×10^{-12} 9.9×10^{-13}	--
10AlCrY (ODS Co-20Cr-10Al)	900	Alumina scale with the co-existing of θ- and α-alumina	6.5×10^{-13}	--
	1000	Alumina scale dominated with α-alumina	8.7×10^{-13} 1.1×10^{-13}	--
Co-10Al	1000	Al_2O_3 formed initially, but breaks down with the formation of $CoAl_2O_4$	5.0×10^{-9}	20, 21
Co-20Cr-10Al	1000	Alumina scale with low adherence	$\leq 5\times10^{-12}$	20
MA 754 (ODS Ni-20Cr)	900	Chromia scale	4.0×10^{-14}	19, 73
	1000		1.0×10^{-12}	
PM 2000 (ODS Fe-20Cr-5.5Al)	880	Alumina scale	2.77×10^{-13}	19, 75
	1050		1.23×10^{-12}	

In the case of 10AlCrY samples oxidized at 900 °C, the particles were observed in the middle part of alumina scale, which means the alumina containing the particles grew inward and the upper parts with free particles grew outward. According to the particles distribution, the alumina scale in 900 °C could be separated and defined to be the outer and inner part, as marked in the **Fig. 5.9** and **Fig. 5.11**, referring the layer determined by outward and inward growth, respectively. With increasing the temperature to 1000 °C, the outer layer was still formed, but it is much thinner than that formed at 900 °C, as show in the **Fig. 5.9** and **Fig. 5.11**. The particles were found

to substantially decorate in the area beneath this extremely thin outer layer, suggesting the growth of the alumina scale was mainly toward the substrate, i.e., the Y-Hf oxide particles exist in outer part of the inner layer at 1000 °C.

I consider furthermore that the 10AlCrY superalloys have to experience a relatively complex oxidation process due to the existing of metastable θ-alumina at 900 °C-1100 °C [77]. The growth process of θ-alumina has been certified to be dominated by the outward aluminum diffusion [66], fitting the most outer layer in the 10AlCrY samples at 900 °C, in which besides the unique blade-like structure, almost no particles could be detected. However, according to the changing k_p value at 1000 °C, which is first high and then decreased, the θ-alumina should also exist in the early part of oxidation since several faint θ-alumina peaks were detected in XRD patterns, but it rapidly transformed to α-alumina during the initial stage at 1000 °C, resulting in the formation of the extremely thin outer layer. After formation of α-alumina, scale growth is controlled by the inward oxygen diffusion, the Y-Hf oxide particles could be detected in the outer part of the inner layer at 1000 °C. Besides, the alumina grains would enlarge in direction of the scale/substrate interface due to the decreased nucleation rate [51, 78], which is consistent with the coarsening alumina grains near the substrate for the 10AlCrY samples at 1000 °C, as shown in the **Fig. 5.11 (b)**.

The different oxidation processes of the 10AlCrY samples oxidized at 900 °C and 1000 °C are shown schematically in **Fig. 5.37**. In the very beginning of oxidation t_1, the θ-alumina preferentially grows outward from the original surface of substrate since a high growth rate. Subsequently, the α-alumina generates at the θ-Al_2O_3/alloy interface, as shown in the stage of time t_2, in which amounts of particles are distributed. Within the t_3 period, the oxidation of the 10AlCrY samples at 900 °C is composed of outward growth of θ- alumina and inward growth of α-alumina, leading to the newly formed θ- alumina without Y-Hf oxide particles in the outer layer at 900 °C. However, at 1000 °C the scale is dominated by the inward growth of α-alumina. Therefore, the outer oxide layer was very thin. Due to the low solubility of hafnium [23] and the sparse grain boundaries with coarse grain size in the inner layer

of α-alumina scale, few Y-Hf oxide particles could be observed at this inner layer. Besides, an accelerated transgranular/intergranular outward diffusion of yttrium and hafnium ions at high temperature had been considered to play a certain role on the coarsening and enrichment of Y-Hf oxide particles on the outer layer [78, 79], which is consistent with the special tail structure and the enrichment of Y and Hf on grain boundary, respectively.

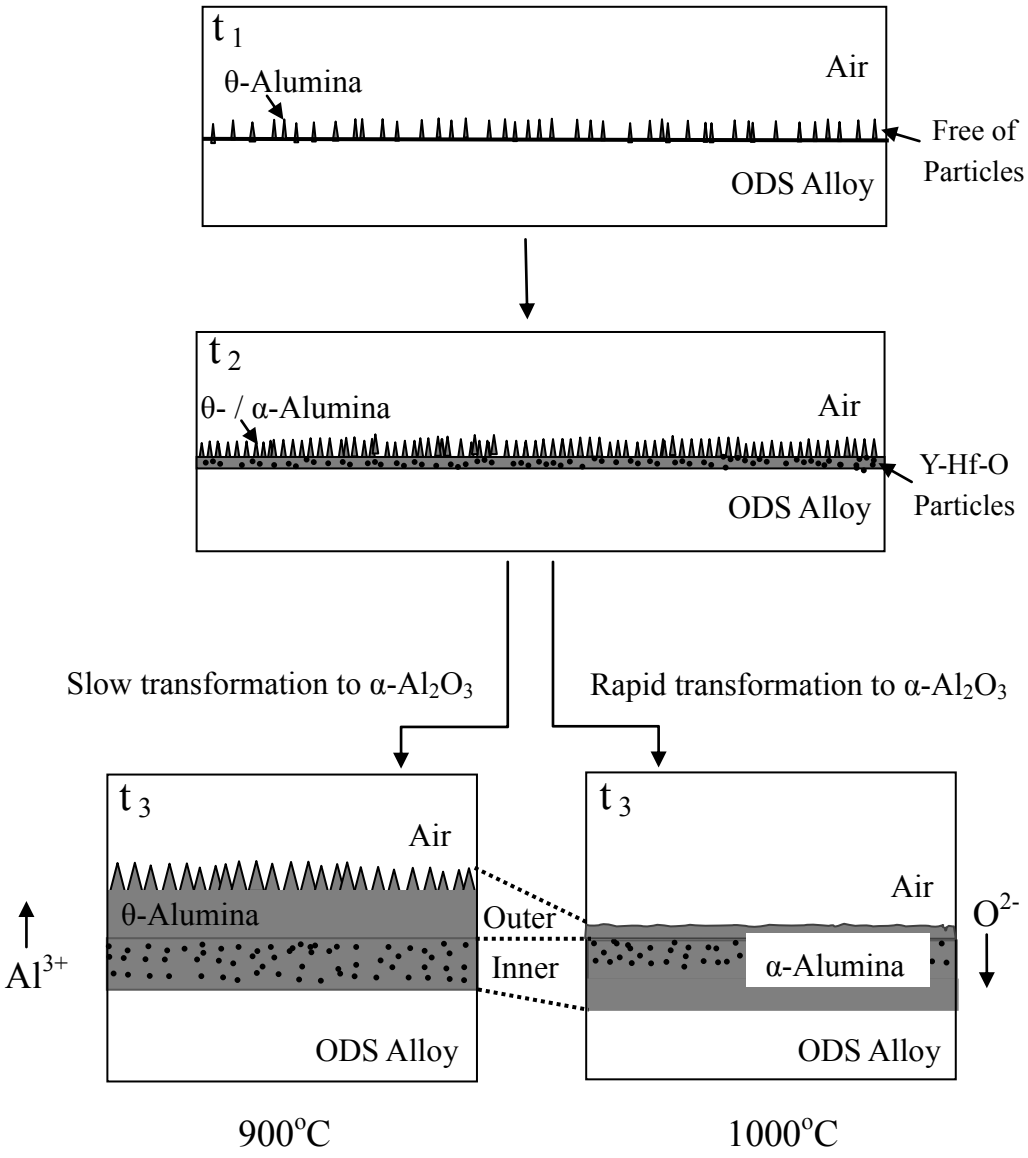

Fig. 5.37 Schematic illustrating the oxidation processes on the time dependence ($t_1 < t_2 < t_3$) of the 10AlCrY samples oxidized at 900 °C and 1000 °C.

5.3.2 Effect of Cr-addition

In comparison with a smooth mass gain of the 10AlCrY sample, the 10AlY sample without Cr addition shows a fluctuant oxidation process, i.e. an extremely rapid oxidation rate at the beginning of the oxidation in the first 1 h and a significantly reduced oxidation rate at the late period. When the growth of oxide scale is controlled by diffusion through the oxide scale, mass gain follows a parabolic law [80, 81]:

$$\Delta W = \sqrt{k_p}\sqrt{t} + C \tag{5.1}$$

where ΔW is the weight gain of the sample taken for unit surface area, k_p is the parabolic rate constant, t is the time of exposure and C is a constant which showed the deviations from the parabolic law during the initial stages of oxidation. **Fig. 5.38** shows the mass gains as a function of square root of time, in which the solid line denotes the fitted results.

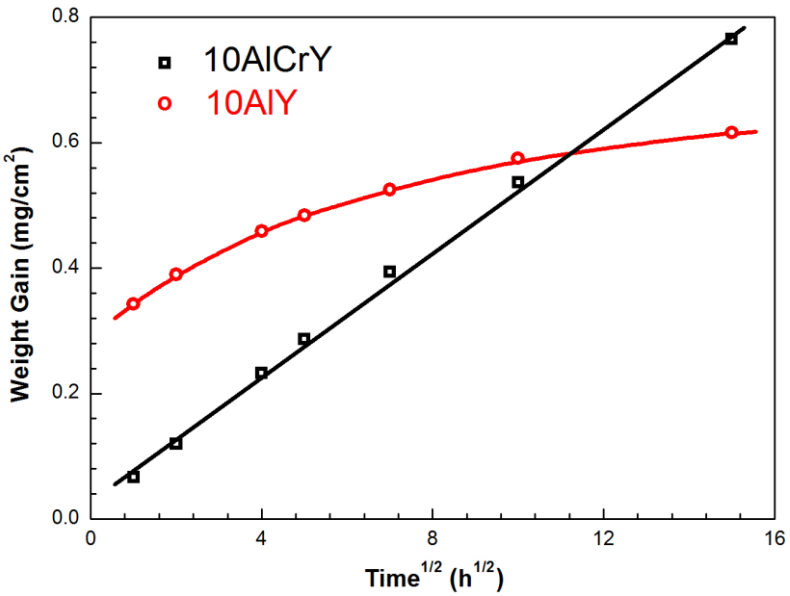

Fig. 5.38 The fitted parabolic curves for the 10AlY sample and the 10AlCrY sample oxidized at 900 ºC for 225 h in air.

According to the kinetic measurements, the oxidation of the 10AlCrY sample follows in the parabolic law, where the values of k_p and C are corresponding to 6.5×10^{-7} mg^2·cm^{-4}·s^{-1} and 0.01 mg/cm^2, respectively. However, one straight line cannot be drawn throughout the whole oxidation of 225 h in 10AlY since a multiply

oxide scale in the 10AlY sample. If we deal these data particularly, the 10AlY seems to be composed of two different oxidation stage, i.e., a rapid mass gain in the initial stage (0-1 h), and another reduced oxidation kinetic which possesses a increasingly slow oxidation rate in the subsequent oxidation (1-225 h), as shown in the **Fig. 5.38**.

At the initial stage of oxidation, the 10AlY sample forms Co oxides and results in a continuous Co-oxide scale in an external layer, as shown in the **Fig. 5.21 (b)**, an obvious gray oxide film (CoO) was found on the surface of the 10AlY sample at 1 h oxidation, which is much thicker than the scale formed in the 10AlCrY sample. Therefore, the rapid mass gain of 10AlY sample during the initial oxidation stage (0-1 h) should be attributed with the formation of the outer Co-oxides which have much higher growth rate [85]. In the subsequent oxidation stage, an evident growth of an inner scale with black contrast is observed, which was determined to be alumina by EPMA elemental mappings in **Fig. 5.23 (a)**. Since a more compact structure of alumina than the Co oxide, the oxidation process would be slowed down by the inner alumina layer and results in a decrease of the oxidation rate in the 10AlY sample. Additionally, the growth of the inner alumina could be restricted with a limited oxygen supply due to the cover of outer CoO and $CoAl_2O_4$ spinel oxides layer. Besides, with the elongation of exposure time, a noticeable increase in the thickness of the intermediate $CoAl_2O_4$ layer could be observed, as shown in **Fig. 5.22**. The spinel structure of $CoAl_2O_4$ layer was confirmed with a significant blocking effect on the diffusion of cation and anion [70], which is responsible for the oxidation kinetics at a slower and slower rate along during oxidation. The overall oxidation is considered to be still controlled by oxygen and/or Al diffusion in the inner Al_2O_3 scale. However, such an uncontinuous change in the thickness of each layer may result in deviation of oxidation kinetics from the parabolic behavior.

With the addition of Cr, the formation of Co-oxides is suppressed and a thin oxide scale enriched Al and Cr is produced in the surface of the 10AlCrY sample at 1 h, as shown in the **Fig. 5.21 (a)**. EPMA mapping indicates that an initial chromia (Cr_2O_3) scale formed on 10AlCrY particularly on the regions of fcc matrix, which contains higher Cr content. Subsequently, chromia could be dissolved into the alumina because

both phases undergo a complete solid solubility at 900 °C. It is well known that the presence of Cr in Fe- and Ni-based alloys could reduce the Al level needed to form a protective Al_2O_3 layer [83, 84], defined as the third-element effect (TEE) [85]. It describes that the addition of a third-element B to binary A–C alloys can decrease the critical C concentration needed to establish an external scale of the C oxide, in which A is the most inert element and C is the most reactive one in the ternary system [83]. The TEE seems to work in the Co-based ODS superalloys, since the Cr possesses an oxygen affinity falling in between those of Co and Al, and also the addition of Cr reduces the concentration of Al required to establish an external alumina scale, as shown in the **Fig. 5.22** where an exclusive alumina scale could be formed through adding Cr to the 10AlY samples. The mechanism of TEE is not yet completely clear, but based on the suggestion claimed by Wagner [85, 86], it was supposed that an initially formed external Cr_2O_3 scale promotes Al_2O_3 formation. In this study I could not observe Cr_2O_3 formation at the very early stage of oxidation. However, Cr_2O_3 formation is expected since Cr-containing scale was observed after 1 h oxidation and Co-rich oxide scale formation was completely suppressed by Cr addition.

In addition, based on the phase diagram (**Fig. 5.16**), due to the addition of 20Cr (wt. %), the volume fraction of CoAl (B2) is significantly increased from 39% in the 10AlY to 50% in the 10AlCrY, which is consistent with the increase of the dark areas (B2) from **Fig. 5.17 (a)** to **(b)**. One point should be noted that the aluminum concentration in the B2 phase is almost triple than that in the fcc phase. At the initial stage of oxidation, the alumina scale is easier to generate at the surface of B2 phase than at fcc phase. Due to higher volume fraction of CoAl in 10AlCrY alloy, Al content in fcc matrix must be decreased. Although this decrease in Al content in fcc matrix is not favored for Al_2O_3 scale formation, fcc matrix contained higher Cr, which promotes external Al_2O_3 scale formation by TEE as mentioned above. In fact, as shown in the **Fig. 5.21**, a compound oxide scale was found at the 10AlCrY samples oxidized at 900°C for 1 h, i.e. a Cr-containing scale formed on the gray area (fcc) and an Al-containing scale generated near the dark area (B2). This indicates that a chromia (Cr_2O_3) scale was also initially formed in 10AlCrY and could be a reason why the

initial weight gain is suppressed for 10AlCrY, as shown in **Fig. 5.18**. Subsequently, chromia could be dissolved into the alumina because both phases undergo a complete solid solubility at 900 ^{o}C. The 10AlY which does not contain Cr preferred to form Co oxides due to a high percentage of cobalt solid solution regions, resulting in a continuous Co-oxide scale at external layer. Even though initially small amounts of alumina could generate at the sites of B2 phases in 10AlY, it is insufficient to evolve to be a complete outer scale since the limited aluminum flux. However, the formation of CoO near the B2 phase should be suppressed significantly, which leads to the uneven morphology of the outer CoO scale with different thickness, as shown in the **Fig. 5.25**. Consequently, the rapid weight gain of 10AlY samples during initial oxidation stage is considered to be induced by the faster growth rate of outer Co-oxides.

However, beneath this CoO layer, another thicker scale with black contrast had formed at inner layer after 25 h, which was confirmed to be alumina with EPMA elemental mappings in **Fig. 5.22 (a)**. Due to a more compact structure, this continues alumina scale in inner plays a dominated effect for the oxidation resistance of the 10AlY during the later stage of the oxidation at 900^{o}C. Furthermore, this inner alumina possesses a slower growth rate with the cover of outer CoO and $CoAl_2O_4$ spinel oxides layer, which significantly reduced the oxygen inward diffusion and retarded the growth of the inner alumina layer. Hence, even though both oxidation processes of the 10AlY and 10AlCrY are dominated by alumina growth during the later stage of oxidation, a slower oxidation constant in 10AlY than in 10AlCrY could be observed, as shown in **Fig. 5.18**. The equilibrium phases in Co-Al-O system were calculated in the diagram of log P_{O2} (atm) vs. Al-mol fraction at 900 °C and 1000 °C by using thermodynamic software CaTCalc [87, 88], which is shown in the **Fig. 5.39**. At the composition of Co-20 at% Al, the formations of CoO, $CoAl_2O_4$ and Al_2O_3 are predicted with decreasing oxygen pressure. The distribution of scales is completely consistent with the results of EPMA point analyses in 10AlY (Co-10wt.% Al almost equals to Co-20 at.% Al), as shown in **Fig. 5.24**. The P_{O2} at the outer surface of the alumina-scale is reduced to 10^{-16} atm at 900 °C (**Fig. 5.39 (a)**), which is significantly

lower than that in the case of 10AlCrY, where alumina-scale directly contact with air (0.21 atm).

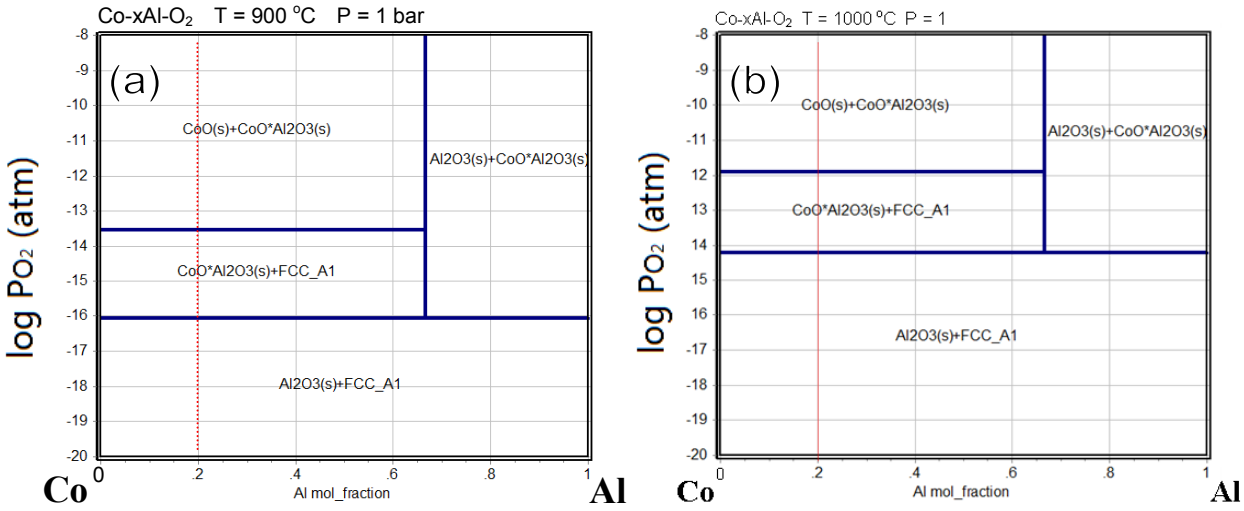

Fig. 5.39 The phase diagram of Co-Al-O system calculated with CaTCalc software at 900 °C (a) and 1000 °C (b).

However, at the interface of $CoO/CoAl_2O_4$, a visible cracking could be found with the exposure time of 100 h at 900°C, as shown in the **Fig. 5.22 (a)**. Due to a high growth rate of CoO and the large thermal stress caused by the mismatch of the coefficients of thermal expansion between the CoO and matrix, the detachment of CoO layer is usually observed in the Co-based alloys [48]. The detachment would be accelerated at higher temperature, as shown in the **Fig. 5.27 and 5.28**, and the spallation of CoO layer is associated with the significant weight loss in the 10AlY during exposure at 1000°C.

5.3.3 Effect of Y_2O_3-addition

In comparison with the appearance of various oxide scales with Cr addition, both the samples with and without Y_2O_3 addition maintain a single alumina scale. However, the formation mechanism of the alumina in 10AlCrY and 10AlCr should be separated because of the difference at oxidation kinetics and microstructure, i.e. the 10AlCrY

exhibits a larger weight gain and results in a thicker alumina scale than the 10AlCr alloys. The alumina scale in 10AlCrY is decorated with abundant secondary particles, and its grain size is smaller than that in the 10AlCr, as shown in the **Fig.5.33**.

Based on the reports that the dispersed particles could effectively decrease the alumina grain size in Fe-ODS and Ni-ODS superalloys [16, 18, 89], the fine grain size of alumina in 10AlCrY alloys is attributed to the distribution of Y-Hf complex oxide particles in the Al_2O_3 scale. Even though the single alumina scale is composed of θ- and α-alumina, the Al_2O_3 layer where with Y-Hf oxides distribution is supposed to be α-alumina since it grows towards inward [18, 51]. Therefore, the nucleation rate of α-alumina could be accelerated because the oxide particles are suitable sites for the nucleation of alumina formation [90]. In addition, due to the pinning effect of such dense oxide particles [55, 91], the grain enlargement of α-alumina scale could be effectively suppressed; many particles are locating within the alumina grains and dispersing along the grain boundaries, as shown in the TEM images (**Fig. 5.33**). Consequently, a high grain boundary density exists in the alumina-scale of 10AlCrY and it accelerates the transport of Al outward and oxygen inward, which was considered to be a reason to enhance the oxidation rate in the 10AlCrY.

In comparison with the shape of alumina grain in the 10AlCrY which is more close to equiaxed morphology, a noticeable columnar grain was observed in the sample of 10AlCr, as proved with the dark field pattern in the **Fig. 5.33**. **Fig. 5.40** shows the fitted parabolic curve of the 10AlCr sample. The oxidation kinetics of the 10AlCr seems to not conform to a parabolic law as well, and also an obvious reduction of the oxidation rate with the increasing of exposure time could be found. Based on the reports regarding to the alumina-forming scale on FeCrAl alloys [92, 93], the columnar grains with a lateral size of which increased linearly with depth beneath the scale surface is responsible for the reduction of the k_p value since a decreased density of grain boundary along with the exposure time. Even an overall distribution of the alumina grains has not been exhibited in the TEM images, the coarsening of the columnar grains with the direction toward to substrate was also supposed to occur in the 10AlCr since a decreased nucleation rate close to the interface of scale/substrate

with a restricted oxygen inward diffusion.

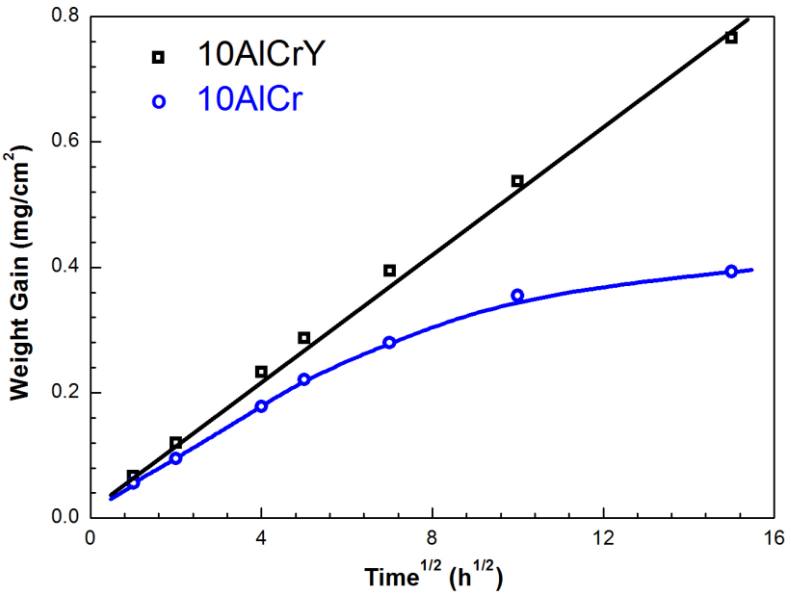

Fig. 5.40 The fitted parabolic curves for the 10AlY sample and the 10AlCrY sample oxidized at 900 ºC for 225 h in air.

However, as shown the fractured surfaces in **Fig. 5.32**, in comparison with a superior adherence of alumina scale in the 10AlCrY, some voids were detected along the alloy/scale interface of the 10AlCr after the exposure at 900 ^{o}C, and the cracking even happened when the temperature up to 1000^{o}C. In the case of conventional alloys, the voids could often be observed at the alloy/scale interface due to the Kirkendall effect [94, 95], but according to the suggestion by K. Arun et al. [96], the interfaces between Y-Hf oxide particles in the 10AlCrY were considered to act as vacancy sinks at sites away from the alloy/oxide interface, hence significantly suppressing the void formation and improving the oxide-scale adherence. Besides, the segregation of Y-Hf oxide particles along grain boundary could play a role on the reduction of voids by decreasing the cation outward diffusion with blocking effect [18, 51]. In addition, this small grain size of alumina in the 10AlCrY is sometimes beneficial to release the large thermal stress induced by the mismatch of thermal expansion coefficients, and refrains from the detachment at the interface between the scale and the matrix during cooling process [17].

5.4 Summary

The influence of Al content on the high-temperature oxidation behavior of the Co-based superalloys has been characterized through researching the isothermal oxidation of the novel Co-20Cr-(5, 10)Al (wt.%) ODS superalloys at 900 ºC and 1000 ºC in air. In addition, the effect of Cr and Y_2O_3 on the oxidation behavior of Co-20Cr-10Al (wt.%) ODS superalloys also has been investigated. The results of this study are summarized as follows:

(1) Effect of Al content. Even though the alloy is ODS with small substrate grain size which can enhance outward Al diffusion, 5Al (wt. %) is not sufficient to form Al_2O_3. The 10AlCrY specimen possesses a better oxidation resistance with the formation of a single alumina scale than the 5AlCrY specimen with a duplex scale of outer $CoCr_2O_4/Cr_2O_3$ and inner Al_2O_3. A faster θ- to α-alumina transformation at higher temperature is responsible for the smaller weight gain at 1000 ºC than at 900 ºC for the 10AlCrY specimens oxidized in 225 h, i.e., θ- and α-alumina coexist at 900 ºC whilst α-alumina dominates at 1000 ºC. Since the confirmation that the θ-alumina grows with cation outward diffusion and the α-alumina forms with oxygen inward diffusion, the alumina scale growth of 10AlCrY is determined by bilateral diffusion of cation outward and oxygen inward at 900 ºC and by oxygen grain boundary transport at 1000 °C.

(2) Effect of Cr-addition. The addition of Cr into Co-based ODS superalloys has proven to effectively improve high-temperature oxidation resistance by accelerating the formation of an exclusive alumina scale instead of the multilayered scale with an external $CoO/CoAl_2O_4$ and an inner Al_2O_3.

(3) Effect of Y_2O_3-addition. With the doping of yttria, the alumina scale has been perfected obviously with the dispersed Y-Hf oxide particles, even though a slight weight gain would be accelerated due to the decreased alumina grains size. The presence of oxide particles inside alumina-scale could significantly maintain a superior spalling resistance.

Chapter 6 Tensile properties

6.1 Experimental details

Tensile properties of the novel Co-20Cr-(5, 10)Al-2.4Hf-1.5Y_2O_3 (wt. %) oxide dispersion strengthened (ODS) superalloy were illustrated through a comparing investigation with Co-20Cr-5Al (wt. %) (5AlCr) alloy. Both the Co-based alloys (with and without ODS participation) were fabricated by mechanical alloying (MA), spark plasma sintering (SPS), hot rolling and the final annealing at 1200 ºC.

The crystalline structure of each consolidated bulk were detected using X-ray diffraction (XRD, Philips X' Pert PRO). The metallographic analysis was carried out using backscattered electron microscopy (BSE) equipped in electron probe micro-analyzer (EPMA, JEOL JXA-8530F). The grain size and phase constituent were observed by Electron Back-Scattered Diffraction (EBSD) jointed in a scanning electron microscope (SEM, Carl Zeiss Cross Beam 1540 EsB), the elements distribution in each phase was analyzed with elemental mapping in electron probe micro-analyzer (EPMA, JEOL JXA-8530F). The distribution of nano-sized oxide particles in each phase was analyzed using transmission electron microscopy (TEM, JEM-2010 and FEI Titan3 G2 60-300), in which the TEM specimens were prepared by Focused Ion Beam Milling and FE-SEM Imaging (FIB-SEM, JEOL JIB-4600F/HKD). The tensile test was carried out at 23 ^{o}C, 250 ^{o}C, 500 ^{o}C, 700 ^{o}C and 1000 ^{o}C with a strain rate of 1×10^{-3} s^{-1} under argon gas atmosphere to prevent a surface oxidization. The size of the samples for tensile tests is 5 mm in gauge length, 1.2 mm in width and 0.5 mm in thickness.

6.2 Results

6.2.1 Microstructural characterization

Based on a Co-Cr-Al ternary phase diagram (**Fig. 6.1**) computed with the thermodynamic software Pandat [69], the Co-20Cr-(5, 10) (wt.%) Al alloys are mainly composed of two different phases at 1100 ^{o}C; the Co solid solution of fcc structure, and the CoAl phase of B2 structure. In contrast with an almost equal volume fraction of B2 and fcc phase in the samples with 10Al (wt.%) addition, the fcc

phase is dominant in the 5Al (wt.%) samples.

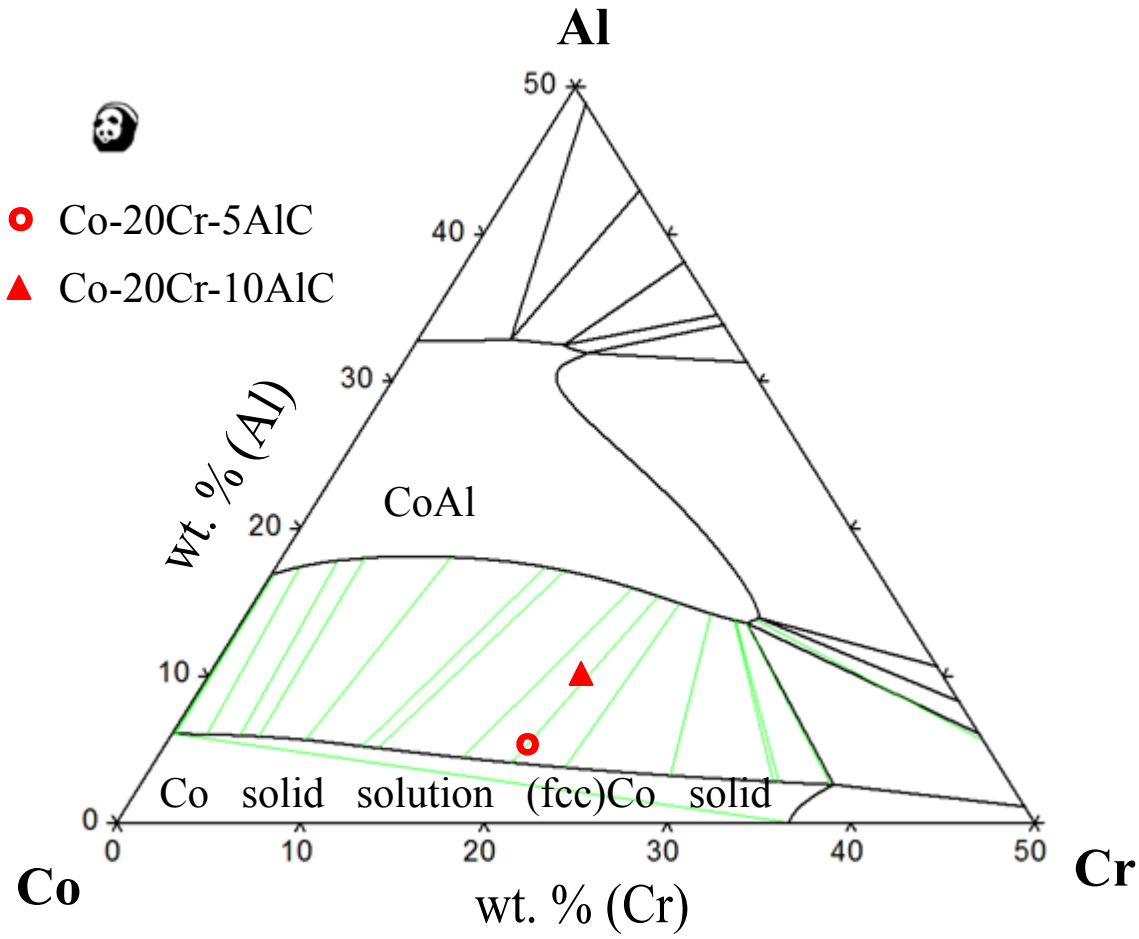

Fig. 6.1 The ternary Co-Cr-Al phase diagram calculated with Pandat software at 1100 ^{o}C.

Fig. 6.2 shows the X-ray diffraction pattern of the Co-based alloys after final annealing at 1200 ^{o}C for 1 h. In contrast with a noticeable hcp structure in cobalt at room temperature, fcc phase predominates in the alloys with 5Al (wt.%) addition and only very faint hcp diffraction peak can be observed, also no obvious hcp peaks could be detected in 10Al (wt.%), which means that the phase transformation of fcc-hcp has been suppressed during cooling process. In addition, the volume fractions of fcc and B2 phase in all the samples are quite fit with the phase diagram (**Fig. 6.1**) even though at room temperature, i.e., the Co-fcc predominates the 5Al alloys (5AlCrY and 5AlCr) as well as the Co-fcc and CoAl-B2 jointly govern the 10AlCrY sample.

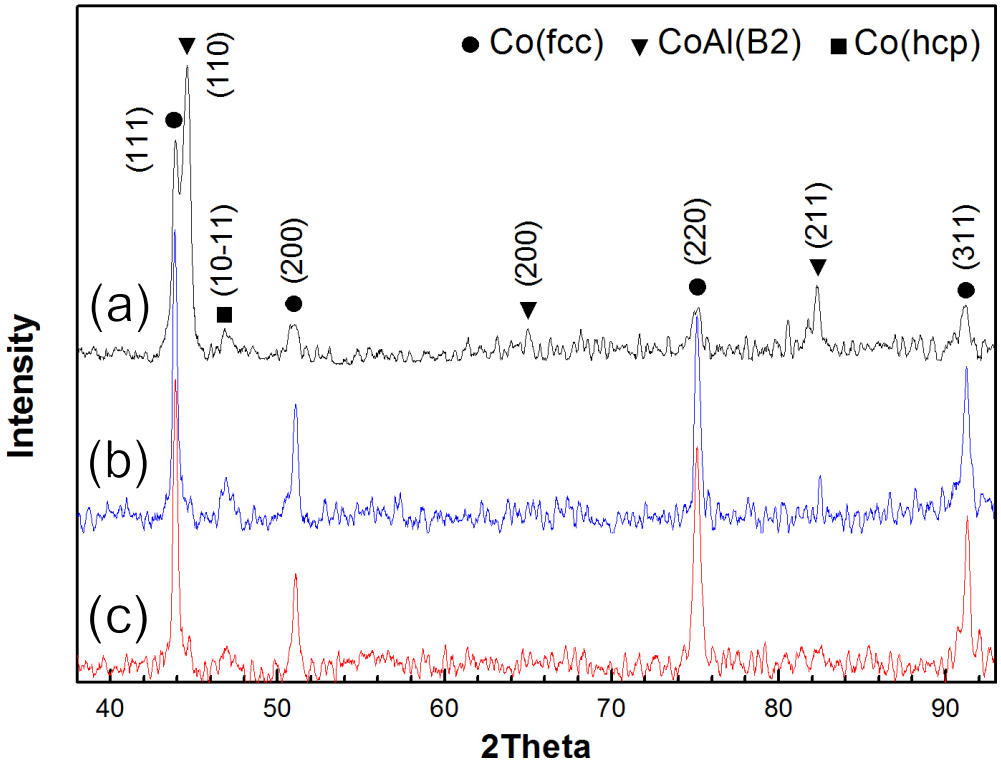

Fig. 6.2 XRD results for the 10AlCrY (a), 5AlCrY (b) and 5AlCr (c) after annealing 1 h at 1200 ^{o}C.

Fig. 6.3 shows the BSE images of the metallographic analysis. Due to high aluminum content in the B2 phase, i.e., nearly triple than that in the fcc phase, it's evident to distinguish the B2 and fcc phase through the image contrast at the BSE mode. Both the two samples basically consist of two regions; i.e. the dark region with 0.2-0.4 μm scale and the light grey matrix. My previous work [68] has proved that the dark region is CoAl phase with B2 structure and the grey matrix is cobalt solid solution with fcc structure, as shown with the inserted diffraction patterns. With the increasing of Al, a larger area of dark regions could be found in the sample of 10AlCrY. The distribution of those dark and grey areas in the 5Al and 10Al samples is consistent with the volume fraction of the B2 and fcc in the XRD results.

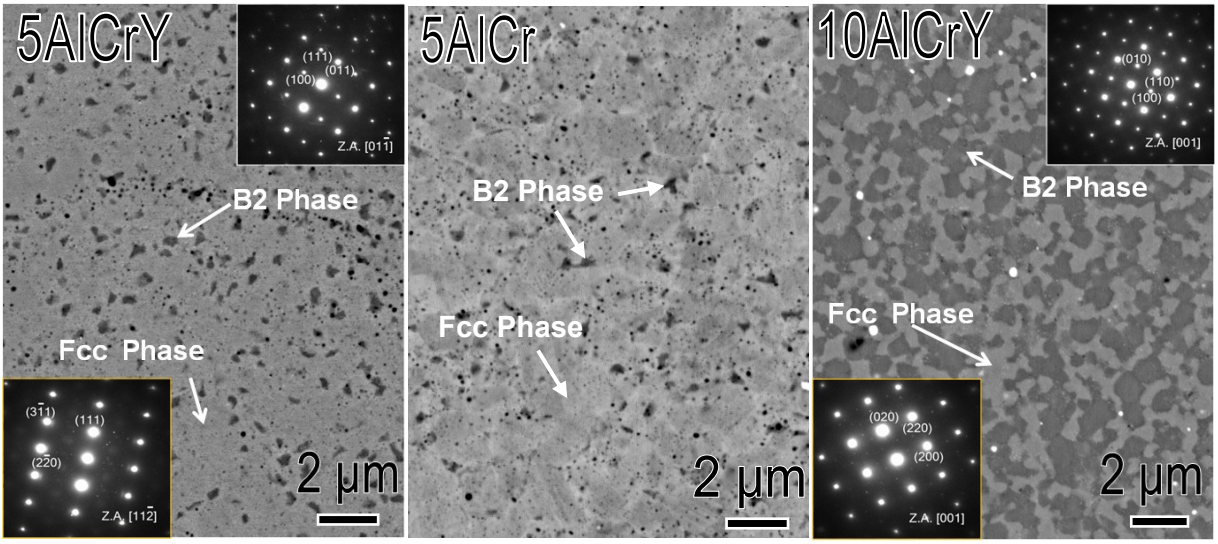

Fig. 6.3 SEM images of backscattered electron obtained from the 5AlCrY, 5AlCr and 10AlCrY samples.

Besides, all the three specimens were analyzed using EBSD, the image quality (IQ) maps and corresponding Orientation imaging microscopy (OIM)-inverse pole figures (IPF) are presented in **Fig. 6.4**, in which the OIM-IPF maps of B2 and fcc phase also have been listed respectively. Based on the IQ maps of **Fig. 6.4**, the average grain size of the 500 nm in the 5AlCrY and the 800 nm in the 10AlCrY could be confirmed. Besides, the 5AlCr alloy without ODS participation shows a coarse grain size with 1.2 μm.

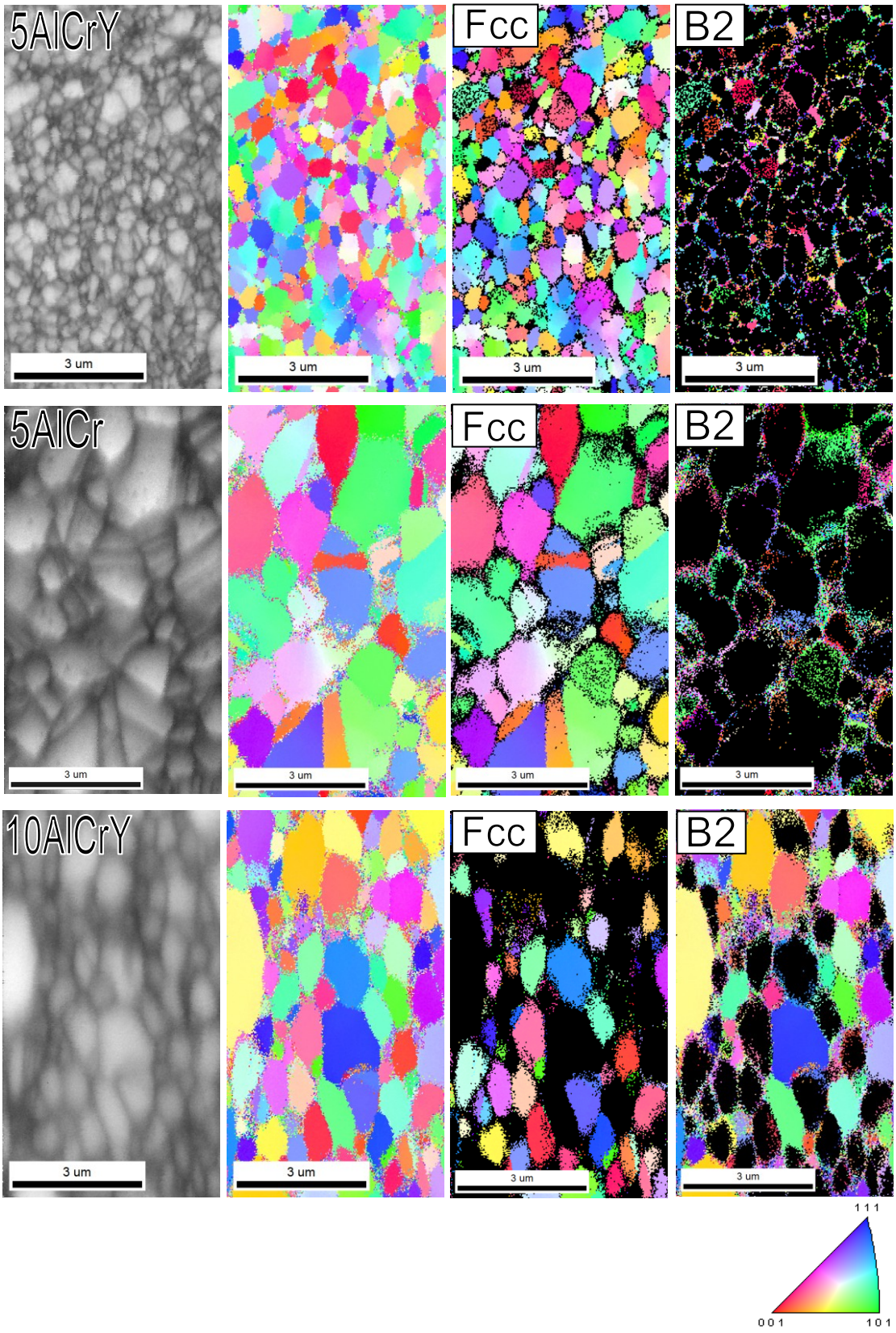

Fig. 6.4 IQ maps and corresponding OIM-IPF maps obtained from the 5AlCrY, 5AlCr and 10AlCrY samples, the fcc and B2 phase are separated with OIM-IPF maps.

6.2.2 Oxide particle characterization

Fig. 6.5 (a) and (b) show the HAADF-STEM images and the corresponding EDS maps of all the chemical composition in the 5AlCrY alloy. Due to a high Al concentration in the B2 phase than that in the fcc phase, the dark area in the HAADF image of the **Fig. 6.5** (a) is easily determined to be the B2 phase, in which Al is much higher than the matrix according to the corresponding aluminum elemental maps. It's obvious that the nanoscale oxide particles are sparser and coarser in the B2 phase (dark area) but denser and smaller in the fcc phase (matrix). Based on the image contrast in the HAADF image of the **Fig. 6.5** (a), the particles dispersed inside the B2 phase seems to be composed of three kinds, i.e., coarse white particles, coarse black particle and joint particle with white and dark parts, which are marked with the arrows of yellow, red and green, respectively. According to the elemental maps of the oxide particles in **Fig. 6.5** (a), it is clear that the white particles are enriched with Y, Hf and O as well as the coarse black particle is enriched with Al and O. Therefore, the coarse white particles are thought to be Y-Hf-rich oxides and the coarse black one is Al_2O_3, the white part in the joint particle is the Y-Hf particle, which is adjacent to the Al_2O_3 with black contrast. The three kinds of particles exist in the fcc matrix, as well, as shown in the **Fig. 6.5** (b), but in which the particles are much denser and smaller than that in B2 phase, especially the Y-Hf particles.

The particles distributed in the 10AlCrY alloy also have been exhibited with the HAADF-STEM images and the corresponding elemental maps, as shown in the **Fig. 6.6**, in which the **Fig. 6.6** (a) and (b) represent the B2 and fcc phase, respectively. Based on the elemental maps, the nanoscale particles in both the B2 and fcc phases are enriched with the elementals of Y, Hf, Al and O, as well. Besides, the particles in fcc phase is smaller and denser than that in the B2 phase, similar with the particles distribution of the two phases in the 5AlCrY alloy. The coalescence of Hf with a high vacancy in the B2 phase has been verified to responsible for the coarsening of those Y-Hf oxides with a core-shell structure of $Y_2Hf_7O_{17}$ type [23, 68]. Besides, the coarsening of the Y-Hf oxide particle joint to Al_2O_3 particle is thought to results from the rapid diffusion of yttrium and hafnium atoms through the Al_2O_3 particle/matrix

interface [68]. EPMA elemental mapping with a high magnification has been conducted to further investigate the distribution density of the oxide particles in the B2 and fcc phase, as shown in **Fig. 6.7**. Since the Y-Hf oxide is the primary dispersoid in the Co-based ODS superallous, it's noticeable to confirm that the fcc phase possesses more particles than the B2 phase through the elemental mappings of O, Y and Hf.

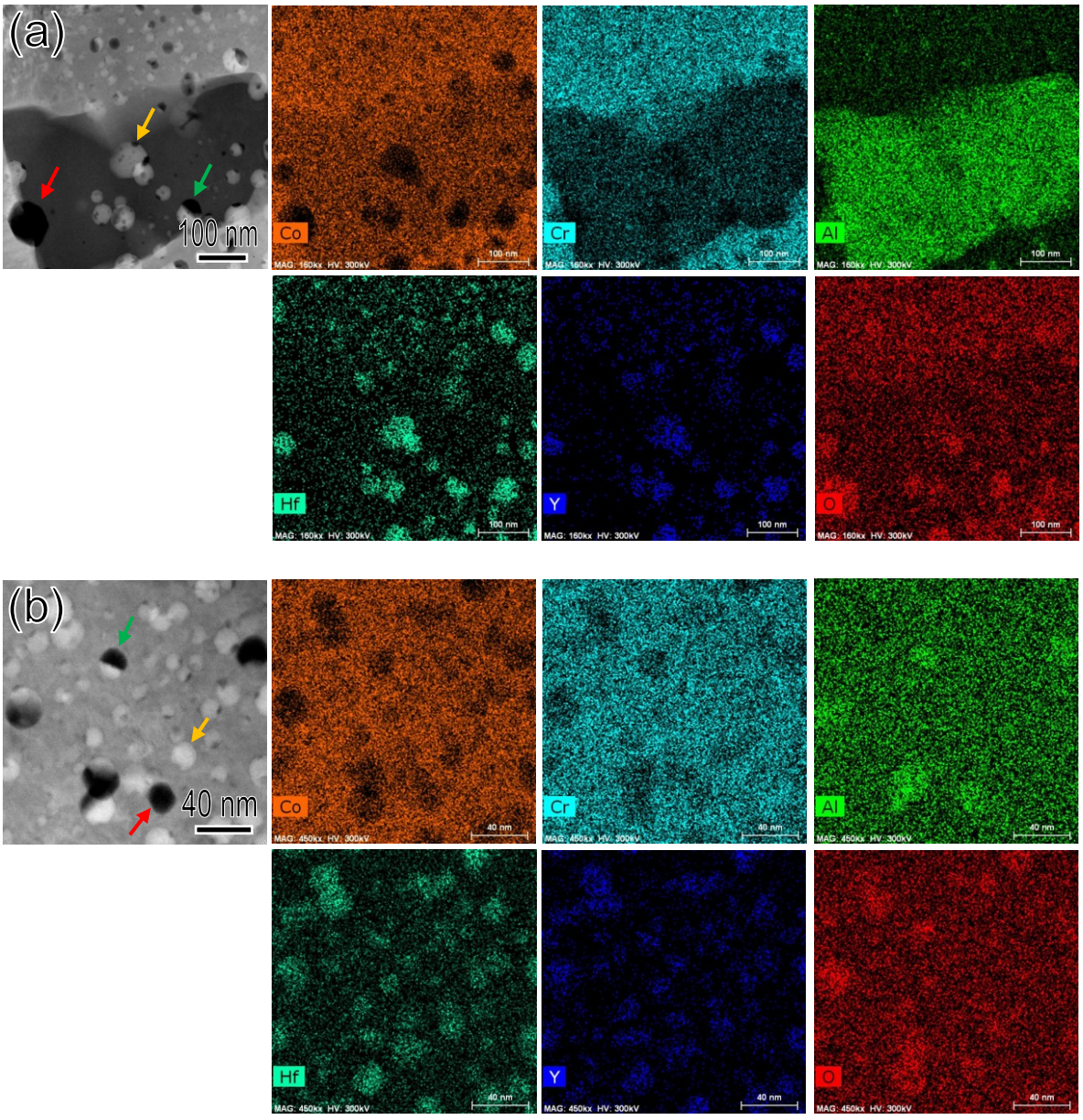

Fig. 6.5 HAADF-STEM images of nanoscale particles in the 5AlCrY alloy and corresponding EDS elemental maps of Co, Cr, Al, Hf, Y and O, in which (a) and (b) are obtained from the B2 and the fcc phase, respectively.

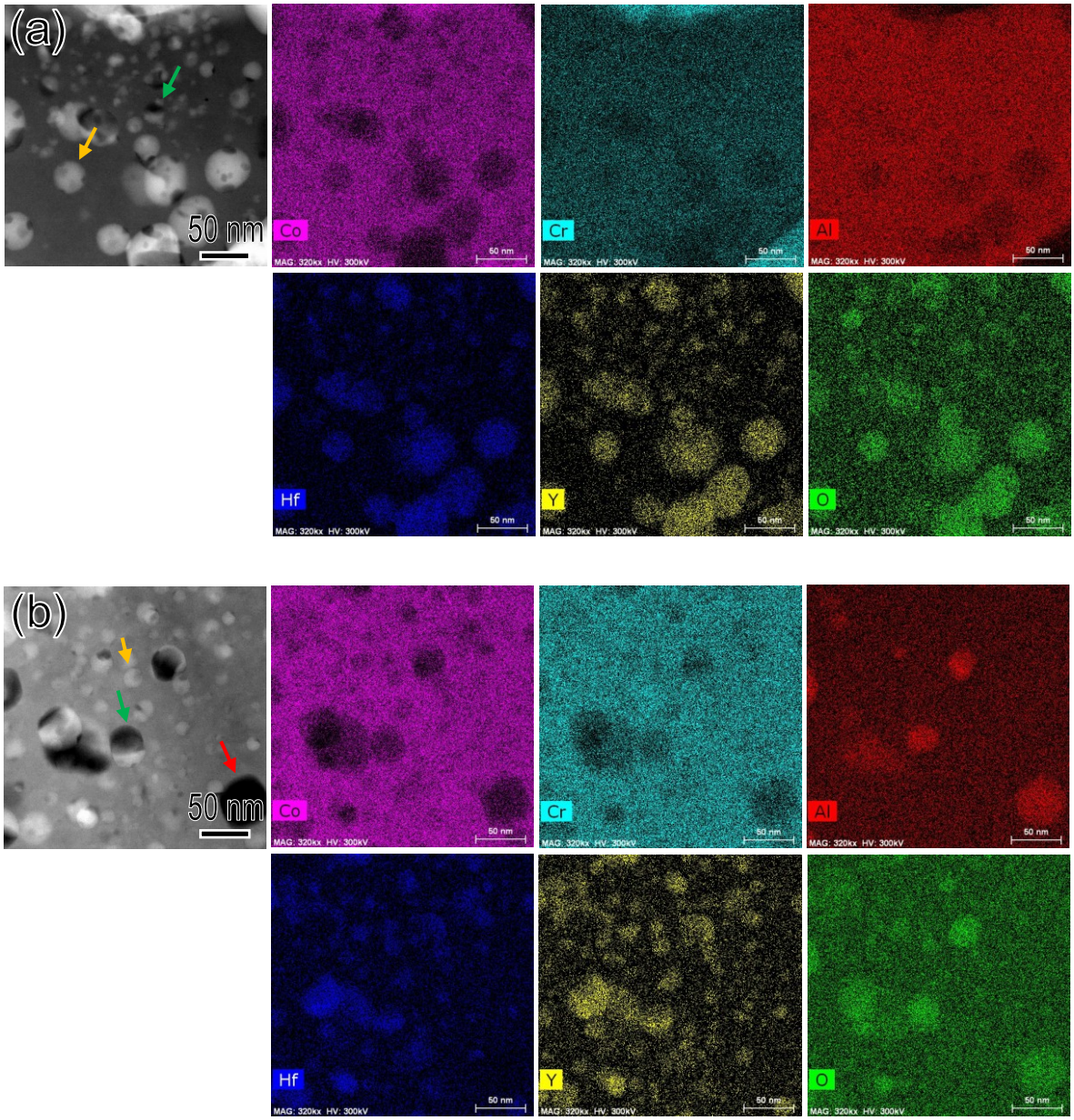

Fig. 6.6 HAADF-STEM images of nanoscale particles in the 10AlCrY alloy and corresponding EDS elemental maps of Co, Cr, Al, Hf, Y and O, in which (a) and (b) are obtained from the B2 and the fcc phase, respectively.

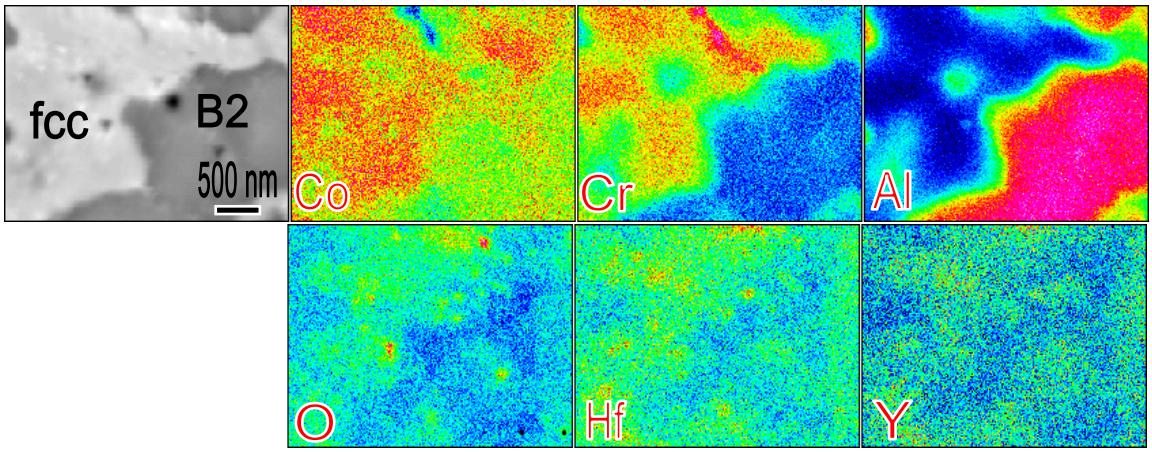

Fig. 6.7 Distribution of Y-Hf oxides in the fcc and B2 phase of the 10AlCrY samples obtained via high magnification EPMA element mappings.

6.2.3 Tensile properties

The ultimate tensile strength (UTS) of the 5AlCrY and 10AlCrY ODS superalloys at the temperatures from 23 ^{o}C to 1000 ^{o}C are presented in the **Fig. 6.8**, in which the results of conventional Co-based alloys (L605) is also inserted to highlight the difference. In contrast to the 10AlCrY alloy which shows comparable UTS with the conventional L605 alloy, the 5Al exhibits much higher tensile strengths and especially outstanding UTS at low temperatures.

The detailed engineering stress-strain curves at 23 ^{o}C and 700 ^{o}C are shown in **Fig. 6.9**. Both the samples with 5Al (wt. %) addition exhibited high UTS at room temperature, i.e., 2.85 GPa in the 5AlCrY and 1.73 GPa in the 5AlCr alloy with free ODS. However, the 10AlCrY sample shows relatively low UTS and extremely small elongation at room temperature. With the increasing of temperature to 700 ^{o}C, both the 5AlCrY and 10AlCrY presented a decreased UTS as well as a gradually increased elongation.

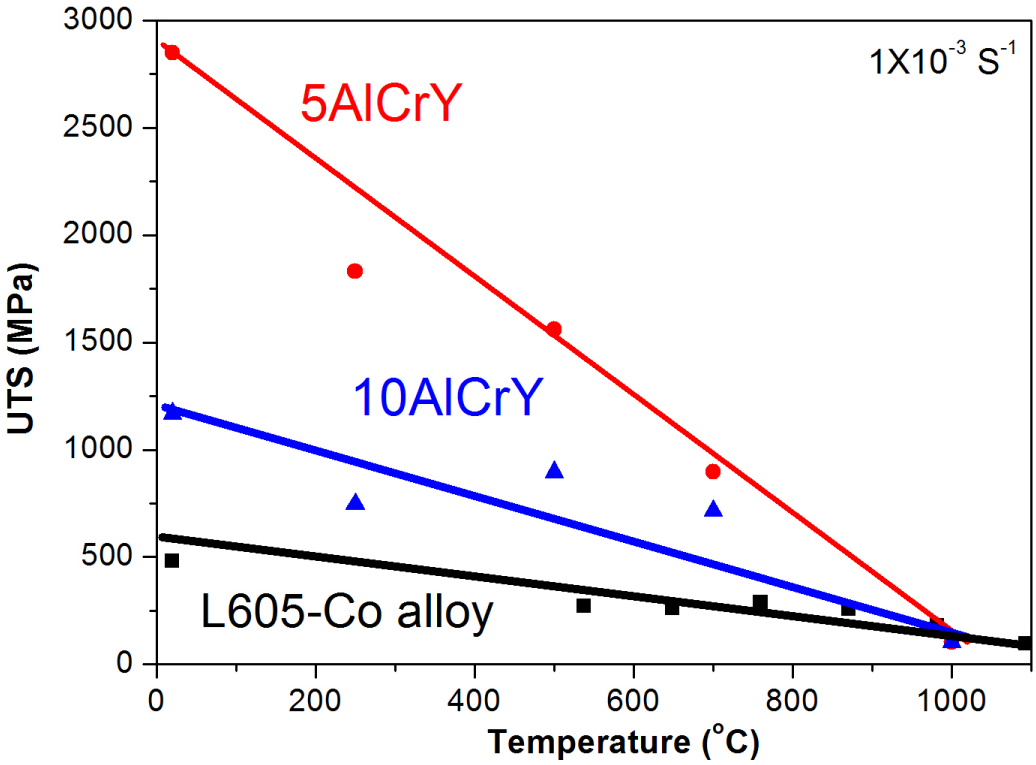

Fig. 6.8 Ultimate tensile strength (UTS) as a function of temperature for the 5AlCrY / 10AlCrY superalloys and conventional L605 Co-based alloys.

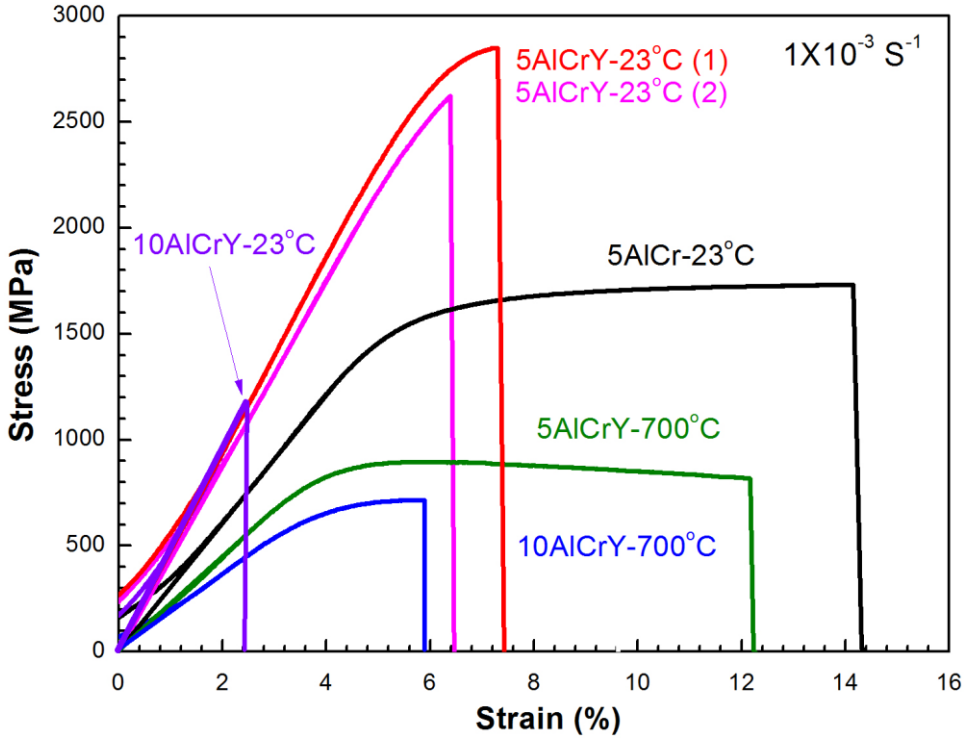

Fig. 6.9 Engineering stress-strain curves of the 5AlCrY, 5AlCr and 10AlCrY at the temperatures of 23 ^{o}C and 700 ^{o}C.

The tensile fractured samples were observed from the normal surface and the cross-section, which is parallel and vertical to the tensile axis, respectively. **Fig. 6.10** shows the fractography of 5AlCrY and 10AlCrY after the tensile testing at 23 ^{o}C. In the magnified image of **Fig. 6.10 (a)**, dimple structure was observed and dominated the fractured cross-section, which means a plastic deformation happened in the fcc matrix. In addition, several spherical holes were found, as shown with the dotted circle in the **Fig. 6.10 (a)**, which was supposed to be derived from the spallation of B2 phase during the tensile test. In the cross-sections of the 10AlCrY, in addition to a small quantity of the dimples, amounts of flat areas were observed, as shown with the dotted circle in the **Fig. 6.10 (b)**, resulting from the brittle deformation of B2 phase.

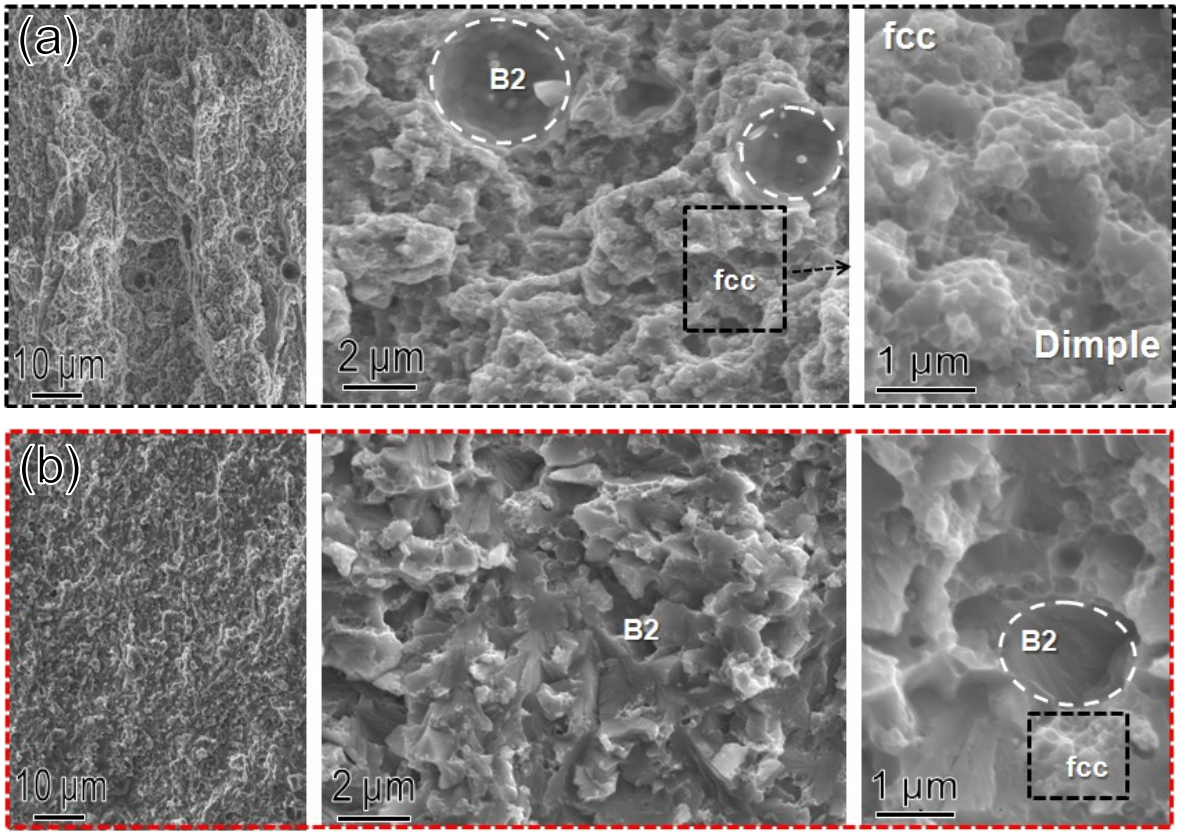

Fig. 6.10 Fractured cross-sections of the 5AlCrY (a) and the 10AlCrY (b) alloys at room temperature.

Fig. 6.11 shows the normal surfaces of the fractured 5AlCrY and 10AlCrY samples at 23 ^{o}C and 700 ^{o}C. It's obvious that the fractured surfaces are tidy at 23 ^{o}C and then change to be rugged at 700 ^{o}C. Usually, the tidy fracture is one of typical

transgranular fracture with high brittleness as well as the rugged fracture means intergranular fracture with high ductility. It means that the fracture mechanism changes from the brittle fracture to ductile fracture with the temperature increasing, which is consistent with the growth of elongation at elevated temperature. However, the occurrence of this rugged fracture is much earlier in the 5AlCrY than that in the 10AlCrY alloy, and an obvious tidy fracture even could be found in the 10AlCrY at 700 ^{o}C. Hence, it was determined that the 10AlCrY is mainly dominated by brittle fracture and results in relatively low UTS during the whole tensile testing. In addition, as shown in the **Fig. 6.8**, even a decrease in the UTS happened with the increasing of temperature, the 10Al possesses a slow decreasing rate of UTS than 5Al alloy, which is attributed to the gradual recovery of plasticity for the 10Al at elevated temperature. In addition, amounts of cracks were observed at the surface after the deformation at 700 ^{o}C, as shown with the magnified image at the bottom left of the **Fig. 6.11**.

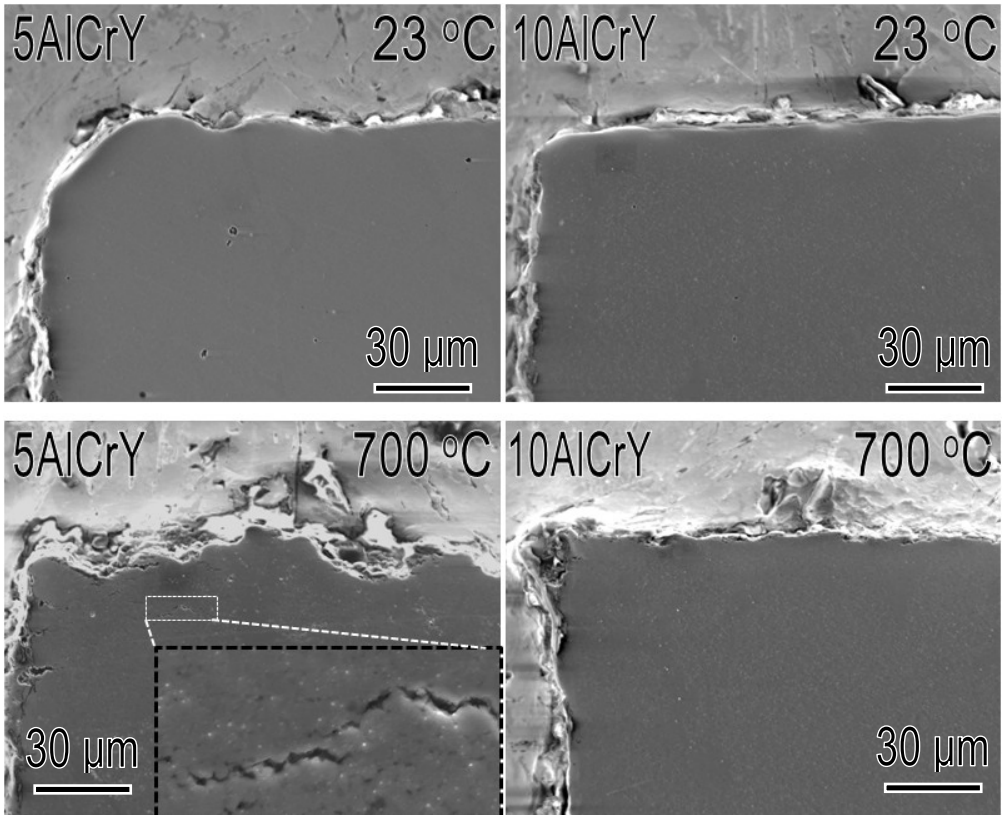

Fig. 6.11 Fractured surfaces of the 5AlCrY and the 10AlCrY alloys at 23 ^{o}C, 700 ^{o}C.

6.3 Discussion

In respect of conventional Co-based alloys, the fcc-to-hcp allotropic transformation proceeds spontaneously during cooling from about 426 ^{o}C down to 330 ^{o}C and results in a stable hcp (ε) phase at room temperature, which is known as fcc/hcp martensitic transformation [96]. As shown in **Fig. 6.12**, the composition of Co-20Cr-5Al/10Al (wt. %) should be dominated by hcp phase based on the ternary phase diagram.

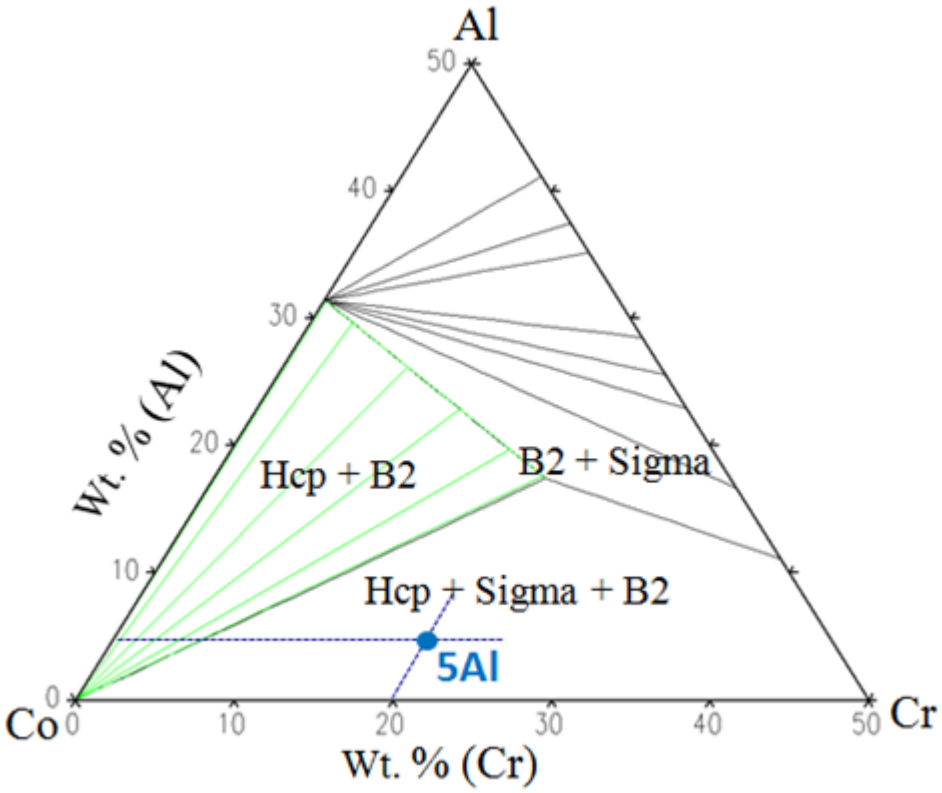

Fig. 6.12 The ternary Co-Cr-Al phase diagram calculated with Pandat software at 23 ^{o}C.

However, no obvious hcp diffraction peaks could be observed in both the 5AlCrY and the 5AlCr samples at room temperature from the XRD diffraction patterns (**Fig. 6.2**), which means that the phase transformation of fcc-hcp has been suppressed during cooling process. Alloying elements play a significant effect on the volume fraction of the ε martensite phase (V_m). However, although a high 20Cr (wt. %) was introduced in the present Co-based system, K. Ando, et al. [97] claimed that the addition of Cr could only slightly decreased the V_m in Co-Al alloys. Thus, the

low V_m in the Co-based alloys at room temperature should not be attributed by the addition of Cr.

P. Huang, et al. [98, 99] reported that the V_m is strongly influenced by the grain size in the Co-Cr-Mo alloy, and the V_m is relatively low in fine grained alloys but concomitantly increases with increasing grain sizes [98]. In the case of the ultrafine grains of the 500 nm in the 5AlCrY, 800 nm in the 10AlCrY and the 1.2 μm in the 5AlCr alloys, an extremely small V_m could be obtained if substituting the grain sizes to the function proposed by P. Huang, et al., as shown in **Fig. 6.13.**

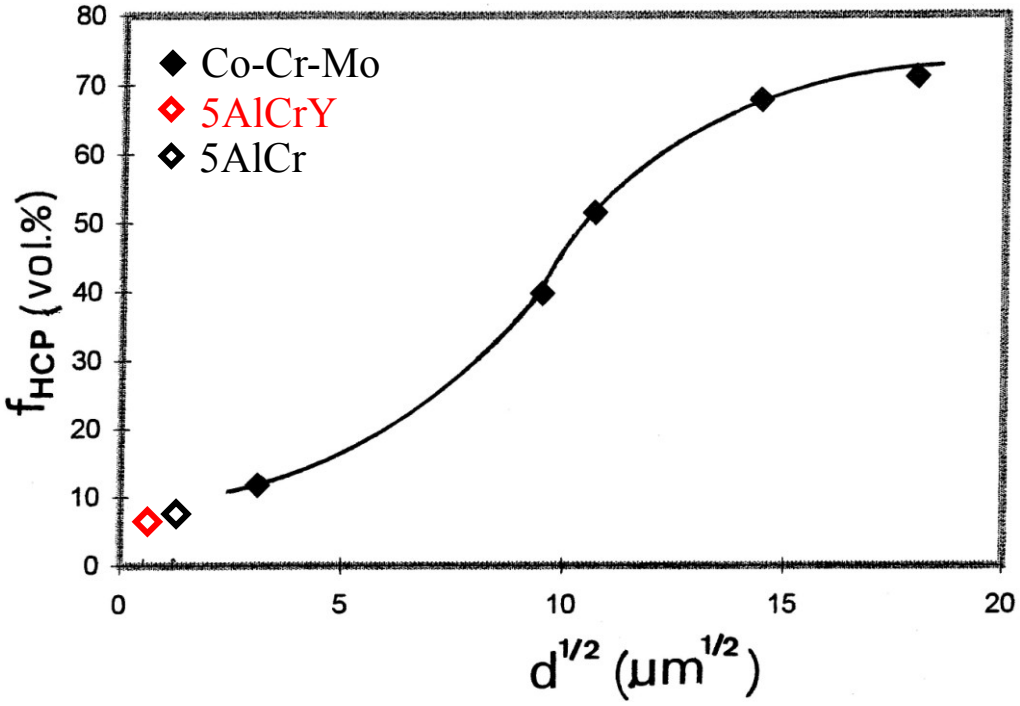

Fig. 6.13 Volume fraction of athermal ε-phase as a function of grain size.

The critical activation energy (ΔG) for fcc-to-hcp martensitic transformation can be expressed as [100]:

$$\Delta G = \frac{K}{(\Delta g + \Delta G_{Int})^4} \quad (6.1)$$

where K is a constant connected with the elastic and interfacial energy between the martensitic and initial phases, Δg is the chemical driving force for martensitic

transformation, and ΔG_{Int} is excess energy because of the Gibbs-Thomson effect [101],

$$\Delta G_{Int} = 2\gamma V_m/R \quad (6.2)$$

In which the γ is the interface energy; V_m is the molar volume; and R is the grain radius. It's obvious that the ΔG_{Int} would increase with the refining of grain size [102], since the decreasing of grain size results in an increase of the volume of interfaces. Since a negative value of Δg for the fcc-to-hcp transformation in Cobalt, i.e., -16 J/mol [103], the total critical activation energy would be increased with the increasing of ΔG_{Int} in Co-based alloys. It has been reported that for cobalt with an average grain size of 10 μm the ΔG for martensitic transformation is 5 times higher than it is for conventional coarse-grained cobalt [104]. Therefore, a much higher ΔG induced by the ultrafine grain in the Co-based alloys is supposed to be responsible for the stable fcc structure at room temperature. The processes that lead to the formation of nano-crystalline structures during ball-milling have been claimed in amounts of reports [105, 106], which is attributed to the high deformation rates in the MA process. Besides, grain boundaries and phase boundaries are decorated with a large number of oxide particles in the 5AlCrY and 10AlCrY alloys [68], the grain coarsening during sintering and annealing process could be suppressed by the oxides pinning effect in ODS superalloys [13, 107], which results in a smaller grain and more faint hcp peak in the 5AlCrY than that in the 5AlCr alloy, as shown in the **Fig. 6.4** and **Fig. 6.2,** respectively.

Another point should be noted is that the extremely high strength of the 5AlCrY at room temperature, which is much higher than other conventional superalloys. As described in **Fig. 6.5**, the 5AlCrY is dominated by fcc phase and in which a large number of fine Y-Hf particles are distributed. According to the TEM observation on the 5AlCrY sample after tensile test at room temperature, as shown in **Fig. 6.14**, dislocation motion was found to be restrained by the pinning of fine dispersoids. Therefore, a strong ODS effect could be confirmed in the 5AlCrY superalloy.

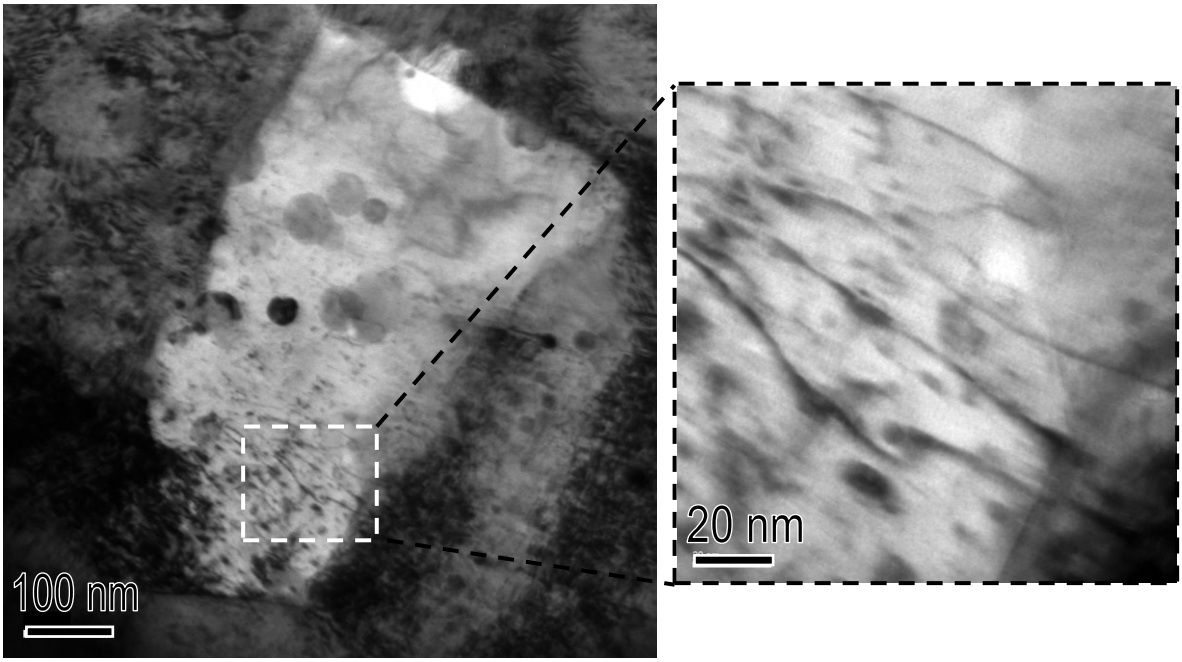

Fig. 6.14 TEM images of the 5AlCoY superalloy after tensile test at room temperature.

Based on the following equations proposed by Scattergood and Bacon [42], the ODS effect could be quantitatively measured.

$$\sigma_{th} = \mathrm{A}\frac{M}{2\pi}\frac{\mathrm{Gb}}{\lambda}\left(\ln\frac{\mathrm{D}}{\mathrm{r_0}} + \mathrm{B}\right) \tag{6.3}$$

$$\lambda = 1.25\ell_{\mathrm{s}} - 2\mathrm{r_s} \tag{6.4}$$

$$\ell_s = \sqrt{\frac{2\pi\overline{\mathrm{r}^3}}{3f\bar{r}}} \tag{6.5}$$

$$\mathrm{r_s} = \frac{\pi\overline{r^2}}{4\bar{r}} \tag{6.6}$$

In which the σ_{th} is the threshold stress and corresponds to the oxide particle-hardening stress; the λ is average face-to-face distance between two particles; M is the Taylor factor (3.06); G is the shear modulus and equals to 75 GPa at room temperature; b is the magnitude of the Burgers vector (2.48×10^{-10} m); A and B are constants and are taken as 1.06 and 0.65, respectively; r_0 is the inner cut-off

radius of a dislocation core (b-3b); D is harmonic mean of λ and $2r_s$; r_s is the average particles radius: 8 nm in fcc phase and 11 nm in B2 phase; ℓ_s is the average center to center distance; f is the volume fraction of the dispersed particles: 0.0217 in the fcc phase and 0.0257 in the B2 phase. Above distribution of the oxide particles in fcc phase and B2 phase was derived by analyzing TEM images and the detailed results are exhibited in **Fig. 6.15**.

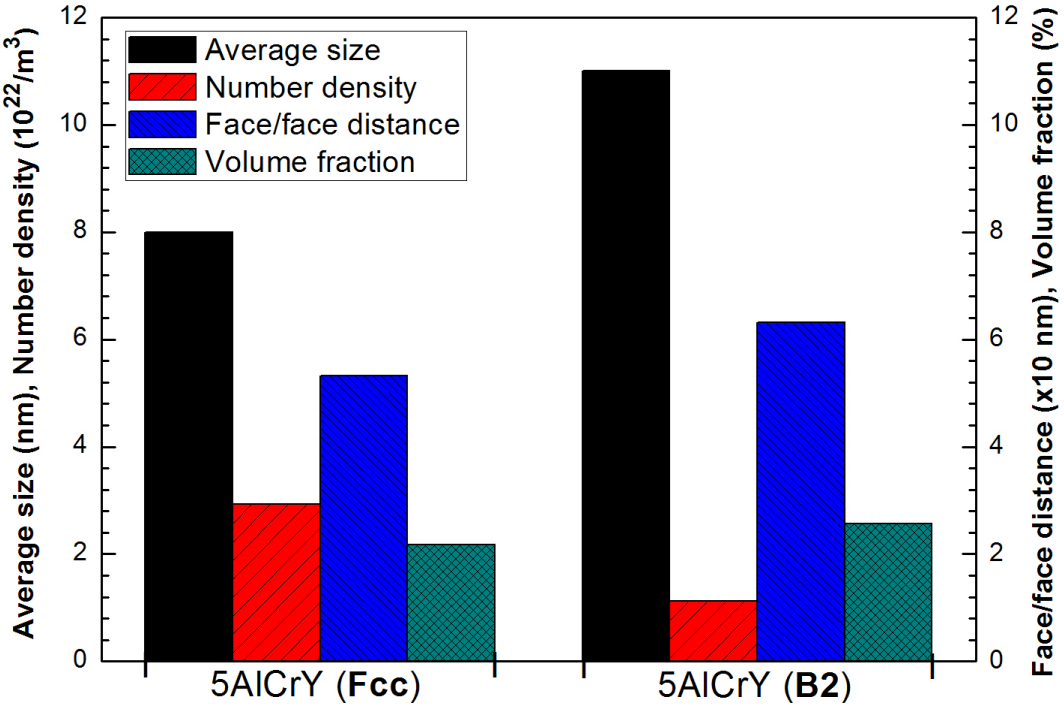

Fig. 6.15 Oxide particles distribution of the fcc and B2 phase on the 5AlCrY superalloy.

The calculation for σ_{th} is 628.8 MPa in the B2 phase as well as 711.1 MPa in the fcc phase. According to the report [68] that volume fraction of the fcc and the B2 phase in the 5AlCoY sample is close to 90 % and 10 %, respectively, the oxide particle dispersion strengthening in the 5AlCoY superalloy was approximated to be 702.9 MPa at room temperature. Strength increment in 5AlCoY from non ODS 5AlCo reaches approximately 1 GPa from **Fig. 6.9**. In 5AlCoY, therefore, the other effect such as grain boundary strengthening could work effectively at room temperature, because 5AlCoY contains finer grain size than 5AlCo.

In order to further investigate the strengthening mechanism, the fractured 5AlCrY

alloy after tensile testing at room temperature was analyzed with more TEM work. Based on the bright field (BF) TEM images (**Fig. 6.16**), amounts of parallel strips with an ultrafine width were found. Furthermore, the selected area diffraction (SAD) pattern of each strip marked with dotted circle has been performed and their results are presented. Based on the SAD patterns, the region 1 was confirmed to be fcc phase, and the area 2 was proved to be the fcc phase, as well.

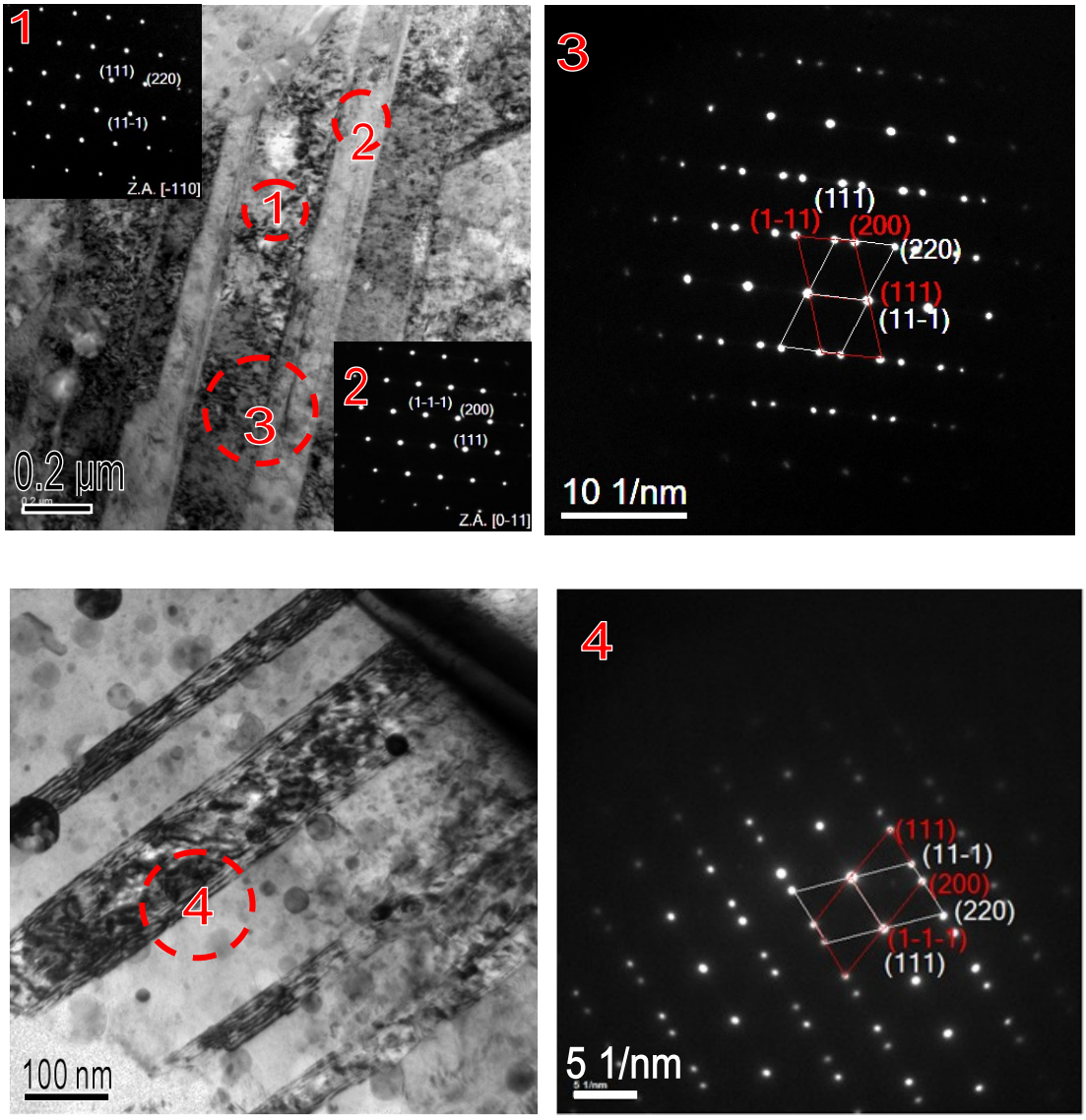

Fig. 6.16 TEM images and corresponding selected area diffraction (SAD) patterns of nano-twins in the 5AlCrY alloy after tensile test at room temperature.

After broadening the range of selected area, a typical fcc twin structure was observed, as shown with the SAD pattern of 3. Therefore, it's confirmed that the

twinning deformation happened during the tensile test at room temperature. Besides, with a high magnification TEM image, as shown with the bottom BF TEM image in **Fig. 6.16**, a large number of oxide particles are decorated inside the nano-twins.

The TEM observation also has been performed for the 5Al No ODS sample after the tensile test at 23 ^{o}C, as shown in the **Fig. 6.17**, in which an obvious twinning deformation could be observed.

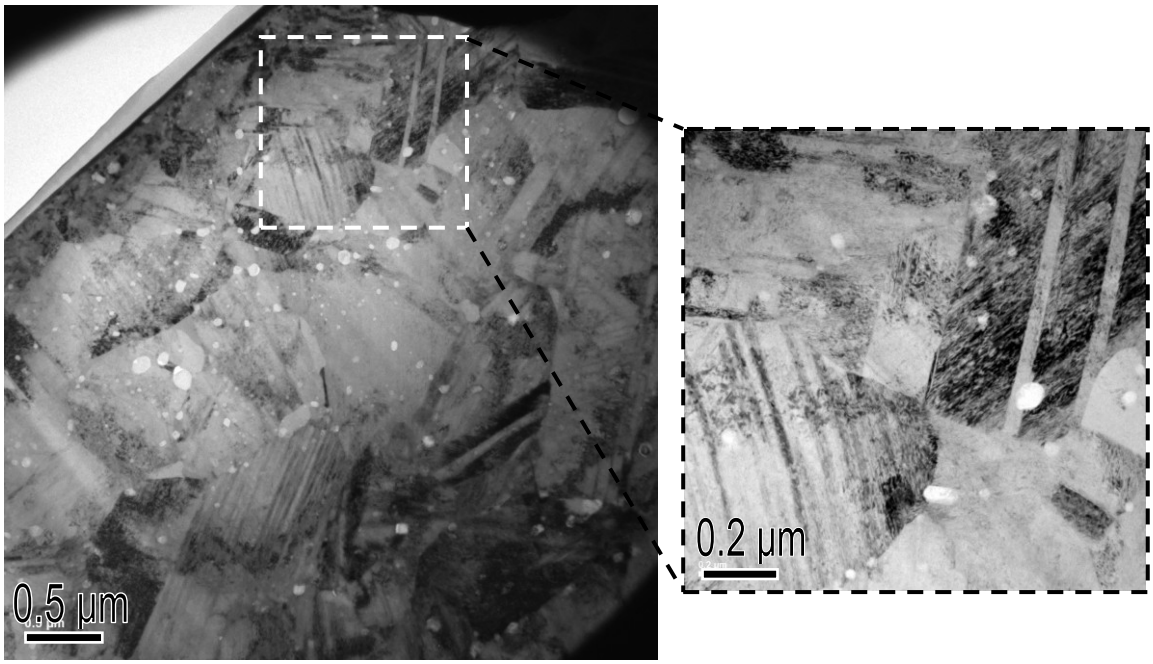

Fig. 6.17 TEM images of deformation twins in the 5AlCr alloy after tensile test at room temperature.

Thus, the twinning formation during tensile test could be confirmed for the two Co-based alloys. It has been verified that metals and alloys with low stacking faults energy (SFE) readily deform via twinning [108, 109]. In respect of other metals which possess a relatively high SFE values, the twinning also could be usually observed through decreasing the grain size, such as Cu and Ni [110, 111]. It has been reported that the twinning is one of the typical deformation mode for the γ-cobalt (fcc), which possesses a low stacking fault energy and facilitates twinning deformation during strain, especially for the ball-milled nanocrystaline cobalt [112, 113].

Twinning may play a crucial role in enhancing the work-hardening rate since the fact that twin boundaries act as strong barriers to dislocation slipping [113, 114]. The interaction between twin and dislocation could be schematically exhibited with **Fig. 6.18.**

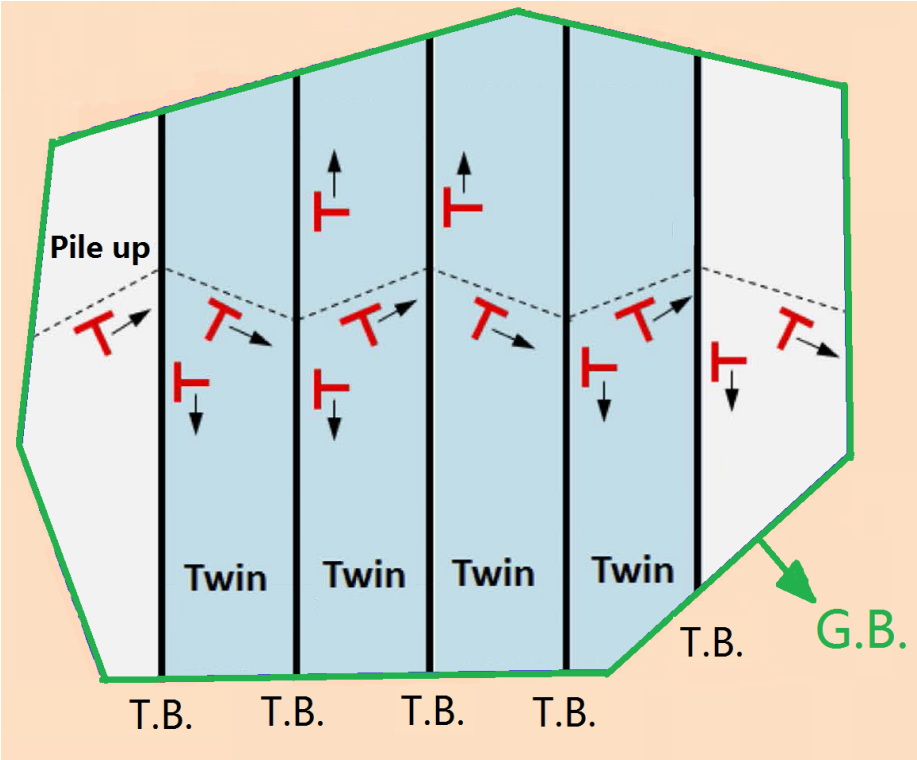

Fig. 6.18 Schematic illustration for the interaction between twin boundary (T.B.) and dislocation motion.

Since the twin boundary works as like grain boundaries to block the motion of dislocation, the well-known Hall-Petch strengthening model was considered to be used to quantify the relation between the mechanical strength and deformation twins. Gray et al.[115] also proposed that the deformation twinning could improve the strain-hardening rate via Hall–Petch type hardening mechanism, since the twinning divided grains and decreased the effective slip distance. The strength of deformation twins has been calculated and the results were found to match quantitatively with the Hall-Petch grain size strengthening by Salem et al.[116].

The well-known Hall-Petch strengthening model could be expressed as follow [117-119],

$$\sigma_y = \sigma_0 + kd^{-1/2} \quad (6.7)$$

where σ_y is the yield strength, σ_0 is the friction stress, *k* is the Hall-Petch slope, d is the grain size. Due to a limited research in the Co-20Cr-Al (wt %) system, no detailed values of σ_0 and *k* can be accessed for the Co-based alloys. In order to derive those values, we cite the σ_0 and *k* in the Ni-20Cr (wt %) (Small addition of Al) system, since both the two systems are fcc structure and the Ni possesses a close atom size with Co. Namely, the σ_0 and *k* in the Co-20Cr-5Al (wt %) alloys are approximately equal to 254 ± 0.01 MPa and 622 ± 0.02 MPa · $\mu m^{1/2}$, respectively [120]. Since the matrix of the 5AlCrY and 5AlCr samples are composed of normal grains and deformation twins, the application of Hall-petch should be separated into two parts, in which a different effective grain size should be utilized. In the case of normal gains, it's easy to obtain this part GB strength since the average matrix size has been measured to be 500nm in the 5AlCrY and 1.2μm in the 5AlCr alloys. For the part of twins, if the twin density and size are both known, the calculation of deformed twins strengthening is fairly straight forward, as well. Therefore, the total GB strength could be shown with next relationship:

$$\sigma = \sigma_n \cdot V_n + \sigma_T \cdot V_T \quad (6.8)$$

in which σ is total GB strength; σ_n and V_n mean the normal grain GB strength and the volume fraction of the normal grains in matix; σ_T and V_T are corresponding GB strength and volume fraction coming from the deformed twins.

Fig. 6.19 shows the IPF and IQ maps of the room temperature tensile tested 5AlCrY and 5AlCr samples. Based on these images, the area fraction of deformation twins could be measured, which was found to be 20% in the 5AlCrY and 32% in the 5AlCr alloys, respectively. In respect of the calculation of twin size, since the motion direction of dislocation in the twins cannot be known, it's difficult to confirm the dislocation sliding is parallel to the long twin boundary or just perpendicular to it. Therefore, based on the observation of TEM, both the short and long distance between twin boundaries have been measured and the results are listed in **Table 6.1.** Besides, the corresponding Hall-petch strength with the two distances has been

calculated and introduced in the **Table 6.1**, which was marked with σ_S and σ_L, respectively.

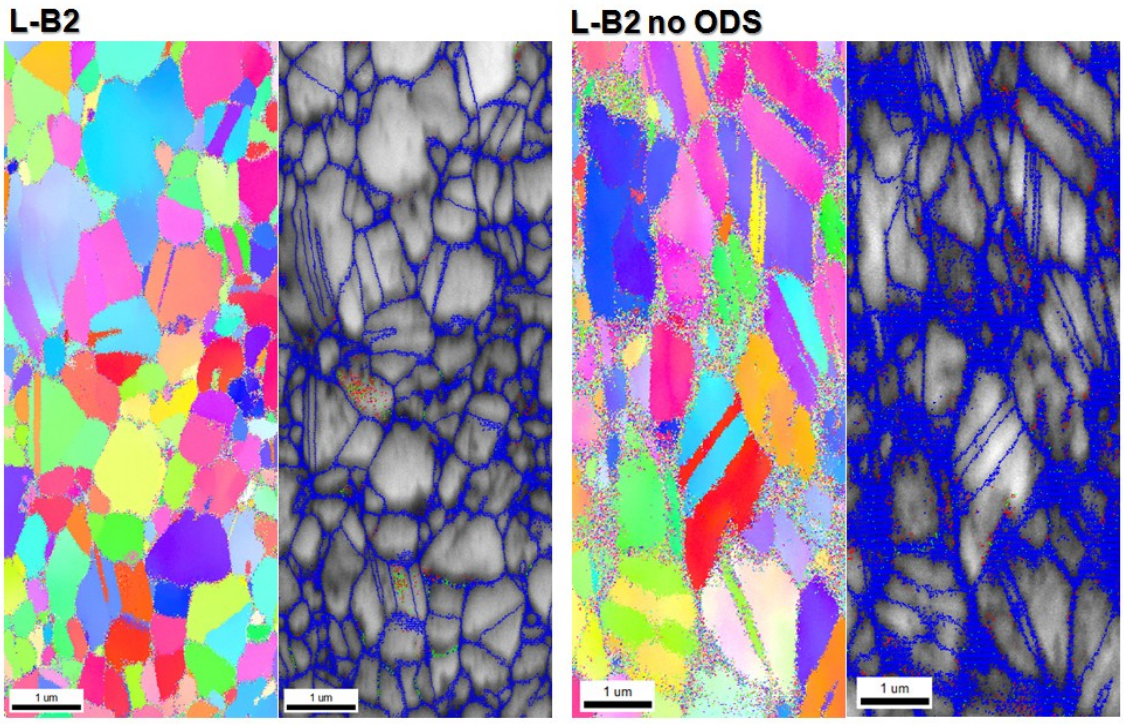

Fig. 6.19 IPF and corresponding IQ maps obtained from the 5AlCrY and the 5AlCr samples.

Table 6.1 Measured distance in deformed twin grains through TEM observation.

Alloys	Short distance/μm	σ_S/MPa	Long distance/μm	σ_L/MPa
5AlCrY	0.03	3845	1.20	822
5AlCr	0.08	2453	1.46	769

In the case of σ_T, we supposed it approximately equals to the average of the σ_S and σ_L, as follow;

$$\sigma_T = \sigma_S + \sigma_L \quad (6.9)$$

Table 6.2 exhibits all the calculated results in the two alloys.

Table 6.2 Calculated relative GB strength values for the deformed twins in the 5AlCrY and the 5AlCr samples.

Alloy	σ_n/MPa	V_n/%	$\sigma_n \cdot V_n$	σ_T/MPa	V_T/%	$\sigma_T \cdot V_T$	σ/MPa
5AlCrY	1134	80	907	2334	20	467	1374
5AlCr	822	68	559	1611	32	516	1075

Thus, the difference of the GB strength could be found to be 299 MPa, which is quite consistent with the value derived from the UTS difference (297 MPa) in the 5AlCrY and the 5AlCr sample. Besides, if we use the UTS strength to subtract the GB strength and relative ODS strength, the solid solution strength in the two samples could be approximately derived, which equals to 673 MPa in the 5AlCrY and 676 MPa in the 5AlCr alloys. Consequently, a summarization **Fig. 6.20** for the analysis of the UTS strength could be produced and listed as follows.

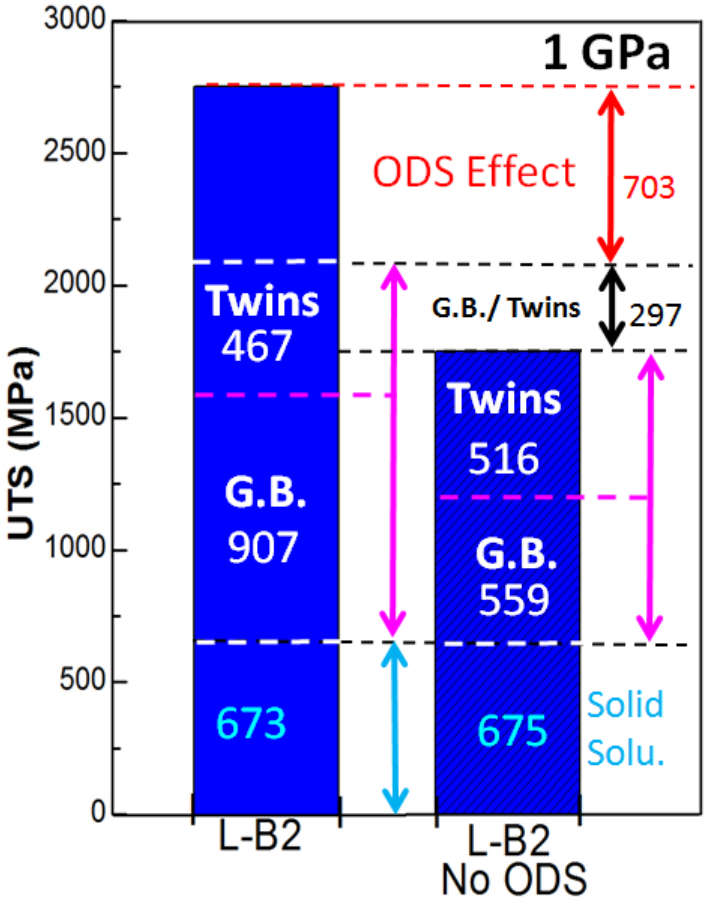

Fig. 6.20 Strength components for the UTS in the 5AlCrY and the 5AlCr samples.

Besides, it's known that the γ-cobalt (fcc) phase is metastable at room temperature and will experience a strain-induced γ-ε martensite transformation on deformation [121-123]. The Shockley partial dislocations at $\{111\}_{fcc}$ has been regarded as an origin for the formation of ε-martensite, and even resulting in fcc-twinning formation once the further deformation happened, as shown with the schematic plot in **Fig. 6.21** [124, 125].

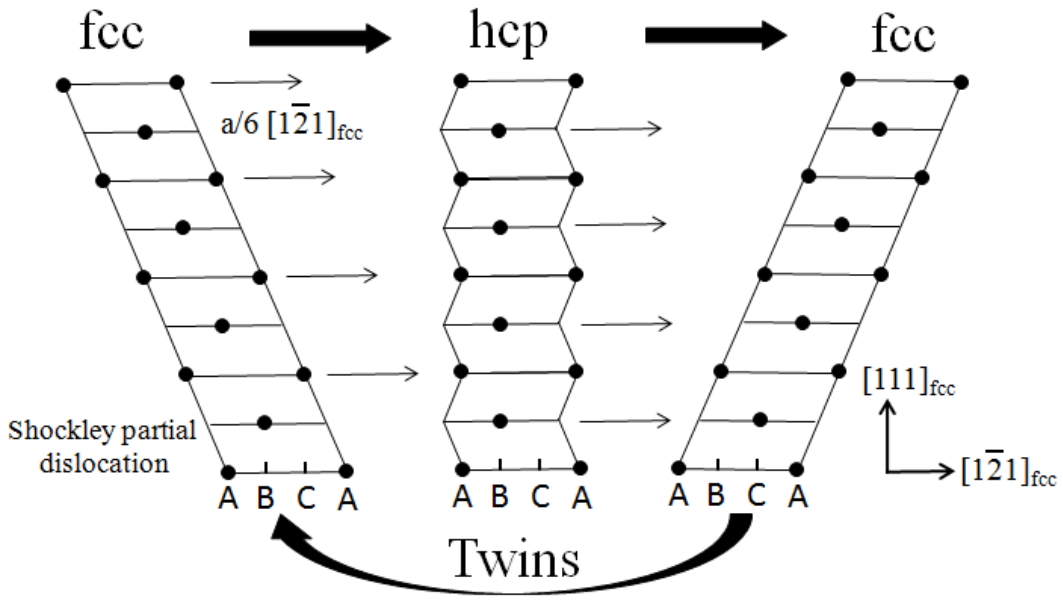

Fig. 6.21 Schematic illustration for the formation of hcp phase and fcc twins induced by Shockley partial dislocation in fcc matrix.

It's also clarified that the strain-induced γ-ε transformation occurs simultaneously with twinning deformation in ultrafine and nanocrystalline grains as the strain increased. And both the ε-martensite and twin boundaries act as strong barriers for blocking dislocation slipping [123]. In order to investigate the martinsite transformation during the tensile test at room temperature, the specimens of 5AlCrY and 5AlCr alloys after deformation were detected with X-ray diffraction analyses, as shown in **Fig. 6.22 (a)** and **(b)**, in which the results of before tensile test also have been inserted to outstanding the effect of deformation. However, no obvious growth of the hcp diffraction peak was found. It means that the ε-martensite phase is not available for interpreting the high strength of the Co-based alloys at room temperature, and the strain-induced direct twinning deformation is supposed to work.

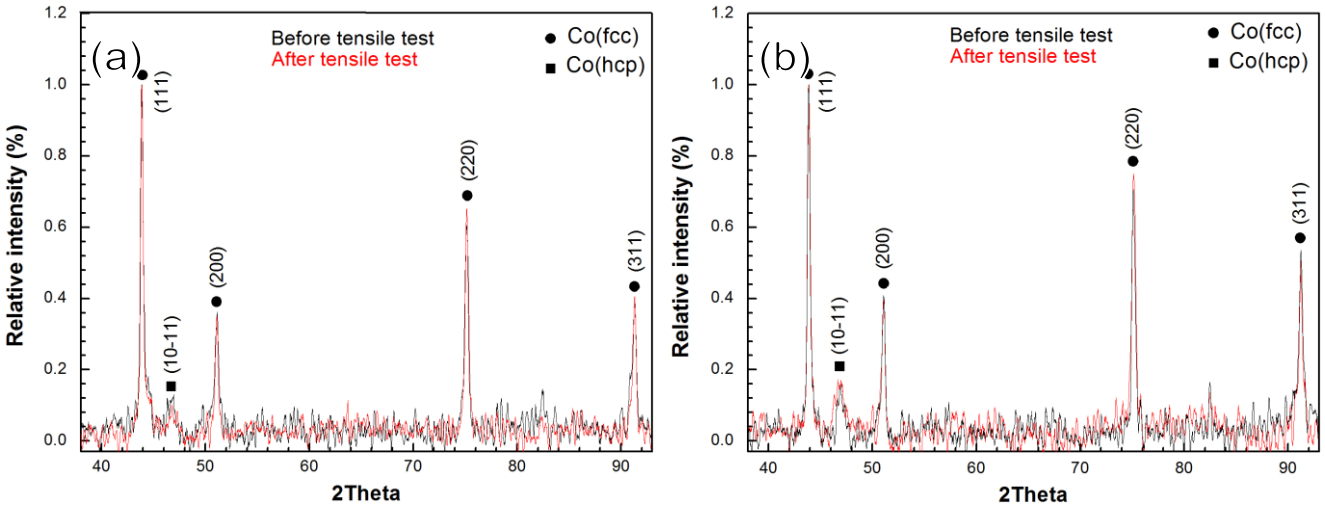

Fig. 6.22 Comparison between the XRD results of the samples before and after tensile test at 23 ^{o}C, (a) is 5AlCrY superalloy and (b) is 5AlCr alloy.

In addition, amounts of cracks at the normal surface of fractured 5AlCrY superalloy were observed, as shown in **Fig. 6.11**, which is being more noticeable with the increasing of temperature for tensile testing, such as at 1000 ^{o}C. According to the corresponding EBSD IQ and OIM-IPF maps, as shown in **Fig. 6.23 (a)** and **(b)**, the cracks are located along grain boundaries and grain boundary triple junctions, which is a clear evidence for the occurrence of grain boundary sliding. At elevated temperatures, deformation could be accelerated since the sliding and atomic diffusion through grain boundaries and results in the formation of cracks follow the grain boundaries. It's one of the main failure modes for the ODS superalloys who possess ultrafine grains [126]. Therefore, the drastic decrease on the UTS is attributed to the grain boundary sliding at elevated temperature, resulting in similar UTS at 1000 ^{o}C, as shown in the **Fig. 6.24**, even the different volume fraction of B2 and fcc phase in the 5AlCrY and 10AlCrY.

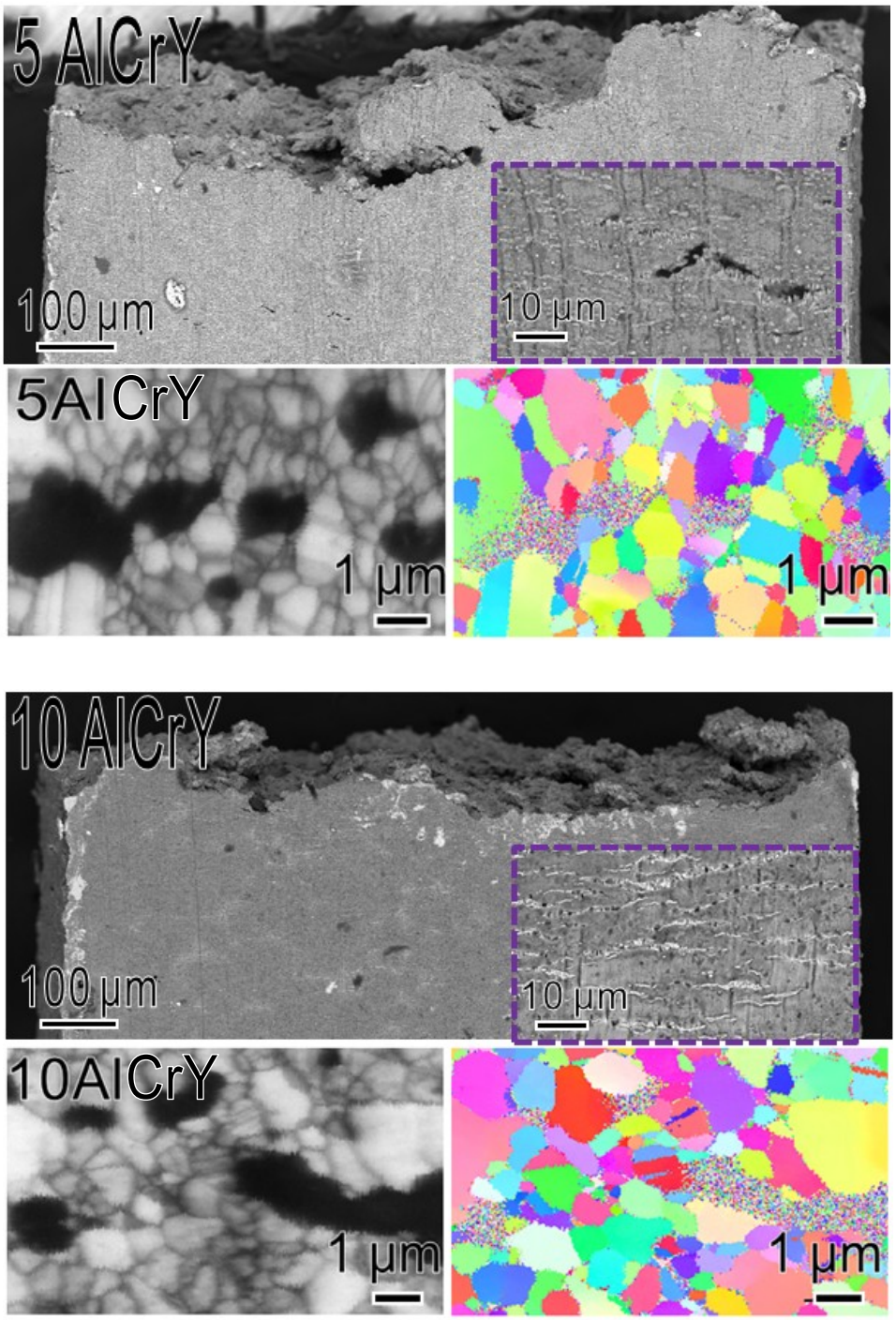

Fig. 6.23 SEM images and corresponding IQ/OIM-IPF maps on the fractured surfaces of the 5AlCrY and the 10AlCrY alloys at 1000^{o}C.

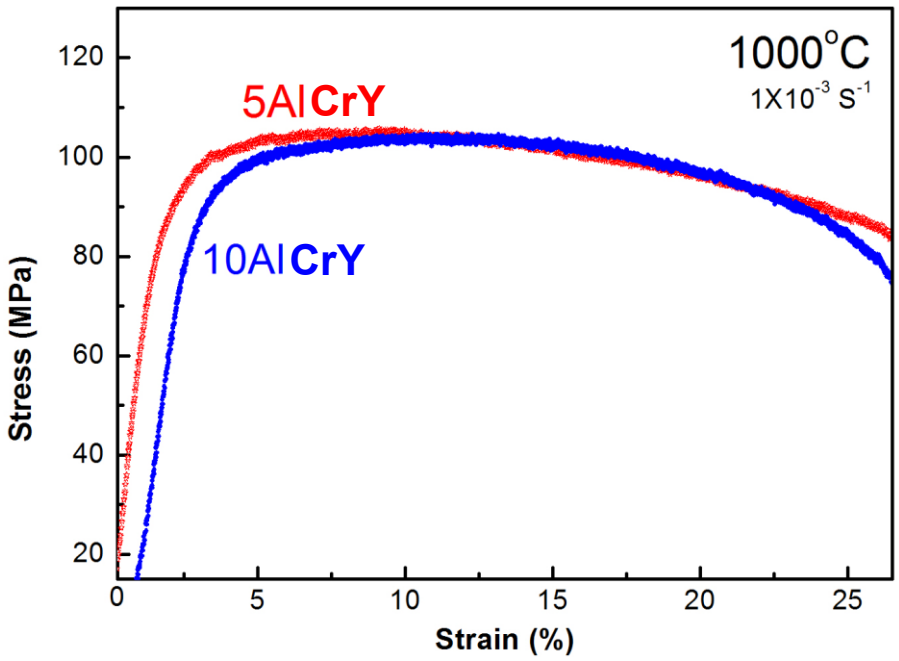

Fig. 6.24 Engineering stress-strain curves of the 5AlCrY and 10AlCrY alloys at the temperature of 1000 °C.

6.4 Summary

A comprehensive experimental investigation has been performed to characterize tensile properties of the novel Co-20Cr-(5, 10)Al-2.4Hf-1.5Y_2O_3 (wt. %) ODS superalloy. Specific conclusions are drawn as follows:

(1) The Co-based superalloys show a stable fcc phase at room temperature due to the ultrafine grain in both alloys, i.e. an average grain size of 500 nm in 5Al and 800 nm in10Al alloy, resulting from the ball-milling and pinning effect of Y-Hf oxide particles. With the increasing of Al addition, the ductility of Co-based superalloys was reduced significantly since a high brittleness of the B2 phase and results in a brittle fracture of the 10Al Co-based superalloys at low temperature.

(2) The 5Al Co-based superalloys exhibit extremely high tensile strength with the 2.65 GPa at room temperature, which is associated with the nano-twins deformation induced by strain. The distribution of fine Y-Hf oxides in the 5Al results in an improvement of strength with 631 MPa. The tensile strengths decreased significantly with the increase of temperature, and a similar UTS was

obtained in the 10Al and 5Al alloys at 1000 ºC, which is attributed to the grain boundaries deformation with an ultrafine grain in the both alloys.

Chapter 7 Conclusions and outlook

I have studied Co-based oxide dispersion strengthened (ODS) superalloys at the Ph.D course of Hokkaido University. In order to realize the excellent mechanical properties and oxidation resistance at 1,000 ºC, the innovative Co-20Cr-(5, 10)Al (wt. %)ODS superalloys containing 1.5 wt% Y_2O_3 were designed and fabricated by mechanical alloying (MA), spark plasma sintering (SPS), hot rolling and the final annealing at 1200 ºC. In the past three years, excellent results have been achieved concerning microstructure characterization, high temperature oxidation mechanism and mechanical strength characterization. The main achievements are described in the following.

(1) Microstructure characterization

The novel Co-based ODS superalloys were designed on the basis of Co-Cr-Al phase diagram computed by the thermodynamic software Pandat. The superalloys contain a Co solid solution phase with face-centered cubic (fcc) structure and a CoAl phase with body-centered cubic (B2) structure, which offers the guarantee for good ductility and favorable strength, respectively. The volume fraction of the two phases in the Co-based ODS superalloys could be flexibly controlled through changing the Al content from 5-10 wt. %. Fine Y-Hf oxides particles were found to be densely distributed in the both phases. Moreover, a unique core-shell structure of $Y_2Hf_7O_{17}$ in core and $Y_2Hf_2O_7$ at periphery was discovered, which provides significant references for the study of ODS superalloys.

(2) High temperature oxidation behavior.

High-temperature oxidation behavior of the Co-based ODS superalloys was investigated by the isothermal oxidation test at 900 ^oC and 1000 ^oC in air. With the increase of Al content from 5 wt. % to 10 wt. %, the oxidation resistance of the superalloys had been significantly improved by the formation of a single alumina scale instead of a duplex scale of outer $CoCr_2O_4/Cr_2O_3$ and inner Al_2O_3 in the 5Al. i.e., the 10Al specimens possess a better oxidation resistance than the 5Al specimens, which is far better than conventional Co-based alloys. A faster θ- to α-alumina transformation at higher temperature was found to be responsible for the smaller

weight gain at 1000 ºC than at 900 ºC for the 10 wt. % Al specimens. The effect of Cr on the oxidation resistance also was investigated, and it shows that the addition of Cr into Co-based ODS superalloys effectively improve high-temperature oxidation resistance by accelerating the formation of an exclusive alumina scale instead of the multilayered scale with an external $CoO/CoAl_2O_4$ and an inner Al_2O_3. Besides, with Y_2O_3 addition, the Co-based ODS superalloys was proved to possess far better oxide-scale adherence than that in free Y_2O_3 alloys.

(3) Mechanical Properties.

The tensile strengths of the Co-20Cr-(5, 10)Al ODS superalloys were evaluated. Both 5Al and 10Al alloys possess high tensile strength at 23 ^{o}C. 10Al shows less strength at low temperature since a brittle fracture caused by high B2 volume fraction. One point should be noted is that 5Al possesses almost 2.85 GPa at room temperature, which is far better than the strength in Fe- and Ni-based alloys, it would be comparable with the strongest steels in the world. The mechanism of this excellent strength was clarified to be attributed to the strain-induced nano-twins deformation during the tensile test. The distribution of fine Y-Hf oxides results in an improvement of strength with 703 MPa in the 5Al and 670MPa in the 10Al superalloys, respectively. However, along with the increasing of temperature, a drastic reduction in strength was observed, which is attributed to grain boundary deformation at elevated temperatures due to the ultrafine grains of 500 nm in the 5Al and 800 nm in the 10Al Co-based superalloys.

(4) Optimized composition and outlook

According to the previous results that the tensile strength of 5Al is higher than 10Al, less Al should be considered to add into the composition of the Co-based superalloys, the reason was confirmed to be the brittle fracture in 10Al with high B2 volume fraction. However, the 10Al superalloy possesses a superior oxidation resistance with the formation of a single alumina scale than the 5Al superalloys with a duplex scale of outer $CoCr_2O_4/Cr_2O_3$ and inner Al_2O_3. Hence, in the next step, the composition optimization based on altering the Al content should be conducted, to find out the least Al content to form the single Al_2O_3 scale through isothermal

oxidation testing at 1000^{o}C. The Al addition of 6 or 7 wt.% was considered to be applicable in this system.

Besides, previous results in our lab have demonstrated that directionally recrystallized grains can be formed in Ni-base ODS superalloys by zone annealing at appropriate conditions. Besides, it was proved that the primary orientation of grains controls the mobility of grain boundary migration and [100] crystalline direction is desirable for columnar grain formation. Hence, zone annealing is considered to make coarse grains in the Co-based ODS superalloys. Due to zone annealing is performed in a temperature gradient, the effect of parameters (annealing temperature, temperature gradient, holding time and travel speed of specimens) on grain morphology will be studied.

Through controlling the aluminum content in the composition, a minimum volume fraction of B2 phase with the ability to form a single Al_2O_3 scale would be retained in the Co-base ODS superalloys. Besides, directionally recrystallized coarse grains with a uniform distribution of ultrafine $Y_2Hf_2O_7$ oxide particles would be implemented and as the desirable microstructure of the Co-based ODS superalloys, which ensures a combination of excellent high temperature strength and microstructure stability at high temperature above 1000^{o}C. The innovative Co-based ODS superalloys will be expected to be used in making high temperature parts of industrial gas turbine, and the thermal efficiency is able to be remarkably improved for the industrial gas turbine. This development greatly contributes to the realization of the next generation of ultrahigh efficient industrial gas-turbines.

References

[1] Bilbrey, Joseph H, Cobalt: a materials survey, U.S. Bureau of Mines, 1962, pp. 3-5.

[2] D. Coutsouradis, A. Davin, M. Lamberigts, Cobalt-based superalloys for applications in gas turbines，Mater. Scin. Eng. 88 (1987) 11-19.

[3] J. Szala, A. Szczotok, J. Richter, J. Cwajna, A. Maciejny, Selection of methods for etching carbides in MAR-M509 cobalt-base superalloy and acquisition of their images, Mater. Charact. 56 (2006) 325-335.

[4] S.H. Zangeneh, H. Farhangi, Influence of service-induced microstructural changes on the failure of a cobalt-based superalloy first stage nozzle, Mater. Des. 31 (2010) 3504-3511.

[5] J. Sato, T. Omori, K. Oikawa, I. Ohnuma, R. Kainuma, K. Ishida, Cobalt-base high-temperature alloys, Science 312 (2006) 90-91.

[6] K. Shinagawa, T. Omori, J. Sato, K. Oikawa, I. Ohnuma, Phase equilibria and microstructure on γ' phase in Co-Ni-Al-W system, Mater. Trans. 49 (2008) 1474-1479.

[7] L. Klein, A. Bauer, S. Neumeier, M. Goken, S.Virtanen, High temperature oxidation of γ/γ'-strengthened Co-base superalloys, Corros. Sci. 53 (2011) 2027–2034.

[8] N. Vermaak, A. Mottura, T.M. Pollock, Cyclic oxidation of high temperature coatings on new γ'-strengthened Co-based alloys, Corros. Sci. 75 (2013) 300–308.

[9] L. Klein, Y. Shen, M. Killian, S. Virtanen, Effect of B and Cr on the high temperature oxidation behavior of novel γ/γ'-strengthened Co-base superalloys, Corros. Sci. 53 (2011) 2713–2720.

[10] L. Klein, M. Killian, S. Virtanen, The effect of nickel and silicon addition on some oxidation properties of novel Co-based high temperature alloys, Corros. Sci. 69 (2012) 43–49.

[11] L. Zhang, X.H. Qu, X.B. He, R.U. Din, H.S. Liu, M.L. Qin, H.M. Zhu,

Microstructural characterization of Co-based ODS alloys, J. Mater. Eng. Perform. 21 (2012) 2487–2494.

[12] S. Ukai, S. Ohtsuka, Nano-mesoscopic structure control in 9Cr–ODS ferritic steels, Energy Mater. 2(1) (2007) 26–35.

[13] S. Ukai, T. Kaito, S. Ohtsuka, T. Narita, M. Fujiwara, T. Kobayashi, Production and properties of nano-scale oxide dispersion strengthened (ODS) 9Cr martensitic steel claddings, ISIJ int. 43 (2003) 2038–2045.

[14] S. Ukai, M. Fujiwara, Perspective of ODS alloys application in nuclear environments, J. Nucl. Mater. 307-311 (2002) 749–757.

[15] M. Yamamoto, S. Ukai, S. Hayashi, T. Kaito, S. Ohtsuka, Formation of residual ferrite in 9Cr-ODS ferritic steels, Mater. Sci. Eng. A 527 (2010) 4418–4423.

[16] Q. Tang, T. Hoshino, S. Ukai, B. Leng, S. Hayashi, Y. Wang, Refinement of oxide particles by addition of Hf in Ni-0.5 mass%Al-1 mass%Y2O3 Alloys, Mater. Trans. 51 (11) (2010) 2019–2024.

[17] T. Kaito, T. Narita, S. Ukai, Y. Matsuda, High temperature oxidation behavior of ODS steels, J. Nucl. Mater. 329-333 (2004) 1388–1392.

[18] W.J. Quadakkers, H. Holzbrecher, K.G. Briefs, H. Beske, Difference in growth mechanisms of oxide scales formed on ODS and conventional wrought alloys. Oxid. Met. 32 (1989) 67–88.

[19] W.J. Quadakkers, Oxidation of ODS alloys, J PHYS IV. 3 (1993) 177–186.

[20] G.N. Irving, J. Stringer, D.P. Whittle, The oxidation behavior of Co-Cr-Al alloys at 1000 ^{o}C, Corrosion-Nace 33 (1977) 56–60.

[21] G.N. Irving, J. Stringer, D.P. Whittle, The high-temperature oxidation resistance of Co-Al alloys, Oxid. Met. 9 (1975) 427–440.

[22] P.S. Liu, K.M. Liang, High-temperature oxidation behavior of the Co-based superalloy DZ40M in air, Oxid. Met. 53 (2000) 351–360.

[23] L. Zhang, S. Ukai, T. Hoshino, S. Hayashi, X. Qu, Y_2O_3 evolution and dispersion refinement in Co-base ODS alloys, Acta Mater. 57 (2009) 3671–3682.

[24] L. Zhang, X.B. He, X.H. Qu, Y. Liu, M.L. Qin, H.M. Zhu, Characteristics of complex oxides in Co based ODS alloys, Powder Metall. 56 (2013) 24–31.

[25] K. Takezawa, S. Ukai, S. Hayashi, Microstructure control of Co-base ODS alloys, Adv. Mater. Res. 239–242 (2011) 864–867.

[26] T. Sasaki, K. Takazawa, S. Ukai, N. Oono, S. Hayashi, Effect of heat treatment on the hardness and microstructure in Co-3Al-1.5Y_2O_3-1.2Hf ODS alloy, Mater. Sci. Eng. A 601 (2014) 139–144.

[27] A. Czyrska-Filemonowicz, B. Dubiel, Mechanically alloyed, ferritic oxide dispersion strengthened alloys: structure and properties, J. Mater. Process. Technol. 64 (1997) 53–64.

[28] G. R. Wallwork, A. Z. Hed, Some limiting factors in the use of alloys at high temperatures, Oxid. of Metals 3 (1971) 171-184.

[29] Sims C T, Stoloff N S and Hagel W C, Superalloys II - High temperature materials for aerospace and industrial power, John Wiley & Sons, 1987.

[30] F. R. Morral, Cobalt-Base Alloys In Aerospace, The Space Congress Proceedings, April 1, 1970, 53-63.

[31] Jiang W H, Yao X D, Guan H R and Hu Z a, Secondary M_6C precipitation in a cobalt-base superalloy, Journal of Materials Science Letters, 18 1999, 303-305.

[32] Lane J R and Grant N J, Carbide Reactions in High Temperature Alloys,Transaction of ASM, 44 1952, 113-120.

[33] Jiang W H, Yao X D, Guan H R, Hu Z Q, Secondary carbide precipitation in a directionally solidified cobalt-base superalloy, Metallurgical and Materials Transactions A, 30A 1999, 513-520.

[34] Jiang W H, Yao X D, Guan H Rand Hu Z Q, Carbide behaviour during high temperature low cycle fatigue in a cobalt-base superalloy, Journal of Materials Science and Technology, 15 1999, 515-518.

[35] B. Geddes, H. Leon, X. Huang, Superalloys: Alloying and performance, ASM International, Materials Park, Ohio, USA (2010).

[36] J.M. Blaise, P. Viatour, J.M. Drapier, Cobalt 49 (1970), 192.

[37] J.W. Martin, Micromechanisms in particle-hardened alloys, Cambridge University Press, London, 1980.

[38] S. Ukai, S. Ohtsuka, T. Kaito, H. Sakasegawa, N. Chikata, S. Hayashi, S. Ohnuki,

High-temperature strength characterization of advanced 9Cr-ODS ferritic steels, Mater. Sci. Eng. A 510-511 (2009) 115–120.

[39] M.J. Alinger: Ph.D dissertation, University of California Santa Barbara, 2004.

[40] Q.X. Tang: Ph.D dissertation, Hokkaido University, 2012.

[41] D.J. Srolovitz, R.A. Petkovic, M.J. Luton. Acta Metall 31 1983 2151.

[42] R.O. Scattergood, D.J. Bacon, Phil. Mag. A 31(1975) 179-198.

[43] A.Y. Badmos: Ph.D dissertation, University of Cambridge, 1997.

[44] D.J. Yong, High temperature oxidation and corrosion of metals, Elsevier Corrosion Series, 1st edition, Amsterdam, The Netherlands (2008).

[45] H.J.T. Ellingham, J. Soc. Chem. Ind. 63 (1944) 125.

[46] Vadym Kochubey: Ph.D dissertation, Kiew, Ukraine (2005).

[47] P.K. Kofstad, High temperature corrosion, Elsevier (1988).

[48] P.K. Kofstad, A.Z. Hed, High-temperature oxidation of Co-10w/o Cr alloys II. Oxidation kinetics, J. Electrochem. Soc. 116 (1969) 229–234.

[49] P.K. Kofstad, A.Z. Hed, Oxidation of Co-25 w/o Cr at high temperatures, J. Electrochem. Soc. 116 (1969) 1542–1550.

[50] David L Oates: Ph.D dissertation, Loughborough University (2007).

[51] W.J. Quadakkers, Growth mechanisms of oxide scales on ODS alloys in the temperature range 1000-1100 ºC, Werkstoffe und Korrosion 41 (1990) 659–668.

[52] Z.H. Zhang, Z.Fe. Liu, J.F. Lu, X.B. Shen, F.C. Wang, Y.D. Wang, The sintering mechanism in spark plasma sintering – Proof of the occurrence of spark discharge, Scripta Mater. 81 (2014) 56-59.

[53] P. Susila, D. Sturm, M. Heilmaier, B. S. Murty, V. S. Sarma, Microstructural studies on nanocrystalline oxide dispersion strengthened austenitic (Fe–18Cr–8Ni–2W–0.25Y_2O_3) alloy synthesized by high energy ball milling and vacuum hot pressing, J. Mater. Sci.45 (2010) 4858-4865.

[54] V. C. Nardone, J.K. Tien, Pinning of dislocations on the departure side of strengthening dispersoids, Scripta Metal. 17 (1983) 467-470.

[55] S. Ukai, T. Okuda, M. Fujiwara, T. Kobayashi, S. Mizuta, H. Nakashima, Characterization of high temperature creep properties in recrystallized 12Cr-ODS

ferritic steel claddings, J. Nucl. Sci. Technol. 39 (2002) 872-879.

[56] S.N. Hosseini, T. Mousavi, F. Karimzadeh, M.H. Enayati, Thermodynamic aspects of nanostructured CoAl intermetallic compound during mechanical alloying, J. Mater. Sci. Technol. 27 (7) (2011) 601-606.

[57] Y. Takano, M. Yoshinaka, K. Hirota, O. Yamaguchi, Mechanical properties of CoAl materials with the combined additions of ZrO_2(3Y) and Al_2O_3, J. Am. Ceram. Soc. 84 (2001) 2445-2447.

[58] K. Ishikawa, M. Ise, I. Ohnuma, R. Kainuma, K. Ishida, Phase equilibria and stability of the BCC aluminide in the Co-Cr-Al system, Phys. Chem. 102 (1998) 1206-1210.

[59] R. Nakamura, Y. Iijima, Self-diffusion of cobalt in B2 type intermetallic compound CoAl, Intermetallics, 13 (2005) 163-167.

[60] M. Wang, Z.J. Zhou, H.Y. Sun, et al. Microstructural observation and tensile properties of ODS-304 austenitic steel, Mater. Sci. Eng. A 559 (2013) 287-292.

[61] Ch.Ch. Eiselt, M. Klimenkov, R. Lindau, A. Möslang, H.R.Z. Sandim, A.F. Padilha, D. Raabe, High-resolution transmission electron microscopy and electron backscatter diffraction in nanoscaled ferritic and ferritic–martensitic oxide dispersion strengthened–steels, J. Nucl. Mater., 385 (2009), pp. 231–235

[62] P. Miao, G.R. Odette, T. Yamamoto, M. Alinger, D. Hoelzer, D. Gragg, Effects of consolidation temperature, strength and microstructure on fracture toughness of nanostructured ferritic alloys, J. Nucl. Mater., 367–370 (2007), pp. 208–212

[63] P. He, M. Klimenkov, R. Lindau, A. Möslang, Characterization of precipitates in nano structured 14% Cr ODS alloys for fusion application, J. Nucl. Mater., 428 (2012), pp. 131–138

[64] X. Boulnat, D. Fabregue, M. Perez, M. Mathon, Y. Decarlan, High-Temperature Tensile Properties of Nano-Oxide Dispersion Strengthened Ferritic Steels Produced by Mechanical Alloying and Spark Plasma Sintering, Metall. Mater. Trans. 44A (2013) 2461–2465.

[65] X. Boulnat, M. Perez, D. Fabregue, T. Douillard, M. Mathon, Y. Decarlan, Microstructure Evolution in Nano-reinforced Ferritic Steel Processed By

Mechanical Alloying and Spark Plasma Sintering, Metall. Mater. Trans. 45A (2014) 1485–1497.

[66] G.H. Xu, G.F. Wang, K.F. Zhang, Effect of rare earth Y on oxidation behavior of NiAl-Al_2O_3, Trans. Nonferrous Met. Soc. China 21(2011) 362–368.

[67] K.M.N. Prasanna, A.S. Khanna, Ramesh Chandra, W.J. Quadakkers, Effect of θ-alumina formation on the growth kinetics of alumina-forming superalloys. Oxid. Met. 46 (1996) 465-480.

[68] H. Yu, S. Ukai, N. Oono, T. Sasaki, Microstructure characterization of Co-20Cr-(5, 10)Al oxide dispersion strengthened superalloys, Mater. Charact. 112(2016)188–196.

[69] W. Cao, S.-L. Chen, F. Zhang, K. Wu, Y. Yang, Y.A. Chang, R. Schmid-Fetzer, W.A. Oates, PANDAT software with PanEngine, PanOptimizer and PanPrecipitation for multi-component phase diagram calculation and materials property simulation, Calphad 33 (2009) 328–342.

[70] P.K. Kofstad, A.Z. Hed, High-temperature oxidation of Co-10w/o Cr alloys I. Microstructure of oxide scales, J. Electrochem. Soc. 116 (1969) 224–229.

[71] V.B. Trindade, U. Krupp, B.Z. Hanjari, S. Yang, H-J. C, Effect of alloy grain size on the high-temperature oxidation behavior of the austenitic steel TP 347, Materials Research, 8 (2005) 371–375.

[72] Y. Kitajima, Study on phase transformation of Al_2O_3 scale formed at high-temperatures, PhD thesis, Hokkaido University, 2010.

[73] H. Hindam, D.P. Whittle, Microstructure, adhesion and growth kinetics of protective scales on metals and alloys, Oxid. Met. 245 (1982) 245-284.

[74] B.A. Pint, I.G. Wright, Long-term high temperature oxidation behavior of ODS ferritics, J. Nucl. Mater. 307–311 (2002) 763–768.

[75] P. Lours, J. Alexis, G. Bernhart, Oxidation resistance of ODS alloy PM2000 from 880 ^{o}C to 1400 ^{o}C, J. Mater. Scilett. 17 (1998) 1089–1093.

[76] B.A. Pint, M. Treska, L.W. Hobbs, The effect of various oxide dispersions on the phase composition and morphology of Al_2O_3 scale growth on–βNiAl, Oxid. Met. 47 (1997) 1–19.

[77] B.A. Pint, J.R. Martin, L.W. Hobbs, The oxidation mechanism of θ-Al_2O_3 scales, Solid State Ionics 78 (1995) 99–107.

[78] L. Marechal, B. Lesage, A.M. Huntz, R. Molins, Oxidation behavior of ODS Fe–Cr–Al alloys: aluminum depletion and lifetime, Oxid. Met. 60 (2003) 1–28.

[79] E.G. Moya, F. Moya, B. Lesage, M.K. Loudjani, C. Grattepain, Yttrium diffusion in α-alumina single crystal, J. Eur. Ceram. Soc. 18 (1998) 591-594.

[80] C. Wagner, Diffusion and high temperature oxidation of metals, Atom Movements, Ohio (1951) 153.

[81] P. Kofstad, High-temperature oxidation of metals, John Wiley & Sons, Inc., New York 1966.

[82] S. Mrowec, T. Walec and T. Werber, Oxidation of cobalt at high temperatures, Corros. Sci. 6 (1966) 287–297.

[83] Y. Niu, S. Wang, F. Gao, Z.G. Zhang, F. Gesmundo, The nature of the third-element effect in the oxidation of Fe–xCr–3 at.% Al alloys in 1 atm O_2 at 1000 ^oC, Corros. Sci. 50 (2008) 345–356.

[84] Y. Niu, X.J. Zhang, Y. Wu, F. Gesmundo, The third-element effect in the oxidation of Ni–xCr–7Al (x = 0, 5, 10, 15 at.%) alloys in 1 atm O_2 at 900–1000 ^oC, Corros. Sci. 48 (2006) 4020–4036.

[85] C. Wagner, Passivity and inhibition during the oxidation of metals at elevated temperatures, Corros. Sci. 5 (1965) 751–764.

[86] C. Wagner, Z. Elektrochem. 63 (1959) 772.

[87] K. Shobu, CaTCalc: New thermodynamic equilibrium calculation software, Calphad 33 (2009) 279–287.

[88] K. Shobu, T. Tabaru, Development of new equilibrium calculation software: CaTCalc, Mater. Trans. 46 (6) (2005) 1175–1179.

[89] H.J. KLAM, Temperature and oxidation resistance of the ODS materials MA 956 and PM 2000, J PHYS IV. 3 (1993) 731–734.

[90] T.N. Phys-Jones, H. J. Grabke, H. Kudielka, The effects of various amounts of alloyed cerium and cerium oxide on the high temperature oxidation of Fe-10Cr and Fe-20Cr alloys, Corros. Sci. 27 (1987) 49–73.

[91] V.C. Nardone, J.K. Tien, Pinning of dislocations on the departure side of strengthening dispersoids, Scr. Metall. 17 (1983) 467–470.

[92] D. Naumenko, B. Gleeson, E. Wessel, L. Singheiser, W.J. Quadakkers, Correlation between the microstructure, growth mechanism, and growth kinetics of alumina scales on a FeCrAlY alloy, Metall. Mater. Trans. A, 38 (2007) 2974–2983.

[93] D.J. Young, D. Naumenko, L. Niewolak, E. Wessel, L. Singheiser, W.J. Quadakkers, Oxidation kinetics of Y-doped FeCrAl-alloys in low and high pO_2 gases, Materials and Corrosion 61 (2010) 838–844.

[94] M. Turker, T. A. Hughes, Oxidation behavior of three commercial ODS alloys at 1200 ºC, Oxid. Met. 44 (1995) 505–525.

[95] J.K. Tien, F.S. Pettit, Mechanism of oxide adherence on Fe-25Cr-4AI (Y or Sc) Alloys, Metall. Trans. 3 (1972) 1587–1599.

[95] K. Arun, M. Nasrallab, D.L. Douglass, The effect of yttrium and thorium on the oxidation behavior of Ni-Cr-Al alloys, NASA CR-2422 (1974).

[96] I. Marek, D. Vojtech, A. Michalcova, et al, The structure and mechanical properties of high-strength bulk untrafine-grained cobalt prepared using high-energy ball milling in comination with spark plasm sintering, materials (2016) 9, 391.

[97] K. Ando, T. Omori, J. Sato, et al., Effect of alloying elements on fcc/hcp martensitic transformation and shape memory properties in Co-Al alloys, Materials Transactions, 47 (2006) 2381-2386.

[98] P. Huang, H.F. Lopez, Athermal ε-martensite in a Co-Cr-Mo alloy: grain size effects, Materials Letters 39 (1999) 249–253.

[99] P. Huang, H.F. Lopez, strain induced ε-martensite in a Co-Cr-Mo alloy: grain size effects, Materials Letters 39 (1999) 244–248.

[100] Zhao, X.; Liang, Y.; Hu, Z.; Liu, B. Thermodynamic interpretation of the martensitic transformation in ultrafine-Fe(N) particles. Jpn. J. Appl. Phys. 1996, 35, 4468–4473.

[101] Sarkar, S.; Bansal, C.; Chatterjee, A. Gibbs-Thomson effect in nanocrystalline

Fe-Ge. Phys. Rev. B 2000, 62, 3218–3222.

[102] Zhao, X.Q.; Veintemillas-Verdaguer, S.; Bomati-Miguel, O.; Morales, M.P.; Xu, H.B. Thermal history dependence of the crystal structure of Co fine particles. Phys. Rev. B 2005, 71.

[103] Ray, A.E.; Smith, S.R.; Scofield, J.D. Study of the phase transformation of cobalt. J. Phase Equilib. 1991, 12, 644–647.

[104] Ma, G.; Zhao, X.; Veintemillas-Verdaguer, S. Size dependent allotropic transition of Co fine particles. J. Nanosci. Nanotechnol. 2009, 9, 4472–4477.

[105] Nazari, A.; Zakeri, M. Modeling the mean grain size of synthesized nanopowders produced by mechanical alloying. Ceram. Int. 2013, 39, 1587–1596.

[106] Abdellahi, M.; Bahmanpour, M. Rapid synthesis of nanopowders in high energy ball milling; Optimization of milling parameters. Ceram. Int. 2015, 41, 1631–1639.

[107] S. Ukai, S. Ohtsuka, Nano-mesoscopic structure control in 9Cr–ODS ferritic steels, Energy Mater. 2(1) (2007) 26–35.

[108] Y. Li, Y.H. Zhao, W. Liu, C. Xu, Z. Horita, etc, Influence of grain size on the density of deformation twins in Cu-30%Zn alloy, Mater. Sci. Eng. A 527 (2010) 3942–3948.

[109] J.A. Venables, Philos. Mag. 6 (1961) 379-396.

[110] Y.S. Li, N.R. Tao, K. Lu, Acta Mater. 56 (2008) 230-241

[111] M.W. Chen, E. Ma, K.J. Hemker, H.W. Sheng, Y.M. W, X.M. Cheng, Deformation Twinning in nanocrystalline aluminum, Science 300 (2003) 1275-1277.

[112] X. Wu, N. Tao, Y. Hong, J. Lu, K. Lu, $\gamma \rightarrow \varepsilon$ martensite transformation and twinning deformation in fcc cobalt during surface mechanical attrition treatment, Scri. Mater, 52 (2005) 547-551.

[113] Sort J, Nogues J, Surinach S, Baro MD. Phil. Mag. 83 (2003)439.

[114] L. Remy, A. Pineau, Twinning and strain-induced F.C.C.—H.C.P. transformation on the mechanical properties of Co-Ni-Cr-Mo alloys, Mater. Sci.

Eng. 26 (1976) 123–132.

[115] Gray III GT. J Phys IV France 1997;7:423.

[116] A.A. Salem, S.R. Kalidindi, R.D. Doherty, Scripta Mater. 46 (6) (2002) 419.

[117] E.O. Hall, Proc. Phys. Soc. London 64B (1951) 747.

[118] N.J. Petch, J. Iron steel Inst. 174 (1953) 25.

[119] R.W Armstrong, I. Codd, R.N. Douthwaite, N.J. Petch, Phil. Mag. 7 (1962) 45.

[120] R. DiDomizio, M.F. Gigliotti, J.S. Marte, PR. Subramanian, V. Valitov, Evaluation of a Ni-20Cr alloy processed by multi-axis forging, Materials Science Forum, 503-504 (2006) 793-798.

[121] Bibby MJ, Gordon Parr J. Cobalt 1963;20:111.

[122] Bibring H, Sebilleau F, Buckle CJ. Inst Metals 1958–1959;87:71.

[123] X. Wu, N. Tao, Y. Hong, G. Liu, B. Xu, J. Lu, K. Lu, Strain-induced grain refinement of cobalt during surface mechanical attrition treatment, Acta Mater. 53 (2005) 681-691.

[124] S. Mahajan, Critique of mechanisms of formation of deformation, annealing and growth twins: Face-centered cubic metals and alloys, Scripta Mater. 68 (2013) 95–99

[125] マルテンサイト変態の型とその結晶構造, 57.

[126] Y. Sugino, S. Ukai, B. Leng, Q.X. Tang, S. Hayashi, T. Kaito, S. Ohtsuka, Grain boundary deformation at high temperature tensile tests in ODS ferritic steel, ISIJ International, Vol. 51 (2011), No. 6, pp. 982–986.

Acknowledgements

First of all, I would like to sincerely thank my supervisor, Prof. Dr. S. Ukai for giving me the opportunity to work on this interesting topic and for his professional guidance and strong support throughout my PhD career. I greatly appreciate all the help he gave and his trust in me and my work.

I would like to extend my appreciation to Prof. Dr. S. Miura and Associate Prof. Dr. N. Sakaguchi, who reviewed my dissertation and provided me many constructive suggestions.

I wish to thank Associate Prof. Dr. S. Hayashi, for his valuable discussion and insightful comments on the study of high-temperature oxidation, I am also very grateful for his enthusiasm and encouragement.

I would like to thank Assistant Prof. Dr. N. Oono for her guidance in the operation of FIB and TEM, and also appreciate her useful suggestions in my research.

I am also grateful to the entire members of my laboratory for providing the friendly and aggressive studying environment. Dr. Xiaochao Wu, Dr. Yoshito Sugino, Dr. Shi Shi, Mr. Syoutaro Yamagishi, Dr. Bikas C. Maji, Dr. S.M. Seyyed Aghamiri, Mr. Tetsuya Yamashiro and many other previous/current members, thanks for all your advice and help.

Special thanks to the "Joint-use Facilities: Laboratory of Nano-Micro Material Analysis" of Hokkaido University for the supply and operation of analysis equipments, particularly, Mr. Nobuyuki Miyazaki for EPMA, Endo Takashi for FIB and Dr. Yongming Wang for TEM.

I also acknowledge the China Scholarship Council (CSC) for the provision of a scholarship during my PhD period.

I am extremely thankful to my family for their support, especially my girlfriend, for her warm caring and accompanying in Japan.

Finally, I would also like to thank my friends and everybody who helped me during my PhD study in Hokkaido University.